Development and Validation of Improved Electromagnetic Transient Simulation Models for Solar Photovoltaic Energy Systems

by

Githmi Chanika Ranasinghe

A thesis submitted to the

Faculty of Graduate and Postdoctoral Studies

of the University of Manitoba

in partial fulfilment of the requirements for the degree of

MASTER OF SCIENCE

Department of Electrical and Computer Engineering

University of Manitoba

Winnipeg.

Abstract

Solar photovoltaic (PV) energy systems are central to the transition toward sustainable power generation. However, integrating them into modern power grids requires careful system studies to mitigate potential undesirable impacts. These studies focus on control strategies to maintain grid stability during disturbances and typically conducted using electromagnetic transient (EMT) simulations. Thus, properly parameterized models of key components such as PV modules are essential to accurately evaluate system behavior. The inverter control strategies need to be improved to ensure stability during disturbances.

To address some of these issues, this thesis develops a robust method for extracting parameters of the Single Diode Model (SDM) of monofacial PV modules from data sheet information. The models of bifacial PV modules, whose output depends on both front and rear irradiance, are not well established. Rear-side irradiance and partial shading effects are often inadequately characterized in manufacturer datasheets, leading to performance prediction errors. In this study, the SDM is extended to bifacial modules by incorporating bifacial gain and partial shading effects, and a method to extract model parameters is proposed. Validation of this model is carried out using manufacturer datasheets and experimental data from published sources.

Fast synchronization of solar plants during grid disturbances is critical for maintaining system stability. Frequency measurement accuracy becomes especially important when PV plants participate in power-frequency control, as errors during transients can lead to maloperation. To address these challenges, two key enhancements are proposed to the Double Second Order Generalized Integrator Phase-Locked Loop (DSOGI-PLL). First, a

transient elimination mechanism is introduced to detect grid disturbances and temporarily hold the frequency output, thereby preventing erroneous readings. Then, an adaptive bandwidth control strategy is proposed to dynamically increases the bandwidth of the DSOGI-PLL during transients to improved the response time. The proposed DSOGI-PLL is validated in PSCAD/EMTDC using synthetic waveforms, a solar plant connected to a voltage source behind an impedance, and a modified IEEE 9-bus system with solar integration. Furthermore, a power reserve control of solar plant is evaluated to demonstrate its effectiveness in supporting primary frequency response during grid disturbances.

Acknowledgment

I would like to express my heartfelt gratitude to Prof. Athula Rajapakse for his invaluable supervision and guidance throughout this research. His deep insights, shared experiences, continuous support, and motivation were instrumental in helping me achieve the objectives of this study.

I am also sincerely thankful to the Faculty of Graduate Studies for their support through scholarship programs, which greatly facilitated the progress of my academic journey.

My appreciation extends to Mr. Lalin Kothalawala and Dr. Dharshana Muthumuni from Manitoba Hydro International fort their valuable suggestions and support throughout the program.

I gratefully acknowledge the technical and IT assistance provided by Mr. Shrimal Koruwage, whose support was crucial during the research process.

Special thanks go to all my friends for their encouragement and companionship. I am deeply grateful to my loving husband, father, mother, and brother for being my unwavering source of strength and support every single day.

Finally, I would like to thank everyone who contributed in any way to the successful completion of this research.

Dedications

To my family !

Contents

List of Tables

List of Figures

List of Abbreviation

PV	Photovoltaic
STC	Standard Test Conditions
NOCT	Normal Operating Cell Temperature
PLL	Phase-Locked Loop
DSOGI-PLL	Double Second Order Generalized Integrator Phase-Locked Loop
SRF-PLL	Synchronous Reference Frame Phase-Locked Loop
RMSD	Root Mean Square Deviation
NRMSD	Normalized Root Mean Square Deviation
BiFi	Rear Irradiance-Driven Power Gain Yield
SCR	Short-Circuit Ratio
PPC	Power Plant Controller
MPP	Maximum Power Point
MPPT	Maximum Power Point Tracking
PCC	Point of Common Coupling
TSO	Transmission System Operator
FFPS	Fundamental Frequency Positive Sequence
BES	Bulk Electric System
DER	Distributive Energy Sources
RSTC	Reliability and Security Technical Committee
NERC	North American Electric Reliability Corporation
FRT	Frequency Ride - Through
VRT	Voltage Ride - Through
ROCOF	Rate of Change of Frequency

FFR	Fast Frequency Response
QSG	Quadrature Signal Generator

Chapter 1

Introduction

This chapter outlines the current state of solar energy technology, identifies the pressing challenges, and delineates the research objectives aimed at addressing these issues through the development and validation of comprehensive simulation components for Solar photovoltaic (PV) systems. The chapter concludes with an overview of the organization of the thesis.

1.1 Background

The global energy landscape is undergoing a profound transformation, with renewable energy sources, particularly solar power, at its core. This transformation is driven by the need to mitigate climate change impacts and reduce dependence on fossil fuels [1], [2]. Solar PV energy systems, capable of converting sunlight directly into electricity, are crucial in this transition. However, integrating them into the power grid introduces a range of technical challenges. These include the need for accurate PV module models that can predict performance under varying environmental conditions, and the ability to maintain grid stability during disturbances. In order to design robust solar PV energy systems, simulation studies, typically performed in electromagnetic transient (EMT) simulators, are essential. EMT simulation models capable of precisely simulating the performance of solar PV modules together with the other components involved in the converters and control

systems are required for this purpose. This thesis addresses the challenges of solar energy integration by focusing on accurate PV module modeling and advanced inverter control strategies to enhance grid stability under disturbances and intermittency.

1.1.1 Accurate Modeling of Solar Modules

Photovoltaic energy conversion relies on semiconductor solar cells, often silicon-based, to harness the photovoltaic effect. The electrical performance of a PV cell is typically characterized by the current-voltage (I-V) curves. When analyzing the impact and performance of solar PV energy system embedded in a power system, the system needs to be simulated together with the power system. In power system simulators, PV cells or modules are represented through their electrical models. However, the nonlinear nature of the I-V curves makes implementing the models of PV cells in power system simulators without significantly slowing the simulation speed a challenging task. Another challenge is the determination of accurate parameters required for the models of solar PV modules relying on the limited information available in the manufacturer datasheets. Robust model parameters are important to ensure simulation stability and the accuracy of simulations, which is essential for predicting power output and optimizing system design [3]. This is especially true for bifacial modules, which capture sunlight from both sides and offer enhanced energy yield potential. Modeling bifacial modules introduces additional complexities due to their increased sensitivity to partial shading. Therefore, developing robust simulation models for both monofacial and bifacial PV modules is vital for improving performance predictions and studying their integration into power grids.

1.1.2 Inverter Controls Amidst Disturbances and Solar Intermittency

Integration of PV systems into the electrical grid requires advanced control mechanisms that incorporate precise frequency measurement and phase detection. These capabilities are crucial for ensuring synchronization of inverters with the grid and controlling their output active and reactive powers as desired. The most prevalent techniques for achieving this synchronization include Phase-Locked-Loops (PLL) and Discrete Fourier Transform (DFT) techniques. Inverter control systems typically employ decoupled control strategies, which needs continuous measurements of the voltage phase angle at the Point of Common Coupling (PCC). Inverter control systems heavily rely on the efficacy of the PLL measure the phase angles. However, the conventional approaches used to implement PLLs often face challenges in maintaining precision during grid disturbances such as transient faults, which can lead to potential stability problems, particularly in scenarios where the grid is inherently weak [4]. The ability to identify the phase swiftly and accurately during transient conditions becomes critically important in the context of decoupled control systems. Additionally, the significance of accurate frequency measurement becomes more distinct in the implementation of power frequency control, which is vital for ensuring a balance between electricity supply and demand as well as for keeping the operational frequency within prescribed limits. Thus, enhancing the accuracy of frequency measurement in inverters is fundamental to improving grid stability, a necessity that becomes even more critical given the variable nature of solar power generation [5].

Moreover, enhancing the primary frequency response of the power grid is vital for responding to rapid changes in electricity demand or supply. One of the main disadvantages of renewable energy sources, such as solar and wind, without battery storage, is their

inability to support the grid during under-frequency scenarios as effectively as synchronous generators. This limitation stems from the intermittent nature of renewable energy sources, which do not produce a constant and predictable output, and the tendency to operate the solar PV modules at the maximum power point to maximize the economic benefits. In the context of grid stability, synchronous generators play a crucial role by providing inertia and damping, which help to maintain frequency within acceptable limits following disturbances. Renewable energy sources, on the other hand, are typically connected to the grid via inverters that do not inherently provide these inertia effects. This discrepancy can lead to challenges in maintaining grid frequency stability, especially as the penetration of renewable energy in the power mix increases [6], [7]. The concept of grid forming inverters that can provide virtual inertia is emerging as a solution; however, a majority of inverters still depend on the grid following controls [8].

1.2 Problem Statement

1.2.1 Accurate Modeling of Solar Modules

Accurate modeling of solar PV modules is critical for performance evaluation, system design optimization, and integration into power grids. However, challenges arise due to the nonlinear nature of the I-V characteristics of PV cells and the limited data provided in manufacturers' datasheets, which often lack essential electrical model parameters. This gap hinders precise representation of PV modules in simulation studies, affecting the reliability of the models.

Existing parameter extraction methods for the Single Diode Model (SDM), which is a widely adopted and practical approach for modeling monofacial PV modules, encounter significant challenges in terms of robustness and efficiency. These methods often rely on complex numerical algorithms or oversimplified assumptions, resulting in inaccuracies, convergence failures, or unrealistic parameter values. Additionally, Current approaches overlook variations in ideality factors (Ai) and struggle to incorporate accurate irradiance and temperature dependencies [9], [10], [11].

The rise of bifacial PV modules, which utilize both front and rear irradiance to enhance energy capture, introduces additional complexities. While the SDM has been extensively used for monofacial PV modules, its application to bifacial PV modules, which capture energy from both front and rear surfaces, remains underexplored. Challenges arise in modeling bifacial-specific characteristics, such as bifacial gain and partial shading effects, which are influenced by environmental conditions and structural features like junction boxes. The absence of a reliable approach to model partial shading reduces the accuracy of performance predictions, limiting the optimization of bifacial PV systems [12].

Thus, there is a need for advanced, robust and accurate modeling techniques for both monofacial and bifacial PV modules. These methods should utilize limited manufacturer data effectively, incorporate environmental dependencies, and address the specific characteristics of each module type, enabling precise simulation, control design, and performance evaluation in real-world PV system applications.

1.2.2 Enhancing Grid Stability Amidst Disturbances

In the process of integration of renewable energy sources, notably solar power, into the electrical grid, it is imperative to ensure the grid stability amidst various disturbances and solar intermittency through effective control of inverters. As mentioned earlier, PLLs plays major role in preserving the stability of inverter control. Traditional methods of determining grid frequency and phase such as PLL, DFT, and Zero Crossing detection, face significant challenges, specailly under weak grid conditions. These traditional mechanisms often fail to accurately and promptly detect grid phase and frequency during transient conditions. These mechanisms often assume linear, steady-state conditions and are not equipped to handle the complexities of non-ideal grid scenarios, which include rapid dynamic changes such as phase jumps, presence of noise and harmonics, and deviations from perfect sinusoidal waveforms. Their slow response to these conditions compromises their ability to provide precise and reliable measurements, highlighting the need for more resilient and adaptive measurement and control technologies in modern power systems. This was confirmed by the Blue Cut Fire event on August 16, which revealed the deficiencies in inverter control and PLL systems in providing precise grid frequency measurements during transient scenarios. An instance of this issue was when a solar inverter incorrectly reported the grid frequency as 54.5 Hz, despite the actual frequency being 59.867 Hz during a line-to-line fault. The incorrect frequency measurement stemmed from distortion in the voltage waveform, which experienced a phase jump of -26 degrees [13]. This inaccurate frequency reading led to unnecessary shutdowns of inverters. Such a chain of events triggered a significant power outage, estimated at around 700 MW, thereby emphasizing the grid's sensitivity to transient

disruptions. In reaction to such events and the inadvertent disconnections due to incorrect frequency detection, NERC suggested a provisional remediation plan [13], [14]. This plan recommended that inverter manufacturers and utility companies implement a delay for activating low or high-frequency protective measures to reduce the risk of unwarranted disconnections. Nevertheless, this temporary fix introduces its own challenges, including the potential for delayed responses of inverters to actual critical frequency changes.

Further supporting these concerns are the events of the 2017 Canyon 2 Fire in California, the 2021 Odessa 1 and 2022 Odessa 2 disturbances in Texas, where solar PV plants continued to trip due to PLL loss of synchronism, exacerbated by sudden phase jumps. In 2021, it was observed that solar PV plants were still tripping on PLL loss of synchronism, and these issues were not being properly mitigated. Transmission Operators (TOs), in coordination with their Reliability Coordinators (RC), Balancing Authorities (BA), Transmission Planners (TP), and Planning Coordinators (PC), have not established interconnection requirements to prevent plants from tripping on PLL loss of synchronism. This form of tripping, though not addressed in PRC-024-3, has been identified as a significant cause of solar PV reduction during grid disturbances. The poor tracking capability of PLLs during transient events has led to unreliable performance of a number of large Bulk Electric System (BES), as solar PV resources often fail to provide adequate fault ride-through support. The persistence and growth of this reliability issue and inadequate mitigation has led to the recommendation that the Reliability and Security Technical Committee (RSTC) of the North American Electric Reliability Corporation (NERC) to direct the NERC Inverter-Based Resource Performance Working Group

(IRPWG) to produce a Standard Authorization Request (SAR) to mitigate this issue effectively [5], [13], [15].

Moreover, the 2022 Odessa disturbance highlighted how inverters did not trip on PLL loss of synchronism because many of those protections had been disabled. However, these inverters tripped on a passive anti-islanding function, which misinterpreted the grid phase angle shift upon fault recovery as an islanding signature. The protection system, which compares the angle difference between inverter voltage and current phasors and operates for a change larger than 15 degrees within 500 ms, failed to accurately respond to the grid conditions, leading to further disruptions [15].

Additionally, inaccurate frequency measurements pose a risk of triggering incorrect operational responses from solar power plants during power frequency control processes, potentially leading to further grid instability at crucial times. For example, if the frequency is erroneously reported as high during a fault condition, the inverter controller might attempt to reduce power output. This reaction, is counterproductive in such scenarios where an increase in power supply is actually needed to restore system balance.

Moreover, the challenges faced by solar plants with decoupled control systems, particularly when integrating into weak grids, underscore the critical importance of accurate and rapid phase detection for system stability. Decouple control systens commonly rely on PLL for estimating the phase, which is crucial for the execution of the Park transform, a key component in these control systems. However, the effectiveness of this approach hinges on the precision and speed with which the PLL-based systems can estimate the phase, particularly during transient events. Delayed or inaccurate phase detection can lead to misjudgments in control actions, resulting in system imbalances. In the context of weak

grid conditions, where the system's resilience to disturbances is already compromised, such inaccuracies can escalate to a system collapse [16], [17].

The widespread adoption of Synchronous Reference Frame (SRF) PLL in converter controls, while popular for its effectiveness in steady-state conditions, exhibits significant limitations under non-ideal grid scenarios marked by imbalance and harmonic disturbances [18], [19]. This reliance on SRF PLL technology, despite its known disadvantages in such conditions, poses a risk to overall system stability. It compromises the system's ability to adequately reject disturbances, making it more vulnerable during transient events and less resilient against the challenges posed by weak grids.

Developing more robust and adaptive control strategies is essential for the reliable operation of solar plants. These strategies must be capable of handling rapid phase changes and disturbances. This is particularly important for integrating solar plants into the broader power system in areas served by weak grids.

1.3 Research Objectives

The main objective of this study is to develop and validate comprehensive simulation models for several essential components in solar PV energy systems, focusing on enhancing grid stability amidst transient conditions and solar intermittency. The research is divided into two primary goals, each supported by specific sub-objectives:

1.3.1 Accurate Modeling of Solar Modules

1. Evaluate the methods available for extracting parameters of the SDM from manufacturers' datasheets for monofacial PV modules

2. Adapt the parameter extraction method for the SDM for bifacial PV modules.
3. Enhance the modeling for bifacial modules by incorporating partial shadings into the simulation model.
4. Validate simulation models of both monofacial and bifacial PV modules under various environmental conditions.

1.3.2 Enhancing Grid Stability Amidst Disturbances

1. Develop an advanced PLL to improve phase detection and frequency measurement accuracy during grid transients.
2. Evaluate the performance of the developed PLL using multiple test scenarios.
3. Develop a control strategy for solar inverters to enhance primary frequency response by leveraging reserve capacity.
4. Validate the effectiveness of the developed strategy for improving primary frequency response of a power system with heavy presence of solar PV generation.

1.4 Thesis Organization

Following this introduction, Chapter 2 provides an in-depth review of the literature related to key research areas. It begins with a comprehensive review of PV solar module modeling methods for both monofacial and bifacial modules. The chapter then explores the Frequency Ride-Through (FRT) capabilities of grid-connected PV systems, frequency measurement methods, and inverter technologies, highlighting their associated challenges. Finally, it discusses power reserve control strategies for inverters and concludes with insights into their role in enhancing grid stability.

Chapter 3 examines the parameter extraction methods for PV modules, addressing both monofacial and bifacial configurations. It highlights the use of manufacturer data and experimental results to validate the proposed extraction methods, ensuring accurate modeling and performance prediction under varying environmental conditions.

Chapter 4 focuses on improving grid synchronization techniques through advanced PLL strategies. It begins by reviewing conventional PLL algorithms, such as the Synchronous Reference Frame PLL (SRF-PLL), and introduces the Double Second-Order Generalized Integrator PLL (DSOGI-PLL) as a more robust alternative for grid-connected systems. To enhance the DSOGI-PLL's performance during grid disturbances, two key mechanisms are developed: a transient detection mechanism and an adaptive bandwidth control algorithm. The chapter includes a comprehensive comparison between SRF-PLL, conventional DSOGI-PLL, and the proposed adaptive DSOGI-PLL, demonstrating the relative performance of the modified approach in terms of synchronization accuracy, phase error reduction, and resilience under fault conditions.

Chapter 5 details the development and validation of solar plant systems integrated with the grid and the IEEE 9-bus system. It assesses various test case scenarios to evaluate the proposed advancements. The chapter also focus on developing a power reserve control algorithm to solar plants and shows how it can be used for primary frequency response.

Chapter 6 concludes the thesis by summarizing the key findings and contributions of the research. It provides recommendations for future studies to further improve solar PV module modeling, grid stability, and the integration of solar energy systems into modern power grids.

Chapter 2

Literature Review

This chapter provides an overview of modeling and parameter estimation of PV modules with a focus on both monofacial and bifacial technologies. It highlights the significance of accurate parameter estimation in enhancing PV system performance. Additionally, the chapter addresses grid stability challenges, including FRT requirements, and examines current frequency regulation standards, frequency measurement techniques, and large-scale inverter control systems. The role of power reserve control and associated challenges in maintaining grid stability are also discussed.

2.1 Modeling of Solar PV Modules

2.1.1 Monofacial PV Modules and Bifacial PV Modules

PV modules have evolved significantly to enhance efficiency and adapt to diverse environmental conditions. Monofacial PV modules, which absorb sunlight from a single side, have been the standard in the solar industry. However, bifacial PV modules have gained prominence due to their ability to capture reflected and scattered light on both sides, leading to higher energy yield per unit area. Studies indicate that bifacial modules can increase energy production by 10–30% compared to their monofacial counterparts, depending on installation conditions such as albedo and tilt angle [20]. The modeling of these modules must consider factors like shading effects, ground albedo, and the angular

response of bifacial cells, making their characterization more complex but rewarding in terms of output prediction.

2.1.2 Equivalent Circuit Models for Monofacial and Bifacial PV Modules

While monofacial PV modules have been extensively studied and modeled, the same cannot be said for bifacial modules. The complex interaction between incident light, surface albedo, and the reflection of sunlight from various surroundings makes bifacial PV module behavior considerably more intricate to predict accurately. The existing modeling methods, initially designed for monofacial cells, often fall short in encapsulating the specific characteristics of bifacial technology [12]. Nevertheless, monofacial PV module models remain a crucial foundation for further development.

In the literature, monofacial PV cell models are categorized into four main types: Ideal SDM, SDM, Double-Diode Model (DDM), and Triple-Diode Model (TDM) as illustrated in Figure 2.1 [3].

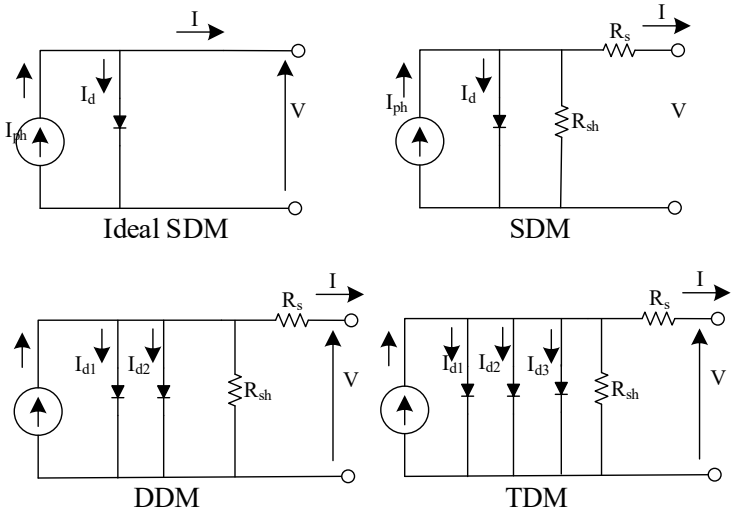

Figure 2.1 Monofacial PV cell models

Among these, the TDM and DDM are known for their high accuracy, as they incorporate additional parameters to account for complex physical phenomena such as recombination losses. However, this increased accuracy comes at the cost of greater complexity. For instance, the DDM requires seven parameters, compared to five in the SDM, making the parameter estimation process more challenging [3], [21].

Despite the higher accuracy of the DDM and TDM, the added complexity does not always translate to significantly better performance predictions in most practical scenarios. As a result, the SDM is widely favored for modeling applications due to its balance between simplicity and accuracy, making it suitable for the majority of situations [22], [23]. Regardless of the chosen model, the precise extraction of PV module parameters is essential for reliable simulations, particularly for control design and performance evaluation. Additionally, the dependence of PV module parameters on environmental factors such as temperature and irradiance necessitate the inclusion of these dependencies in modeling efforts. Incorporating these variations ensures that the models accurately reflect real-world performance under dynamic operating conditions [24].

The rear side of a bifacial PV module can be treated as an additional current source. Models like the SDM can be adapted for bifacial modules by including separate photocurrent sources for the front and rear surfaces, as outlined in the IEC 60904-1-2 standard [25]. One research study proposed an equivalent circuit for bifacial modules, representing them as two parallel-connected monofacial PV module [26]. The equivalent circuit used in this model is shown in Figure 2.2. Advanced approaches include the use of Double Single-Diode Models (D-SDM) in parallel or Double Double-Diode Models (D-DDM). The D-

DDM approach, while offering higher accuracy in low irradiance conditions, introduces additional parameters, significantly increasing the complexity of the models [27], [28].

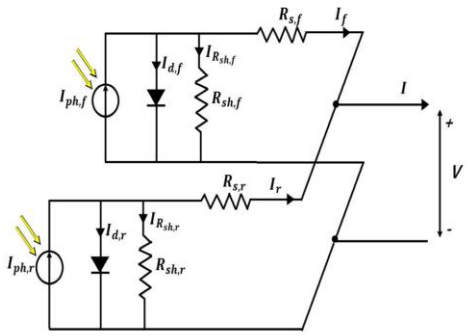

Figure 2.2 Equivalent circuit for a bifacial solar cell [26]

These complexities pose challenges for parameter extraction, especially when relying on limited information, such as manufacturers' datasheets. This highlights the need for more efficient and robust parameter estimation techniques that leverage simplified equivalent circuits without compromising accuracy.

2.1.3 Parameter Estimation Methods for PV Electrical Models

Researchers typically rely on two primary data sources to estimate the parameters of a solar PV module [29], [30], [31].

1. **Experimentally Measured I-V Curves:** These provide detailed and accurate data but require controlled environmental conditions and expensive equipment, such as sun simulators, which may not always be accessible.
2. **Manufacturer's Datasheet Information:** This includes key parameters, such as voltage and current, at Standard Test Conditions (STC) and Normal Operating Cell Temperature (NOCT). While less precise than experimental measurements,

datasheets are widely used due to their availability and practicality for researchers and designers in the PV industry.

As a result, many parameter estimation techniques focus on extracting parameters from datasheet information to address the challenges of limited experimental resources.

Various methods have been proposed to determine the unknown parameters of PV modules by analyzing I-V curves measured under different operating conditions. These methods are broadly classified into analytical techniques, numerical techniques, and evolutionary algorithm techniques [32]. Each method has distinct advantages and limitations, as described below [9], [10], [11] .

Analytical methods use mathematical equations and simple calculations to estimate parameters. They are computationally efficient and ideal for rapid parameter extraction under standard conditions. Techniques such as the Lambert W-function have been combined with parameter extraction algorithms to address the nonlinearity of the Shockley equation, producing explicit analytical equations for PV models [33], [34]. However, these methods often simplify parameters, leading to reduced accuracy in dynamic conditions, such as varying irradiance or temperature. Despite advances, analytical methods can still produce unrealistic parameter values in some scenarios, highlighting ongoing challenges in the field.

Numerical methods employ iterative optimization algorithms, like Newton-Raphson and Bisection algorithms, to refine parameter values for greater accuracy [35], [36]. These methods are suitable for handling complex PV models but are highly sensitive to initial values and prone to convergence failures. Additionally, while numerical techniques

provide robust solutions, the computational demands and the risk of producing unrealistic results remain significant limitations.

Evolutionary algorithms leverage heuristic optimization techniques, such as genetic algorithms and Particle Swarm optimization, to search for global solutions. These methods are especially effective under dynamic conditions like partial shading. However, their computational demand and requirement for careful tuning make them resource intensive [9], [10].

The use of a combination of analytical and numerical techniques has been observed to be more efficient in terms of computational time compared to other standalone techniques [37]. An advanced method has been proposed to consider multiple points on the P-V curve, reducing dependency on initial conditions. However, such methods require a curve extractor to obtain data points from I-V curves in datasheets, which can be inconvenient and introduce errors [38]. Despite these efforts, the issue of determination of the PV parameters remains an ongoing challenge in the field as algorithms sometimes fail to converge or produce unrealistic parameter values.

2.2 Grid Stability Challenges and Frequency Ride-Through Capability Requirements

2.2.1 Frequency Regulation Standards and Grid Codes

Grid frequency stability is maintained through regulatory standards that outline permissible frequency deviations, recovery times, and operational modes. These standards vary across regions to reflect differing grid operational requirements. For instance, the European

Network of Transmission System Operators for Electricity (ENTSO-E) defines detailed frequency regulation standards for Great Britain, Continental Europe, the Nordic system, and the all-island Irish System. Table 2.1 summarizes these standards, highlighting acceptable frequency deviation ranges and recovery protocols [39].

Table 2.1 ENTSO-E network code: frequency standards

	Great Britain (GB)	**The continental Europe (CE)**	**The inter-Nordic system (NE)**	**The all-island Irish system (IRE)**
Standard frequency deviation range	± 0.2 Hz	± 0.05 Hz	± 0.1 Hz	± 0.2 Hz
Maximum instantaneous frequency deviation	0.8 Hz	0.8 Hz	0.8 Hz	0.8 Hz
Maximum steady state frequency deviation	0.5 Hz	0.2 Hz	0.5 Hz	0.5 Hz
Frequency recovery range	± 0.5 Hz	not used	not used	± 0.5 Hz
Time to recover frequency	60 s	not used	not used	60 s
Frequency restoration range	± 0.2 Hz	not used	± 0.1 Hz	± 0.2 Hz
Time to restore frequency	600 s	900 s	900 s	1200 s

As the integration of PV systems into modern power grids accelerates, maintaining grid stability during transient events has become a critical challenge. Unlike conventional synchronous generators, inverter-based PV systems lack inherent inertia, which limits their ability to resist frequency deviations. Consequently, advanced control mechanisms and FRT capabilities have become essential to ensure stable grid operation [40]. Table 2.2 summarizes the FRT requirements for Distributive Energy Sources (DER) according to IEEE Std 1547-2018 [41].

Table 2.2 Frequency ride-through requirements for DER

Frequency Range (Hz)	Operating Mode	Minimum time (s)
> 62.0	Not required to stay connected	N/A
61.2 – 61.8	Mandatory Operation	299 seconds
58.8 – 61.2	Continuous Operation	Indefinite
57.0 – 58.8	Mandatory Operation	299 seconds
< 57.0	Not required to stay connected	N/A

2.2.2 Frequency Measurement Techniques

Accurate frequency measurement is a prerequisite for implementing various measures such as FRT control designed to preserve grid stability. Various techniques have been developed to address challenges posed by non-ideal grid conditions such as harmonics, noise, and voltage disturbances. Below is a comprehensive review of frequency measurement techniques.

Zero-Crossing method is one of the simplest and most widely used techniques for measuring the frequency of a periodic signal. It works by detecting the time intervals between consecutive zero-crossings, points where the signal crosses the zero-voltage level. As illustrated in Figure 2.3 and represented by (2.1) the frequency (*f*) is calculated using the time difference between two successive zero-crossings.

$$f = \frac{1}{2.(t2 - t1)} \tag{2.1}$$

Where:

- t2-t1 the time between successive zero crossings.

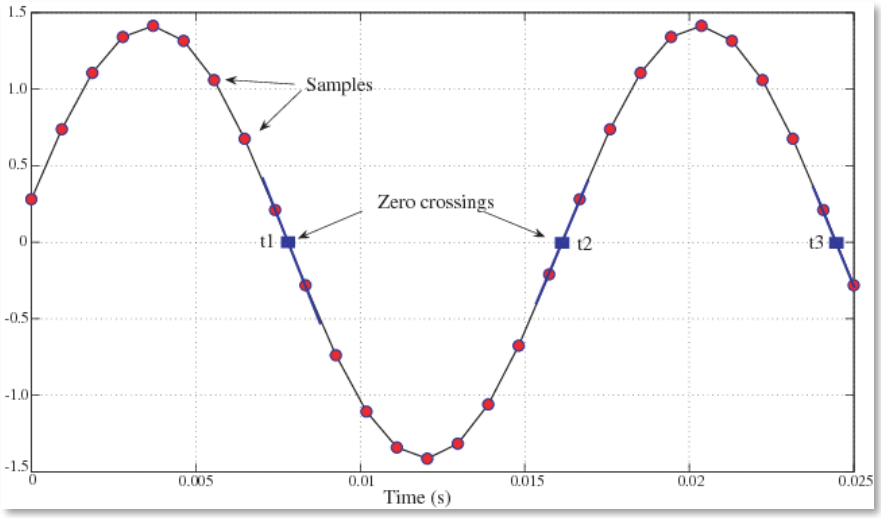

Figure 2.3 Zero crossing detection for frequency estimation[42]

Its simplicity and low computational cost make it popular for basic frequency measurement. However, its accuracy can be compromised by harmonics, noise, and quantization errors. Enhancements like polynomial curve fitting and moving average filters improve precision but increase complexity and latency. Furthermore, its slow response to frequency changes limits its effectiveness in dynamic scenarios, requiring supplementary techniques to enhance reliability [42], [43].

DFT is a widely employed method in power systems for the calculation of voltage and current phasors, particularly for estimating the fundamental frequency phasors of a signal. The voltage phasor V_k is derived from the fundamental frequency component of the DFT algorithm using the sequential data of the instantaneous voltage v. The calculation is expressed as in (2.2):

$$V_k = \sqrt{\frac{2}{N}} \sum_{n=0}^{N-1} v(\mathrm{k} + \mathrm{n} - \mathrm{N} + 1) e^{-\frac{j2\pi n}{N}} \tag{2.2}$$

Where:

- N is the number of samples in one cycle,
- k is the index of the last sample in the data window,
- $e^{-\frac{j2\pi n}{N}}$ represents the complex exponential term in the Fourier transform.

The resulting phasor, V_k , rotates in the complex plane with an angular velocity determined by the signal frequency (*f)* which can then be derived from the phase angle difference between consecutive phasors as shown in (2.3).

$$f = \frac{1}{2\pi} \frac{\arg[V_{k+1}] - \arg[V_k]}{\Delta t} \tag{2.3}$$

It is particularly effective in steady-state conditions but is prone to leakage errors when the signal frequency does not align with discrete frequency bins. Techniques like variable sampling rates, adjustable data windows, and re-sampling address these errors but introduce computational demands and feedback loop delays. Despite these challenges, DFT remains highly valuable for applications requiring simultaneous estimation of phasors, harmonics, and frequency.

In addition to these several advanced techniques are employed for frequency measurement in power systems. **Orthogonal decomposition** involves breaking down a signal into orthogonal components, such as sine and cosine, to estimate frequency. It offers high accuracy but requires precise filter design and can struggle with unbalanced systems [44].

Signal demodulation simplifies frequency estimation by modulating the input signal with a reference and extracting the low-frequency component using a low-pass filter, providing simplicity but requiring careful filter design [45], [46]. **Least Squares Estimation** involves fitting a model to the signal data to estimate frequency, minimizing the sum of squared errors, which offers high accuracy but can be computationally intensive. **Wavelet Transform** analyzes signals at multiple scales, making it suitable for detecting transient events and non-stationary signals, though it requires complex computations[47], [48], [49]. **Prony Analysis** models the signal as a sum of damped exponentials, enabling the extraction of modal information such as frequency, damping, and amplitude, effective for analyzing signals with damped oscillations but sensitive to noise [50]. **Artificial Intelligence Techniques**, including machine learning algorithms and neural networks, have been applied to frequency measurement, offering adaptability to complex and non-linear system behaviors, though they require substantial training data and computational resources[51], [52]**. Taylor approximation estimates frequency** by expanding signal models into a series, suitable for small variations but less effective for large deviations and transients [53]. **Numerical analysis** methods are computationally efficient and provide high accuracy through predefined calculations without iteration. However, they have limitations, including sensitivity to noise, reliance on high-quality and uniform sampling, and reduced adaptability to changing signal conditions [54]. Each method presents a balance between accuracy, computational complexity, and sensitivity to noise and harmonics, with the choice depending on specific application requirements, including the need for real-time processing and the dynamic nature of the power system.

Most inverter control systems rely on PLLs for frequency and phase synchronization due to their effectiveness in maintaining grid stability. By accurately locking onto the grid's frequency and phase, PLLs are integral to providing synchronized reference frames, such as the dq-frame, which is essential for decoupling and independently controlling active and reactive power. Among these, the SRF-PLL is widely used because of its simplicity and ease of implementation. However, SRF-PLL performance can degrade under non-ideal grid conditions, such as unbalanced voltages or harmonic distortion, leading to challenges in accurately tracking the grid's frequency and phase. This compromises system stability and reduces disturbance rejection capabilities, making it less robust against issues like voltage sags, swells, and harmonic distortions [55], [56]. In literature many PLLS have been introduced with different modifications. Most of these PLL algorithms attempt to extract the fundamental frequency positive sequence (FFPS) of the grid voltage and track phase using the SRF-PLL. Brief comparison of different types of PLLs is given in Table 2.3.

Table 2.3 Comparison of Different PLL improvement Techniques

PLL	Merits	Demerits
Low Pass Filter based PLL [19], [57], [59]	• Simple to implement • High noise immunity • Improves stability • Introduced variable phase shifts in filtered signal.	• Slow dynamic response
Moving Average Filter (MAF) - PLL[19]	• High filtering capability • Less computational burden • High noise immunity	•Low disturbance ejection • No harmonic extraction • Slow dynamic response
Notch Filter based PLL [19], [57]	• High disturbance rejection • High filtering capacity • Fast dynamic response • Highly immune to noise	• No harmonic extraction •High computational burden
Delayed Signal Cancellation (DSC)-Based PLL [19]	• Average for disturbance rejection • High filtering capability • Low computational burden • Highly immune to noise	• No harmonic extraction • Slow dynamic response
Complex-coefficient-filter (CCF) based PLL [58], [59]	• High disturbance rejection • High filtering capacity • Can extract harmonic • Fast dynamic response • Highly immune to noise	•High computational burden

PLL	Merits	Demerits
Double Second-Order Generalized Integrator PLL (DSOGI-PLL) [19], [57]	• High disturbance rejection • High filtering capacity • Can extract harmonic • Fast dynamic response • Highly immune to noise • Suitable in voltage unbalance	• High computational burden
Decoupled Double Synchronous Reference Frame PLL – (DDSRF PLL) [58]	• Stable • High harmonics filtering • Suitable in voltage unbalance • Low computational complexity • Eliminate DC offset	• Moderate implementation complexity • Not suitable for frequency variation

Compared to other PLLs proposed in the literature, DSOGI-PLL offers significant advantages with fewer drawbacks. However, despite advancements in PLL techniques, a comprehensive solution that addresses key challenges remains warranted. Reducing the impact of harmonics, improving noise immunity, and enhancing disturbance rejection capabilities are crucial for robust performance in non-ideal grid conditions. Additionally, minimizing frequency oscillations during transients and improving phase tracking speed are essential for dynamic stability and responsiveness. Integrating these improvements into a single, optimized PLL algorithm could greatly enhance the performance and reliability of inverter-based systems, particularly in diverse and challenging operational scenarios.

2.2.3 Control System Architecture and Challenges in Large-Scale Solar PV Plants

The basic structure of the control system for a large-scale solar power plant is illustrated in Figure 2.4. At the core of this system is the Power Plant Control (PPC), which functions as the master controller. It gathers measurements from the PCC and issues commands to various devices, including inverters, Flexible AC Transmission Systems (FACTS), and capacitor banks. During regular operations, inverters adhere to PPC instructions via their internal controls. However, in Voltage Ride Through (VRT) scenarios, inverters bypass PPC commands to respond swiftly, aligning with grid codes to prevent non-compliance due to communication delays during faults [59].

PV power plants must meet several grid code requirements. For voltage regulation, this includes managing reactive power setpoints, implementing voltage regulation via droop curves, and adhering to power factor setpoints as specified by the Transmission System Operator (TSO). Frequency regulation involves TSO directed active power curtailment and frequency management through droop curves, with potential contributions from energy storage systems. During FRT events, plants must dynamically inject active power and maintain grid connection for specified durations. Additionally, ramp rate restrictions control the variation in active power during transitions, with energy storage systems providing flexibility. These requirements ensure compliance with grid codes, focusing on voltage and frequency stability, fault response, and ramp rate management, thereby facilitating the smooth integration of large-scale PV plants into the power grid [14], [60].

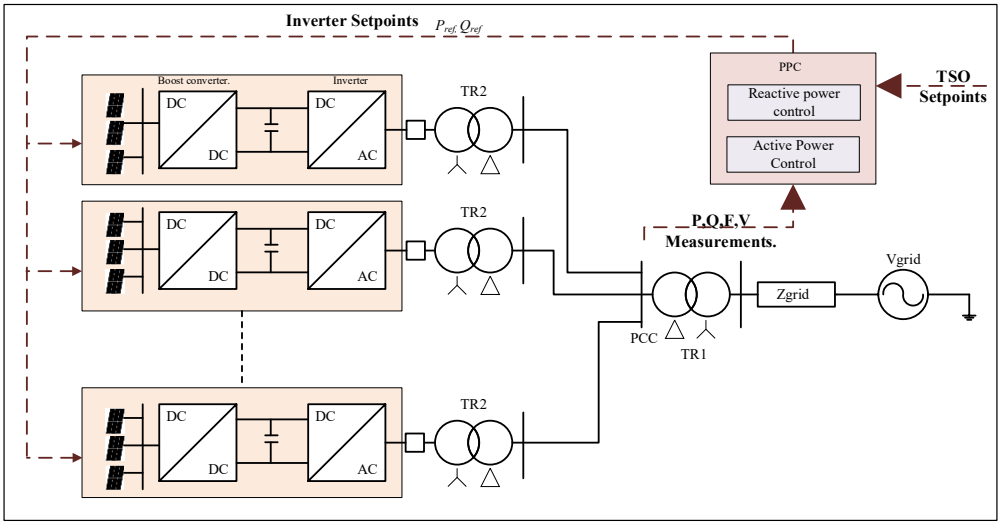

Figure 2.4 Basic inverter control diagram

Figure 2.5 shows the active power control of the PPC. This Power reference can be given to each inverter. Inverters can operate according to the PPC, but if the inverter can't produce the amount there will be problem. So, to avoid such scenarios, the individual inverter can take the minimum power reference out of the reference given by the PPC and the Maximum Power Point (MPP) of the inverter.

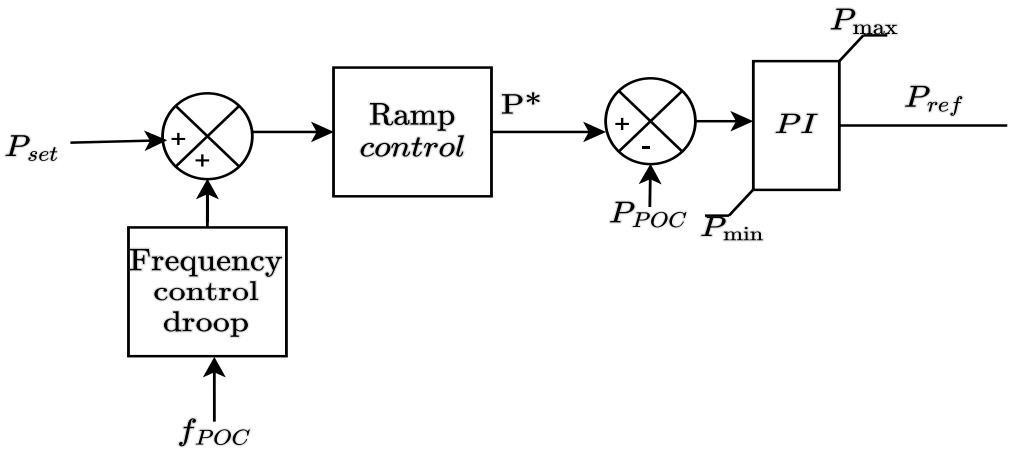

Figure 2.5 Active power control.

Reactive power (Q_{ref}) can be provided as a set value Q_{set}, or Q can be calculated to maintain voltage at the PCC or a specific power factor. The user can select between these control modes, with the PPC assigning the Q_{ref} command to each inverter. A controller to give the Q_{ref} is shown in Figure 2.6.

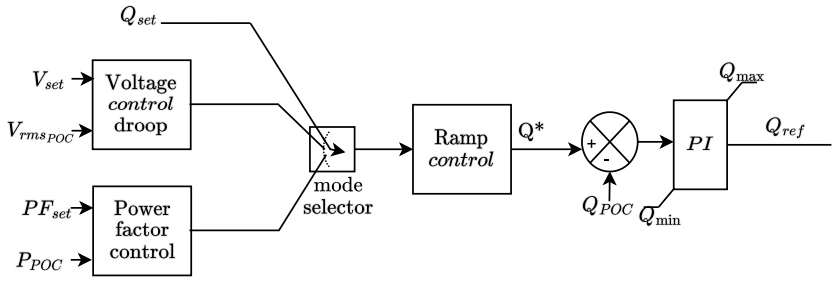

Figure 2.6 Reactive power control

In grid-connected photovoltaic systems, inverter control architectures are commonly classified into single-stage and dual-stage configurations. In single-stage systems, the photovoltaic array is directly interfaced with the grid-side inverter, and both maximum power point tracking and grid power control are performed within a single power conversion stage. Such architectures are widely adopted in high-power industrial applications due to their higher efficiency and reduced component count [61].

In contrast, dual-stage inverter systems employ an additional DC–DC conversion stage between the PV array and the grid-side inverter, allowing independent control of the PV operating point and the DC-link voltage. Figure 2.7 illustrates the dual stage control system for a single inverter within the solar plant. Both P_{ref} and Q_{ref} are fed to individual inverters, enabling each inverter to independently manage its active and reactive power while adhering to the PPC instructions and its MPP (P_{mppt}). This two-stage setup comprises a boost converter and an inverter controller, each with specific control objective. For the

boost converter, the control objective is to select the minimum of the P_{ref} from the PPC or the P_{mppt} and maintain that power level. This ensures optimal utilization of the PV system while aligning with grid requirements. For the inverter controller, the primary goals include maintaining the DC-link voltage at a constant reference value and managing the Q_{ref}. The system utilizes a decoupled control strategy to manage active and reactive power independently [62], [63].

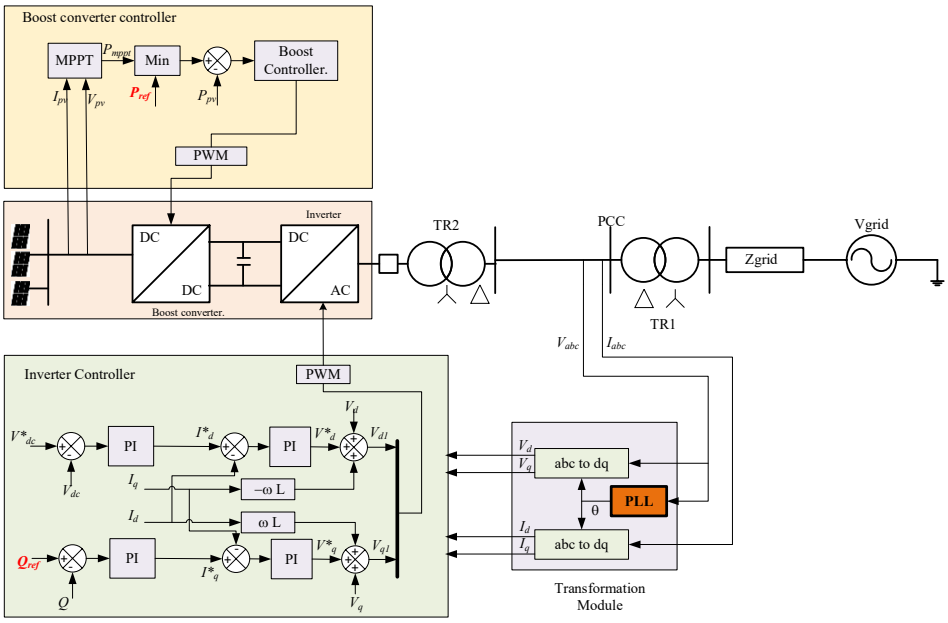

Figure 2.7 Dual stage grid tied inverter control system

A key component in this control structure is the PLL, which plays a vital role in the control system. The PLL provides the phase angle (θ) for abc-to-dq transformations, which are essential for the operation of the decoupled controllers. The accuracy and reliability of the PLL are critical, especially during transients, as the PPC's power-frequency control often relies on the frequency measured by the PLL. Accurate frequency measurement is essential to ensure stability and compliance with grid codes during dynamic events. Without a

properly functioning PLL, the system's performance can be severely compromised [16], [17].

2.2.4 Power Reserve Control of Inverters

The increasing penetration of inverter-based resources in modern power grids has led to a reduction in system inertia, thereby increasing the rate of change of frequency (ROCOF) following generation or load disturbances. This shift necessitates faster responding resources to arrest frequency deviations and stabilize the grid. Fast Frequency Response (FFR) refers to the rapid energy injection or demand reduction to support grid stability. Sources of FFR include synchronous machine inertia, fast-responding inverter-based resources (such as wind, solar PV, and batteries), automatic load tripping, and non-sustained energy extraction from wind turbine rotors [14].

Given these dynamics, maintaining a power reserve in solar plants is particularly beneficial for grids with high inverter-based resource penetration. A power reserve allows PV inverters to provide primary frequency response and contribute to FFR, enhancing grid reliability. Power point tracking can be performed on either side of the MPP, referred to as points A or B, as illustrated in Figure 2.8 [64].

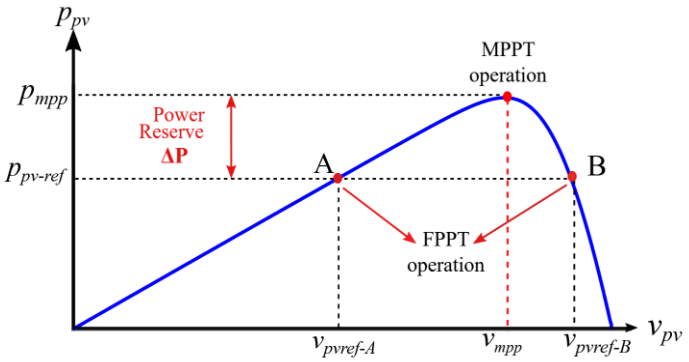

Figure 2.8 PV curve showing MPP and FPPT [64]

Various algorithms have been developed to determine the available power in PV systems under operation. These include the following approaches [64], [65], [66].

- **Utilizing solar forecasting data** combined with PV array characteristics provides a predictive approach but heavily relies on the accuracy of weather forecasts, which may falter during sudden environmental changes.
- **Measurement-based techniques**, using sensors to measure irradiance, temperature, voltage, and current, offer real-time accuracy but increase system complexity and costs due to additional hardware requirements.
- **Artificial Intelligence -based techniques**, which utilize meteorological data and historical operation records, provide robust predictions but require significant computational resources and access to large datasets.
- **Curve-fitting approaches** use PV characteristic curves to estimate power, offering simplicity but limited adaptability to dynamic changes in environmental conditions.

- O**perating a small PV unit in MPPT mode** to approximate total available power is a practical method but assumes uniform environmental conditions across the array

Recent grid codes and standards now require PV power generators to provide frequency support through power reserve control [67], [68]. While Power reserve control significantly improves grid stability and ensures compliance with grid regulations, further research is necessary to evaluate its impact on primary frequency response and to develop simplified mechanisms for integrating MPPT within power reserve control systems. This would enhance system reliability in diverse grid conditions.

2.3 Chapter Summary

This chapter reviewed research on modeling and parameter estimation of PV modules and FRT capability addressing key problem statements.

Monofacial and bifacial PV modules both face modeling challenges. Monofacial models, despite extensive study, struggle with robustness and accuracy using only manufacturers' datasheet information. SDM is identified as a simple and effective model for both types of modules, but bifacial modules require further improvements due to the complexity of dual-sided light capture. The limitations of existing methods for extracting parameters of PV modules have been identified, highlighting the need for more robust and accurate techniques.

PV systems lack inertia, posing challenges in maintaining grid stability during transient events. Existing techniques, including frequency measurement methods and PLL designs,

have limitations in accuracy and robustness under dynamic conditions. DSOGI-PLL is identified as a promising option but requires further improvements.

Power reserve control plays a significant role in enhancing grid stability and ensuring regulatory compliance. However, its influence on primary frequency response remains an area requiring further investigation. Continued research is essential to optimize its integration and fully understand its impact on system dynamics.

Chapter 3

PV module model parameter extraction and incorporation of partial shading effects

3.1 Introduction

The accurate modeling of PV modules is pivotal for simulating and optimizing solar energy systems with the adoption of renewable energy technologies continues to accelerate. Manufacturers typically provide limited data for PV modules under STC and NOCT, and these data do not directly correspond with the parameters needed in the physics-based models such as SDM. Poor parameterization results in inaccurate representation of PV module characteristics in simulations studies, which compounds under dynamic environmental conditions such as partial shading if such effects are poorly modeled.

Traditional models such as the SDM have been widely used to represent PV modules due to their balance between simplicity and accuracy. However, these models often overlook critical aspects like the bifacial characteristics of newer PV technologies and the impact of non-uniform irradiance. The emergence of bifacial PV modules, which utilize both front and rear surfaces for energy generation, introduces additional complexities, including rear-side irradiance and shading effects.

This chapter focuses on addressing these challenges by presenting robust methods for parameter extraction from manufacturer data, extending the SDM to incorporate partial

shading effects, and validating these models with both experimental data and manufacturer specifications. Special attention is given to bifacial PV modules, where an enhanced modeling approach captures unique characteristics such as bifacial gain and shading impacts. Through these advancements, this work contributes to more accurate and reliable modeling of PV systems, enabling better design, integration, and operation of solar energy technologies.

3.2 Monofacial PV Modules

The SDM is one of the most widely used models for representing the electrical behavior of PV cells. It strikes a balance between simplicity and accuracy, making it suitable for various simulation and design applications in solar energy systems. The SDM is represented by a simplified equivalent circuit, as shown in Figure 3.1, which effectively reproduces the I-V curve of a PV cell or module.

This circuit includes the following components:

1. **Photoelectric Current Source (I_{ph})**: Generates current in response to incident sunlight, representing the photocurrent of the PV cell.
2. **Diode**: Models the nonlinear current-voltage characteristics of the p-n junction in the PV cell.
3. **Series Resistance (R_s)** Accounts for resistive losses due to cell solder bonds, interconnections, and junction box materials.
4. **Shunt Resistance (R_{sh})**: Represents leakage currents through high-conductivity shunts across the p-n junction

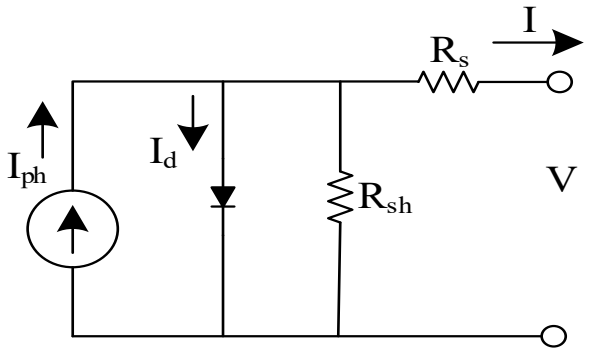

Figure 3.1: Equivalent circuit of a PV module

The diode in the model represents a real diode and is described by the Shockley equation embedded in ((3.1), which relates the PV cell/module terminal current I and voltage V [69]

$$I = I_{ph} - I_o \left[e^{\left(\frac{V+IR_s}{A_i V_T}\right)} - 1 \right] - \frac{V + IR_s}{R_{sh}} \tag{3.1}$$

Where:

- I_o is the diode's reverse saturation current.
- A_i is the ideality factor that incorporates deviations from the Shockley diffusion theory.
- V_T is the thermal voltage of the diode

The V_T is defined by (3.2) is determined by several physical constants and operating conditions. These includes electron charge (q), Boltzmann constant (k), the number of cells in series (Ns), and absolute temperature (T) [33], [70].

$$V_T = N_s \frac{kT}{q} \tag{3.2}$$

3.2.1 Parameter Calculation

The performance of a PV module is commonly represented by it's I-V characteristics, which describe the relationship between the output current and voltage under specified operating conditions. The I-V curve typically features three critical points: the short-circuit current (I_{sc}), the open-circuit voltage (V_{oc}), and the MPP (I_{mpp},V_{mpp}). I_{sc} corresponds to the maximum current generated by the module when the output terminals are short-circuited (V=0) and is directly proportional to solar irradiance while being influenced by the module's temperature. The V_{oc} represents the maximum voltage the module can produce when no current flows (I=0), and it decreases with increasing temperature. The MPP identifies the optimal operating condition where the module delivers its highest power output ($P_{mpp}=I_{mpp}V_{mpp}$), which is critical for efficient energy extraction. These points, alongside other specifications, are typically provided in manufacturer datasheets under standard test conditions STC, characterized by an irradiance of 1000 W/m^2, a cell temperature of 25°C. Additionally, parameters under NOCT, such as an irradiance of 800 W/m^2, an ambient temperature of 20°C, and a wind speed of 1 m/s, offer insights into real-world performance. The shape and position of the I-V curve are influenced by environmental factors like irradiance and temperature, as well as the inherent electrical properties of the module, making these points crucial for understanding and optimizing PV system performance.

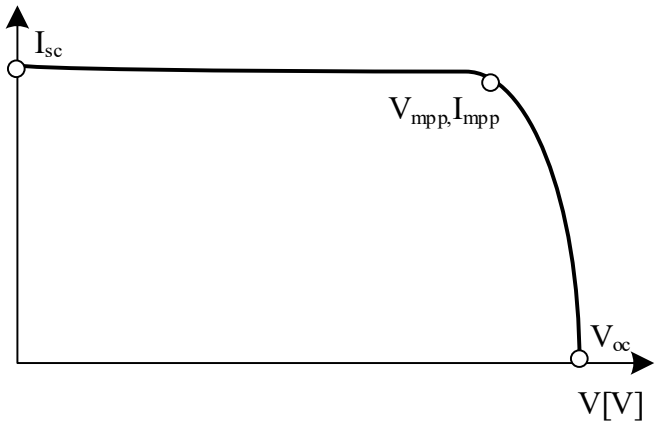

Figure 3.2 Typical I-V characteristics of a PV module

The following is a procedure to determine all required parameters using only the information provided in manufacturer's datasheet, which is a common situation faced in industry when attempting to model a PV array for simulation studies. By substituting the three known points on the I-V curve into (3.1), a set of equations can be derived to extract the necessary parameters of the SDM [33], [70].

For the short-circuit point (I_{sc}), where V=0, the equation is:

$$I_{sc} = I_{ph} - I_o\left[e^{\left(\frac{I_{sc}R_s}{A_i V_T}\right)} - 1\right] - \frac{I_{sc}R_s}{R_{sh}} \tag{3.3}$$

For the open-circuit point (V_{oc}), where I=0, the equation becomes:

$$0 = I_{ph} - I_o\left[e^{\left(\frac{V_{oc}}{A_i V_T}\right)} - 1\right] - \frac{V_{oc}}{R_{sh}} \tag{3.4}$$

At the maximum power point, where the module delivers the maximum power ($P_{mpp}=I_{mpp}V_{mpp}$), the equation is:

$$I_{mpp} = I_{ph} - I_o\left[e^{\left(\frac{V_{mpp}+I_{mpp}R_s}{A_iV_T}\right)} - 1\right] - \frac{V_{mpp} + I_{mpp}R_s}{R_{sh}} \tag{3.5}$$

Power at any point can be obtained by multiplying (3.1) by V:

$$P = VI = VI_{ph} - VI_o\left[e^{\left(\frac{V+IR_s}{A_iV_T}\right)} - 1\right] - \frac{V^2 + \mathrm{V}IR_s}{R_{sh}} \tag{3.6}$$

Then one more equation can be obtained considering the derivative of power–voltage relationship, dP/dV, which is equal to zero at the maximum power point:

$$\left.\frac{dP}{dV}\right|_{V=V_{mpp}} = 0$$

$$0 = I_{ph} - I_o\left[e^{\left(\frac{V_{mpp}+I_{mpp}R_s}{A_iV_T}\right)} - 1\right] - V_{mpp}I_o e^{\left(\frac{V_{mpp}+I_{mpp}R_s}{A_iV_T}\right)}\left(\frac{1 - \frac{I_{mpp}}{V_{mpp}}R_s}{A_iV_T}\right) - \frac{2V_{mpp}}{R_{sh}}) \tag{3.7}$$

Substituting $I_{mpp} = P_{mpp}/V_{mpp}$ on (3.7):

$$0 = I_{ph} - I_o\left[e^{\left(\frac{V_{mpp}+\frac{P_{mpp}}{V_{mpp}}R_s}{A_iV_T}\right)} - 1\right] - V_{mpp}I_o e^{\left(\frac{V_{mpp}+\frac{P_{mpp}}{V_{mpp}}R_s}{A_iV_T}\right)}\left(\frac{1 - \frac{P_{mpp}}{{V_{mpp}}^2}R_s}{A_iV_T}\right) - \frac{2V_{mpp}}{R_{sh}}) \tag{3.8}$$

Maximum power equation can be obtained by multiplying (3.5) by V_{mpp}:

$$P_{mppp} = V_{mpp}I_{mpp} = V_{mpp}I_{ph} - V_{mpp}I_o\left[e^{\left(\frac{V_{mpp}+I_{mpp}R_s}{A_iV_T}\right)} - 1\right] - \frac{{V_{mpp}}^2 + V_{mpp}I_{mpp}R_s}{R_{sh}}) \tag{3.9}$$

Substituting $I_{mpp} = \frac{P_{mpp}}{V_{mpp}}$ to (3.9):

$$P_{mppp} = V_{mpp}I_{ph} - V_{mpp}I_o\left[e^{\left(\frac{V_{mpp}+\frac{P_{mpp}}{V_{mpp}}R_s}{A_iV_T}\right)} - 1\right] - \frac{{V_{mpp}}^2 + \mathrm{P}_{mpp}R_s}{R_{sh}}) \tag{3.10}$$

Substituting I_{ph} from (3.5) and $P_{mpp} = I_{mpp}V_{mpp}$ to equation (3.10):

$$-\frac{I_{mpp}}{V_{mpp}} = -\frac{I_o}{A_iV_T}\left(1 - \frac{I_{mpp}}{V_{mpp}}R_s\right)\left[e^{\left(\frac{V_{mpp}+I_{mpp}R_s}{A_iV_T}\right)} - 1\right] - \left(1 - \frac{I_{mpp}}{V_{mpp}}R_s\right)\frac{1}{R_{sh}} \tag{3.11}$$

From (3.3) - (3.10), it is possible to derive equations as discussed in subsequent paragraphs [33], [70] :

When the PV module is short-circuited (V=0), the photo current (I_{ph}) can be determined using Kirchhoff's Current Law (KCL). The relationship is given by:

$$I_{ph} = I_{sc}\left(1 + \frac{R_s}{R_{sh}}\right) \tag{3.12}$$

Using e (3.4) and (3.12) diode saturation current can be expressed as:

$$I_o = \frac{I_{sc}(R_s + R_{sh}) - V_{oc}}{R_{sh}e^{\left(\frac{V_{oc}}{A_iV_T}\right)}} \tag{3.13}$$

The series resistance can be determined by solving (3.14), which is obtained by (3.11) and substituting $R_{sh} = 1 - I_{mpp}R_s/V_{mpp}$:

$$\frac{A_i V_T V_{mpp}(2I_{mpp} - I_{sc})}{[V_{mpp}I_{sc} + V_{oc}(I_{mpp} - I_{sc})](V_{mpp} - I_{mpp}R_s) - A_i V_T(V_{mpp}I_{sc} - V_{oc}I_{mpp})} = e^{\left(\frac{V_{mpp}+I_{mpp}R_s - V_{oc}}{A_i V_T}\right)} \quad (3.14)$$

The shunt resistance is obtained by (3.4) and (3.11) along with the assumption that $V_{oc} \approx V_{mpp} + I_{mpp}R_s$:

$$R_{sh} = \frac{(V_{mpp} - I_{mpp}R_s)[V_{mpp} - R_s(I_{sc} - I_{mpp}) - A_i V_T]}{(V_{mpp} - I_{mpp}R_s)(I_{sc} - I_{mpp}) - A_i V_T I_{mpp}} \quad (3.15)$$

Equations (3.12)- (3.15) can be solved for R_s, R_{sh}, I_{ph}, and I_o for an estimated value of A_i. However, solving for R_s is not straightforward. It is possible to transform (3.14) into an explicit equation using the Lambert W-function defined in (3.16); where z is a complex number:

$$z = W(z)e^{W(z)} \quad (3.16)$$

For a real variable x, the relation W is defined only for $x \geq -1/e$ and it can be shown as in Figure 3.3.

$$x = W(x)e^{W(x)} \quad (3.17)$$

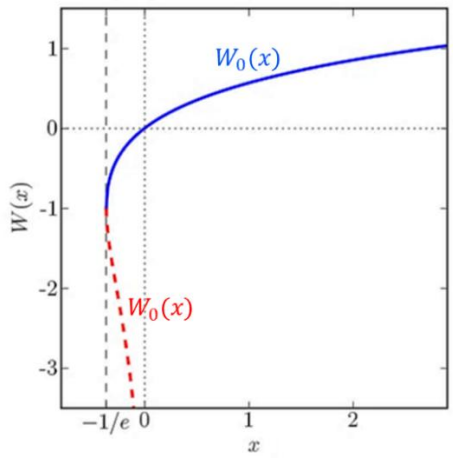

Figure 3.3 Lambert W function for real variable x

Using Lambert W function, it is possible to rewrite (3.14) as:

$$\frac{-V_{mp}(2I_{mp}-I_{sc})}{[V_{mp}I_{sc}+V_{oc}(I_{mp}-I_{sc})]}e^{\left(-\frac{2V_{mp}-Voc}{A_iV_T}+\frac{V_{mp}+I_{mp}R_s-V_{oc}}{(V_{mp}I_{sc}+V_{oc}(I_{mp}-I_{sc}))}\right)} \tag{3.18}$$

$$=\left(\frac{I_{mp}R_s-V_{mp}}{A_iV_T}+\frac{V_{mp}I_{sc}-V_{oc}I_{mp}}{(V_{mp}I_{sc}+V_{oc}(I_{mp}-I_{sc}))}\right)e^{\left(\frac{I_{mp}R_s-V_{mp}}{A_iV_T}+\frac{V_{mp}I_{sc}-V_{oc}I_{mp}}{(V_{mp}I_{sc}+V_{oc}(I_{mp}-I_{sc}))}\right)}$$

Applying the equivalence in (3.17) to (3.18) yields:

$$\left(\frac{I_{mp}R_s-V_{mp}}{A_iV_T}+\frac{V_{mp}I_{sc}-V_{oc}I_{mp}}{(V_{mp}I_{sc}+V_{oc}(I_{mp}-I_{sc}))}\right) \tag{3.19}$$

$$=W_{-1}\left(\frac{V_{mp}(2I_{mp}-I_{sc})}{[V_{mp}I_{sc}+V_{oc}(I_{mp}-I_{sc})]}e^{\left(-\frac{2V_{mp}-V_{oc}}{A_iV_T}+\frac{V_{mp}I_{sc}-V_{oc}I_{mp}}{(V_{mp}I_{sc}+V_{oc}(I_{mp}-I_{sc}))}\right)}\right)$$

Where $W_{-1}(\cdot)$ represents the negative branch of Lambert W function, as the left-hand side of equation (3.18) is lower than -1 for typical solar PV modules. Note that in (3.19), R_s is included only on the left-hand side, and an explicit expression can be obtained for the series resistance R_s as in (3.20) [33].

$$R_s = C_1(W_{-1}(C_2 e^{C_3}) - C_4 - C_3) \tag{3.20}$$

where: $C_1 = \frac{A_i V_T}{I_{mp}}$, $C_2 = -\frac{V_{mp}(2I_{mp}-I_{sc})}{[V_{mp}I_{sc}+V_{oc}(I_{mp}-I_{sc})]}$,

$C_3 = -\frac{2V_{mp}-V_{oc}}{A_i V_T} + \frac{V_{mp}I_{sc}-V_{oc}I_{mp}}{(V_{mp}I_{sc}+V_{oc}(I_{mp}-I_{sc}))}$, $C_4 = \frac{V_{mp}-V_{oc}}{A_i V_T}$

As described, (3.12)- (3.15) enable the determination of R_s, R_{sh}, I_{ph}, and I_o by applying the Lambert W function to a given A_i. The optimum value for A_i can be found through a grid search, that is computing R_s, R_{sh}, I_{ph}, and I_o for different values of A_i in a defined search area and evaluating the fitness of the computed parameters. The fitness of these computed parameters can be assessed using an objective function that considers multiple criteria outlined below:

1. At V_{mpp}, the calculated power should be equal to P_{mpp} given in the datasheet. This gives:

$$f_1(A_i) = V_{mpp}\left[I_{ph} - I_o\left[e^{\left(\frac{V_{mpp}+I_{mpp}R_s}{A_i V_T}\right)} - 1\right] - \frac{V_{mpp}+Ip_{mp}R_s}{R_{sh}}\right] - P_{mpp} = 0 \tag{3.21}$$

2. At V_{mp}, the derivative of output power with respect to voltage should be equal to 0. This gives:

$$\left.\frac{dP}{dV}\right|_{V=V_{mp},I=I_{mp}} = 0 \tag{3.22}$$

$$f_2(A_i) = I_{ph} + I_o - \left(1 + \frac{V_{mp}}{A_i V_T}\right) I_o e^{\left(\frac{V_{mp}+I_{mp}R_s}{A_i V_T}\right)} - \frac{2V_{mp} + I_{mp}R_s}{R_{sh}} = 0 \tag{3.23}$$

3. At $V = 0$, i.e., at short circuit point, the derivative of current with respect to voltage is equal to the negative of the reciprocal of the shunt resistance. This gives:

$$\left.\frac{dI}{dV}\right|_{V=0} = -\frac{1}{R_{sh}} \tag{3.24}$$

$$f_3(A_i) = -\frac{\frac{1}{R_{sh}} + \frac{I_o}{A_i V_T} e^{\left(\frac{I_{sc}R_s}{A_i V_T}\right)}}{1 + \frac{R_s I_o}{A_i V_T} e^{\left(\frac{I_{sc}R_s}{A_i V_T}\right)} + \frac{R_s}{R_{sh}}} + \frac{1}{R_{sh}} = 0 \tag{3.25}$$

4. At V_{mpp}, the calculated current should be equal to I_{mpp} given in the datasheet. This condition yields an alternative expression to $f_1(A_i)$ which can be omitted if desired:

$$f_4(A_i) = I_{ph} - I_o \left[e^{\left(\frac{V_{mpp}+I_{mpp}R_s}{A_i V_T}\right)} - 1\right] - \frac{V_{mpp} + I_{mpp}R_s}{R_{sh}} - I_{mpp} = 0 \tag{3.26}$$

5. The combined objective function to minimize can be defined as:

$$f_{obj}(A_i) = [f_1(A_i)]^2 + [f_2(A_i)]^2 + [f_3(A_i)]^2 + [f_4(A_i)]^2$$

The value of A_i (and the corresponding R_s, R_{sh}, I_{ph}, and I_o) that minimizes $f_{obj}(A_i)$ can be considered the optimum PV module equivalent circuit parameters, at the standard test conditions. By searching over a broader range for 'A_i', this method ensures the avoidance of unrealistic parameters, such as negative shunt resistance values, when using the single-diode PV module equivalent circuit depicted in Figure 3.1. This method leads to optimal 'A_i' values slightly below 1.0 in some cases, while maintaining realistic values for other parameters. The process of estimating the PV module parameters at the standard conditions is shown in Figure 3.4.

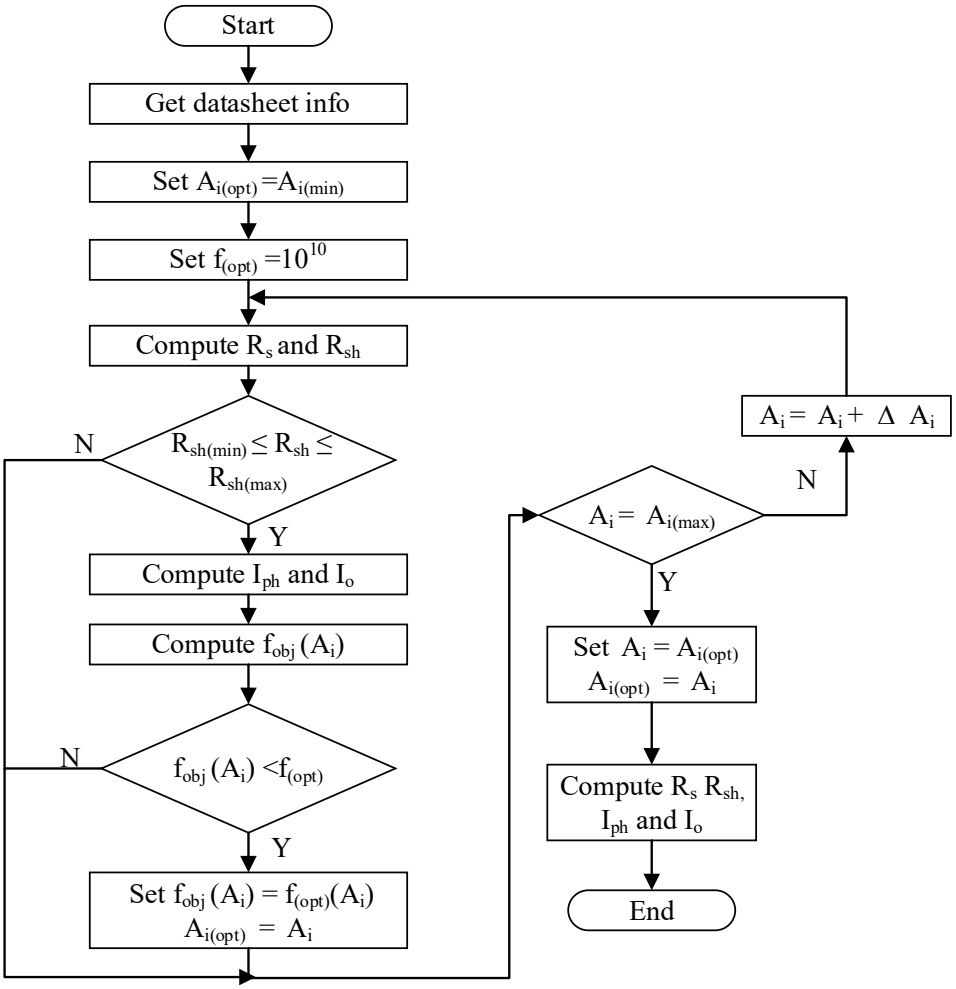

Figure 3.4 The process of estimating the PV module parameters at STC

Calculating R_s involves solving the Lambert W function, which is a complex process. Some advanced software like MATLAB has an inbuilt Lambert W function, but a simple search algorithm can be developed to solve for y in $x = ye^y$ for a given x .

3.2.2 Irradiance and Temperature Dependence of Parameters

The short circuit current of the PV module is dependent on both the irradiance (*G)* and the cell temperature (*T),* and is typically modeled as in (3.27), where I_{sc_STC} is the short circuit current at standard test conditions defined by $\mathrm{G_{STC}}(= 1000\frac{W}{m2})$ and $\mathrm{T_{STC}}(= 25℃)$ [3].

$$I_{sc}(G,T) = I_{sc_{STC}}\frac{G}{G_{STC}}[1 + \delta_{IscT}(T - T_{STC})] \tag{3.27}$$

The temperature coefficient of short circuit current (δ_{IscT}) is available in data sheets. The value of δ_{IscT} is typically given as a percentage variation of I_{sc_STC} per degree centigrade (%/^{o}C), and it is a positive value.

The V_{oc} of the module is also dependent on both the *G* and *T*. The V_{oc} varies linearly with *T*, but the variation of V_{oc} with *G* is nonlinear. However, the variation with *G* can be considered approximately linear with the change is $\ln(G)$ and the voltage can be modeled as given in (3.28), where V_{oc_STC} is the open circuit voltage at the standard test conditions [70]. The temperature coefficient of open circuit voltage (δ_{VocT}) is typically given as a percentage variation of V_{oc_STC} per degree centigrade (%/^{o}C) and is available in data sheets. The value of δ_{VocT} is negative as V_{oc} drops with the increase of cell temperature. The value of irradiance coefficient of open circuit voltage (δ_{VocG}) is not available in typical datasheets. But it can be evaluated using the open circuit voltage at the NOCT which is

usually given in the datasheets using (3.29[3] . NOCT (T_{NO}) is the cell temperature when the irradiance (G_{NO}) is 800 W/m^2, ambient temperature is 20 ºC, and the wind speed is 1 m/s [71], [72], [73], [74], [75].

$$V_{oc}(G,T) = V_{oc\_STC}\left[1 + \delta_{VocG}\left(ln\,(G) - ln\,(G_{STC})\right)\right]\left[1 + \delta_{VocT}(T - T_{STC})\right] \tag{3.28}$$

$$\delta_{VocG} = \frac{\dfrac{V_{oc}(G_{NO}, T_{NO})}{V_{oc\_STC}[1 + \delta_{VocT}(T_{NO} - T_{STC})]} - 1}{ln\,(G_{NO}) - ln\,(G_{STC})} \tag{3.29}$$

The short-circuit current can be restated as in (3.30**)**:

$$I_{sc}(G,T) = I_{sc_{STC}}\frac{G}{G_{STC}}\left[1 + \delta_{IscT}(T - T_{STC})\right] \tag{3.30}$$

Although the parameters R_s and A_i are also slightly affected by the temperature, they can be assumed to remain constant without significant error for the normal range of operating temperatures [1]. The dependence of I_{ph}, and I_o on G and T can be modeled using $V_T(T)$, $I_{sc}(G,T)$, and $V_{oc}(G,T)$ as given in (3.31) and (3.32).

$$I_{ph}(G,T) = I_{sc}(G,T)\left(1 + \frac{R_s}{R_{sh}}\right) \tag{3.31}$$

$$I_o(G,T) = \frac{I_{sc}(G,T)(R_s + R_{sh}) - V_{oc}(G,T)}{R_{sh}e^{\left(\frac{V_{oc}(G,T)}{A_i V_T(T)}\right)}} \tag{3.32}$$

Given the temperature and irradiance conditions for a specific PV module, it is possible to calculate the I-V and P-V curves using (3.27) – (3.31).

3.2.3 Validation of the Method Using Manufacturer's Data Sheets

The proposed parameter estimation methodology was implemented in MATLAB to verify the accuracy of the derived parameters for PV modules. The methodology was tested on several PV modules for which manufacturer datasheets provided I-V curves and other necessary data points.

To evaluate the accuracy of the estimated parameters against the manufacturer's datasheet values, two key error metrics were used:

1. **Root Mean Square Deviation (RMSD):** The RMSD quantifies the absolute difference between the model-predicted current ($I_{k,model}$) and the actual datasheet current ($I_{k,data}$) over N data points. It is defined as:

$$RMSD = \sqrt{\frac{\sum_{k=1}^{N}\left(I_{k,data} - I_{k,model}\right)^2}{N}} \tag{3.33}$$

2. **Normalized Root Mean Square Deviation (NRMSD):** The NRMSD normalizes the RMSD by dividing it by the short-circuit current (Isc) of the module. This allows for a scale-independent comparison between different PV modules

$$NRMSD = \frac{RMSD}{Isc} \times 100 \tag{3.34}$$

The proposed method was applied to several PV modules, utilizing the datasheet-provided values for I_{sc}, V_{oc}, V_{mpp}, and I_{mpp}. The key equations were implemented in MATLAB, and the estimated parameters (R_s,R_{sh},I_{ph},I_o,A_i) were validated by comparing the predicted I-V curves to those provided in the manufacturer datasheets as shown in Table 3.1.

Table 3.1 : Manufacturer's Datasheet Values for Tested Modules

Parameters (STC)	**SOLAR MODULES.**				
	Canadian solar CS1U-405MS	*Jinko Solar JKM405M-54HL4*	*Suntech STP585S-C72/Nsh*	*Blue Sun BSM535M10 -72HPH*	*Deep Blue JAM78s30-600/GR*
Maximum power (P_{mpp})	405 W	405W	585 W	535W	600W
Voltage at Pmax (V_{mpp})	44.3 V	30.52V	42.79 V	41.47V	45.3V
Current at Pmax (I_{mpp})	9.16 A	13.27A	13.67 A	12.90 A	13.25A
Open-circuit voltage (V_{oc})	53.5 V	37.06V	51.55 V	49.45 V	53.5 V
Short-circuit current (I_{sc})	9.65 A	13.85A	14.40 A	13.79A	14.03A
Number of Cells in Series (N_{sm})	81	54	72	72	78

The estimated parameters of the tested solar modules are presented in Table 3.2. The results demonstrate realistic electrical characteristics for all modules, validating the effectiveness of the proposed parameter estimation method. Notably, the R_{sh} were consistently of the order of 1000 compared to the R_s, reflecting realistic electrical characteristics. Relaxing the range of A_i during the optimization process yielded optimum values for A_i within the range of [0.5–2.0], further improving the accuracy of the extracted parameters and ensuring realistic values for all other parameters.

Table 3.2 : Parameter Identification

Parameters (STC)	SOLAR MODULES.				
	CS1U-405MS	**JKM405M-54HL4**	**STP585S-C72/Nsh**	**BSM535M10 -72HPH**	**JAM78s30-600/GR**
Series Resistancce R_s (Ω)	0.2808	0.2035	0.1717	0.145	0.0465
Shunt Resistance R_{sh} (Ω)	15491	6.885.1	8657.3	14608	15681
Diode Ideality Factor (Ai)	1.2000	0.8700	1.1600	1.5350	1.3080
Photo Current at STC I_{ph} (A)	9.6502	13.8504	14.4003	13.7900	14.030
Irradiation coefficient of V_{oc} (%)	3.53	2.70	4.17	4.03	2.47

Model performances were evaluated by comparing the I-V curves from the data sheets with the model's output. The datasheet-provided I-V curves were extracted using an online graph extractor [38], allowing for direct comparison with the model-generated curves. The accuracy of the model was assessed by calculating the difference in the PV current between the model predictions and the datasheet values using the NRMSD as the metric.

3.2.3.1 Effect of irradiance

The performance of the proposed parameter estimation method was evaluated under varying irradiance levels for PV modules from different manufacturers, while maintaining a constant temperature of 25°C. Figure 3.5 illustrates the comparison between the I-V characteristics predicted by the model and the corresponding datasheet values at different irradiance levels.

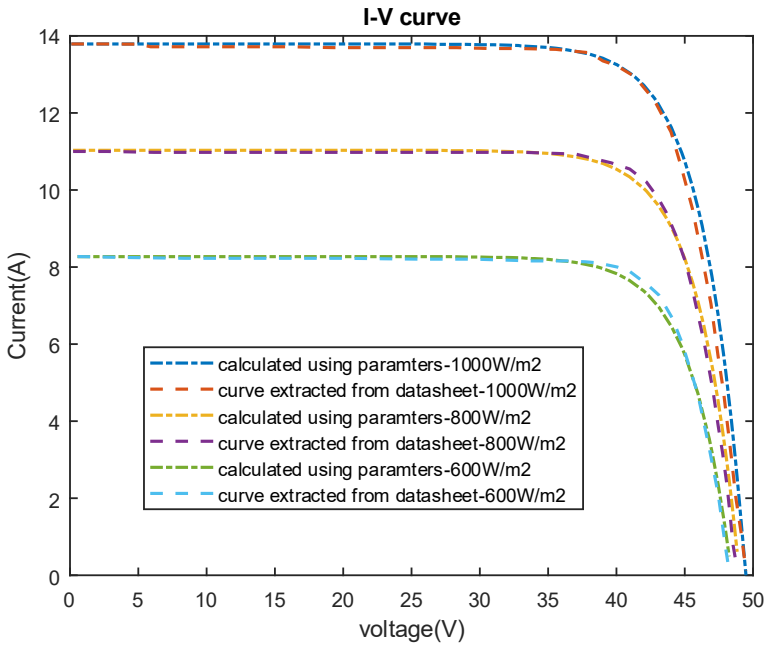

Figure 3.5 : I-V Comparison between the proposed method and the manufacturer data of the "Blue sun" panel at different irradiances

The accuracy of the model was further validated using the NRMSD as a metric. Table 3.3 presents the NRMSD values for different modules at various irradiance levels. The results show that the NRMSD values lie consistently within the range of 1%–4%, indicating an excellent fit between the predicted and actual values.

Table 3.3 : NRSMD values as a percentage for different PV modules at different irradiation levels in 25°C

PV modules.	**Irradiances**		
	1000(W/m^2)	800(W/m^2)	600(W/m^2)
Canadian Solar	4.05	2.69	1.95
Jinko solar	1.62	1.27	1.55
Suntech	1.52	1.16	1.22
Blue sun	1.47	1.68	1.05
Deep Blue	2.47	1.77	1.78

3.2.3.2 Effect of temperature

The impact of temperature on the performance of PV modules was evaluated by comparing the I-V characteristics generated by the proposed method with the manufacturer's datasheet I-V curves. The comparisons, shown in Figure 3.6, were conducted at a constant irradiance of 1000 W/m² across various temperature levels.

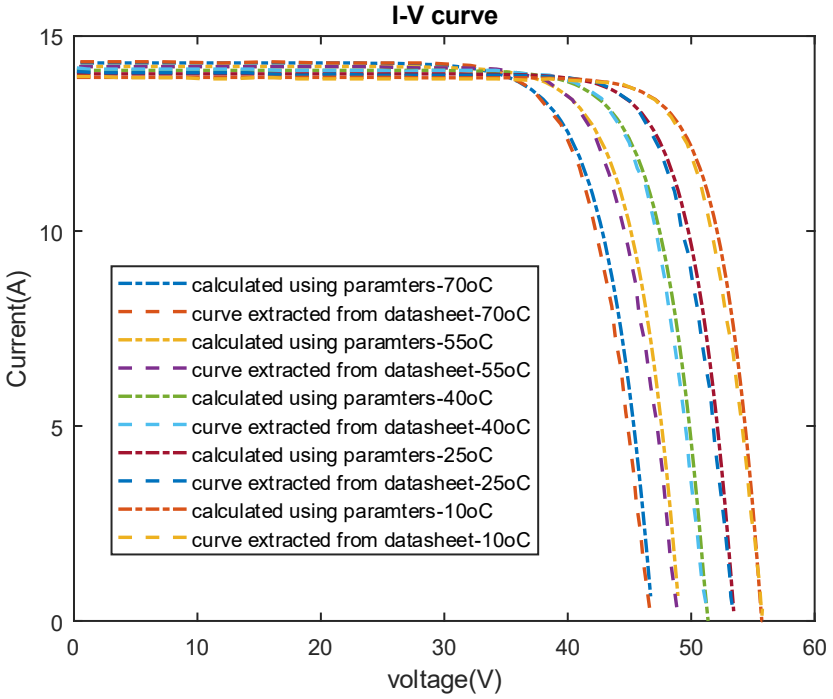

Figure 3.6 Comparison between the proposed method and the manufacturer data of deep blue solar panel at different T values and G of 1000W/m^2

The I-V curves required for detailed comparisons are not always available in every manufacturer's datasheet. For modules where I-V curves were provided at different temperature levels under a constant irradiance (G=1000 W/m²), the model's accuracy was evaluated using the NRMSD metric.

Table 3.4 presents the NRMSD values for two solar modules under varying temperatures. The values consistently fall within the range of 1%–3%, indicating a strong agreement between the estimated and actual values, even as temperature levels vary.

Table 3.4 NRSMD values at different temperatures

Temperature (°C)	Blue sun PV module	Deep Blue PV module
10	1.89	1.78
25	2.47	1.83
40	1.64	2.54
55	2.99	2.65
70	2.65	2.99

While the temperature coefficient of power (K_p) is commonly provided in datasheets, it is not directly used in the proposed methodology. Instead, the calculated K_p values are compared with the datasheet-provided values to further validate the accuracy of the model. K_p quantifies the rate at which a PV module's P_{mpp} changes with temperature. It is expressed as the slope of the percentage variation of P_{mpp} with respect to T.

The calculation of K_p involves analyzing the P_{mpp} at different temperatures and plotting the "Percentage variation of P_{mpp} vs. T graph. Figure 3.7 and Figure 3.8, derived from Jinko Solar data, illustrate this calculation process. These graphs visually demonstrate the linear relationship between the percentage change in P_{mpp} and T, providing a clear method for determining K_p .

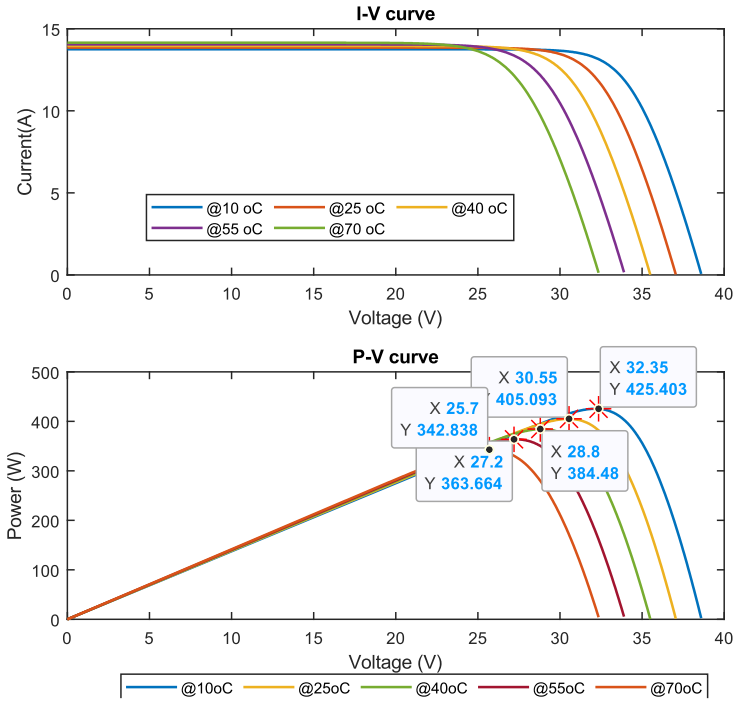

Figure 3.7 I-V, P-V curves for Jinko Solar panel for different temperatures

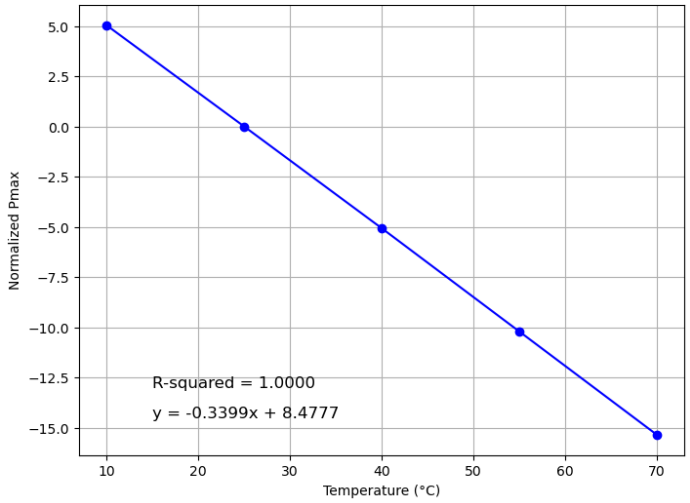

Figure 3.8 Percentage variation of Pmax vs Temperature

To validate the accuracy of the proposed model, the value of K_p is compared against manufacturer datasheet values, as shown in Table 3.5. The percentage difference is in the range of 1- 4%, for all PV modules. This reaffirms the proposed model's accuracy in estimating I-V characteristics for a given PV module.

Table 3.5 Comparison of Kp for different PV modules

PV module	Data sheet value (% / °C)	Calculated value. (% / °C)	Percentage Error (%)
Canadian Solar	-0.37	-0.35	4.13
Jinko solar	-0.35	-0.339	2.85
Suntech	-0.3	-0.304	1.43
Blue sun	-0.35	-0.346	1.02
Deep Blue	-0.35	-0.346	1.25

3.3 Bifacial PV Modules

3.3.1 Background

Bifacial PV technology, which captures solar energy from both the front and rear surfaces of solar modules, has emerged as a promising advancement in solar energy generation. As illustrated in Figure 3.9, these modules utilize rear-side irradiance in addition to direct sunlight on the front surface. This dual exposure enables bifacial modules to achieve higher energy yields compared to their monofacial counterparts. Consequently, they present an attractive solution for enhancing solar power efficiency.

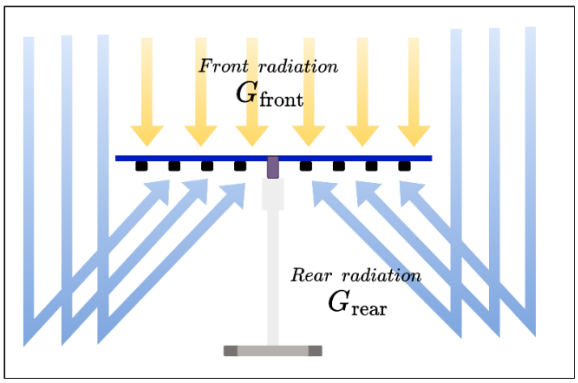

Figure 3.9 Bifacial PV module

3.3.2 Enhanced SDM Adaptation

While the SDM has been extensively validated and is widely used for simulating monofacial PV modules, its accuracy and applicability to bifacial PV modules remain less explored. Bifacial modules introduce unique characteristics, such as bifacial gain, bifaciality, and rear irradiance-driven power gain yield (BiFi), which require specific adaptations to traditional SDM modeling approaches. Furthermore, bifacial modules are often subjected to partial shading, a factor that can significantly impact energy output and is insufficiently addressed in existing models. Some of the bifacial PV module parameters are discussed in Section 3.3.2.1.

3.3.2.1 Bifacial PV Module Parameters

Bifacial Gain

Bifacial Gain, a crucial metric in bifacial PV modules, signifies the additional energy output compared to monofacial counterparts. It is shaped by diverse factors including albedo (reflectivity of the ground), solar radiation, module height, rear shading, and row pitch. Albedo, measuring reflected light, plays a substantial role in influencing energy generation on the rear side. Solar radiation directly affects energy yield on both sides of the module. Module height, shading, and row pitch are essential considerations to determine the amount of light reaching the rear side. Bifacial Gain can be mathematically expressed as [76], [77]:

$$Bifacial\ Gain = \frac{E_{bifi}}{E_{mono}} - 1 = \frac{E_{rear}}{E_{mono}} \tag{3.35}$$

Where:

- E_{mono} is the specific energy yield with front-side illumination under identical conditions.
- $E_{bifi,}$ *is* the specific energy yield of the bifacial module.
- E_{rear}, is the difference between E_{bifi} and E_{mono}, denoted as encapsulates the incremental energy gain from the rear side.

Bifaciality

Bifaciality characterizes the relative performance of a module's rear side compared to its front side. Measured under STC, it is expressed through three key ratios: $\varphi Pmax$ (rear-to-front side maximum power), φVOC (rear-to-front open-circuit voltage), and φISC (rear-to-front short-circuit current). Notably, the values of $\varphi Pmax$ vary depending on module technology, with n type - Passivated Emitter Rear Totally Diffused (PERT) modules ranging from 75% to 95%, p-type Passivated Emitter and Rear Cell (PERC) modules from 60% to 70%, and Heterojunction Technology (HJT) modules exceeding 90%. Bifaciality, an intrinsic module property, interacts with installation techniques and environmental factors to determine Bifacial Gain [25], [76]. Equation (3.36) defines bifaciality as the ratio of the rear-side maximum power output ($Pmpp_{rear}$) to the front-side maximum power output ($Pmpp_{front}$).

$$\varphi\text{Pmax} = \frac{Pmpp_{rear}}{Pmpp_{front}} \tag{3.36}$$

Rear-irradiance driven power gain yield (BiFi)

The rear irradiance-driven power gain yield (BiFi) quantifies the contribution of rear-side irradiance to the P_{mpp} of bifacial PV modules. It is determined by analyzing the module's

P_{mpp} under a fixed front irradiance (G_{front}=1000 W/ m^2) while varying the rear irradiance (G_{rear}). BiFi is calculated as the slope of the P_{mpp} vs. G_{rear} graph, adhering to the IEC 60904-1-2 standard, which provides two measurement methods: single-side illumination, where G_{rear} is calculated indirectly, and double-side illumination, where G_{rear} is directly measured [76]. This slope represents the additional energy yield contributed by the rear side of the module and serves as a critical metric for optimizing bifacial module performance. It is assumed that the module's performance can be interpolated between the STC and any level of rear irradiance, enabling accurate modeling and system design. Figure 3.10 illustrates the P_{mpp} vs. G_{rear} relationship, with the slope defining BiFi.

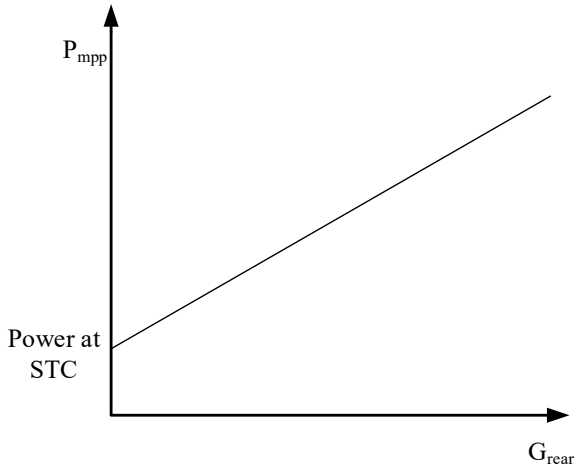

Figure 3.10 Power vs the rear irradiation (slope is used to calculate find BiFi)

Equivalent Irradiance (G_E)

Equivalent irradiance represents the combined effect of irradiance received on both the front and rear surfaces of a bifacial PV module as illustrated in Figure 3.11. This value is adjusted by the module's bifaciality, which reflects the relative performance of the rear

side. Equation (3.37) describes the total effective irradiance (G_E) as the sum of the G_{front} and the rear-side G_{rear}, scaled by the bifaciality factor.

$$G_E = G_{front} + \text{Bifaciality}. G_{rear} \tag{3.37}$$

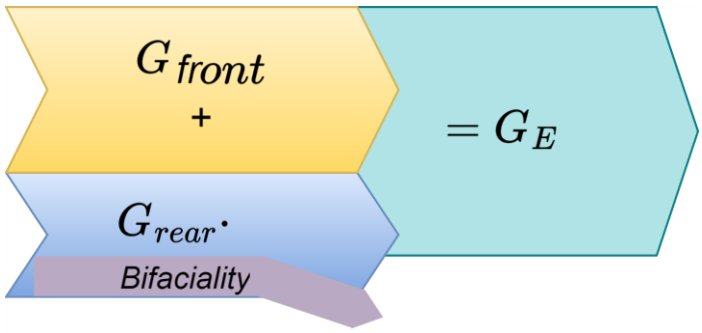

Figure 3.11 Equivalent irradiation

Bifacial Ratio

Bifacial ratio is the ratio between the G_{rear} and G_{front} as shown in (3.38).

$$\text{Bifacial ratio} = \frac{G_{rear}}{G_{front}} \tag{3.38}$$

From the equations describing the parameters of bifacial PV modules, the relationship between bifacial gain, bifacial ratio, and bifaciality can be expressed as:

$$Bifacial\ Gain = Bifacial\ ratio\ .\ Bifaciality \tag{3.39}$$

3.3.2.2 Bifacial PV Module Equivalent Circuit

The adaptation of the SDM to include separate photocurrent sources for the front and rear surfaces aligns with the single-side illumination method described in the IEC 60904-1-2 standard [25]. This approach effectively models bifacial modules by considering contributions from both irradiance sources. For bifacial PV modules, the model can be

adapted to include separate photocurrent sources for the front and back sides as in Figure 3.12 which depicts the equivalent circuit. The total photocurrent (I_{ph}) can be written as the summation of front ($I_{ph,f}$) and rear ($I_{ph,r}$) photoelectric current currents as (3.40).

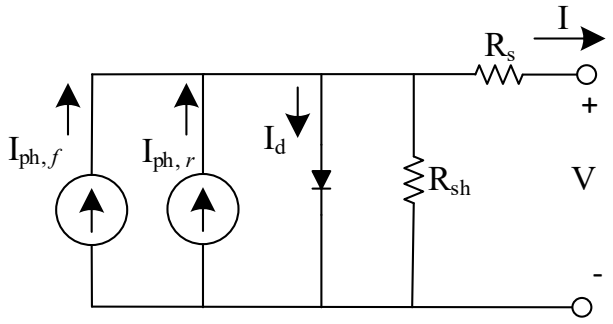

Figure 3.12 Bifacial PV module equivalent circuit

$$I_{ph} = I_{ph,f} + I_{ph,r} \tag{3.40}$$

Although there may be a minor mismatch between the I-V curves around the maximum power point when comparing the single-side and double-side illumination methods, this difference is typically negligible [78]. Additionally, research has shown that there is no significant difference in the temperature coefficient of short circuit current ($\delta_{I_{SCT}}$) of the front and rear sides of the module [79]. As a result, the SDM, with its inherent simplicity and adaptability, remains an accurate and practical tool for evaluating the performance of bifacial PV modules. By accommodating the contributions from both the front and rear surfaces, the same modeling approach used for monofacial modules can be effectively applied to bifacial modules with minimal modifications

3.3.2.3 Modeling Partial Shading

In PV systems, shading from surrounding facilities or objects can significantly impact module performance. Unlike unshaded cells that convert sunlight into electricity, shaded

cells in a module cease to generate power and instead begin to act as loads. This phenomenon leads to electrical consumption by the shaded cells, utilizing the energy produced by the remaining illuminated cells within the module. The resultant effect is a reduction in the overall electrical output of the module and the generation of heat losses. This heat can induce thermal stress and damage to the solar cells, manifesting as hot spots which accelerate the degradation of the module's performance and durability. To mitigate the adverse effects of partial shading, bypass diodes are integrated into PV modules. These diodes are designed to provide an alternative path for the current to flow around shaded cells, thus preventing them from consuming power and overheating. Typically, in a 72-cell PV module, one bypass diode is installed for every group of 24 cells as shown in Figure 3.13.

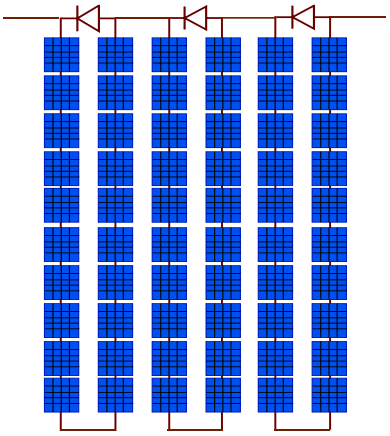

Figure 3.13 Physical configuration of a PV module

If there are N_s number of cells in a PV module and N_b number of bypass diodes, each group of cells, consisting of N_s/N_b, is connected in series and protected by a bypass diode, as illustrated in Figure 3.14.

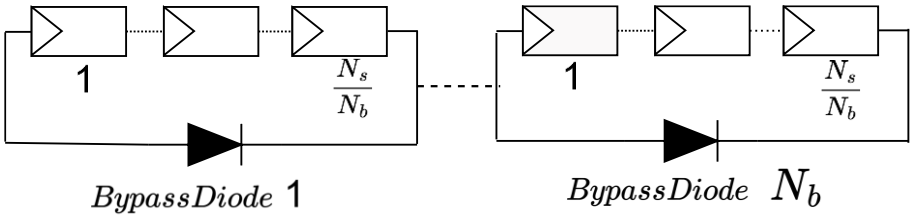

Figure 3.14 PV module configuration with bypass diodes for N_s/N_b, cell groups.

When shading occurs on one group, the bypass diode associated with that group becomes active, creating an alternative current path. This design isolates the shaded group, allowing the rest of the module to continue operating efficiently. This modular protection mechanism enhances the reliability and performance of PV modules under real-world conditions. Figure 3.15 depicts the electrical circuit configuration of each group of cells.

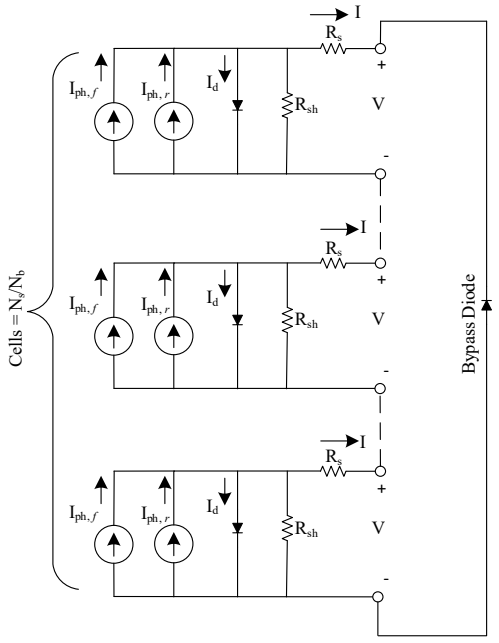

Figure 3.15 Electrical circuit of a single cell group with bypass diode.

When modeling the effects of partial shading on PV cells, it's essential to consider the details of each individual cell. Partial shading can cause significant variations in the performance of different cells within the same module, affecting the overall module output. The parameters of the SDM for a solar cell can be extracted using the same method used to extract the parameters of a solar module using manufacturers data. For a solar cell within a module, these parameters can be adjusted based on the number of cells in series (Ns) as follows:

$$V_{oc_{cell}} = \frac{V_{oc_{STC}}}{N_s} ; V_{mpp_{cell}} = \frac{V_{mpp_{STC}}}{N_s} \quad (3.41)$$

(Where, $V_{oc_{STC}}$, $V_{mpp_{STC}}$,$N_s$are from data sheets.)

These equations are used to determine the electrical characteristics of each cell in the context of the whole module. This is crucial when modeling the impact of partial shading because the shaded and unshaded cells will have different electrical outputs, which must be accurately represented in the model to predict the module's performance.

This detailed approach allows for more accurate predictions of PV system behavior under real-world conditions, which is especially important for systems that incorporate bifacial modules where partial shading can occur on either side of the module.

To accurately model this behavior, a series of equations and conditions are used to predict the cell's I-V characteristics. Isc_{cell} can be written as the summation of front (Isc_f) and rear (Isc_r) short circuit currents as in (3.42).

$$Isc_{cell} = Isc_f + Isc_r \quad (3.42)$$

Rear and front short circuit currents can be written as in (3.43) and (3.44) where, SR_f is shading ratio of front side of the cell, SR_r is shading ratio of rear side of the cell and Isc_{STC} is the short circuit current of the module at STC.

$$Isc_f = Isc_{STC}.\left(\frac{G_f}{G_{STC}}\right).\left(1 + \delta_{I_{SCT}}.(Tnom - T_{STC})\right).\left(1 - \frac{SR_f}{100}\right) \quad (3.43)$$

$$Isc_r = Isc_{STC}.\left(\frac{G_r}{G_{STC}}\right).\left(1 + \delta_{I_{SCT}}.(Tnom - T_{STC})\right).\left(1 - \frac{SR_r}{100}\right) \quad (3.44)$$

As in the SDM of a monofacial solar module, dark saturation current (Io_{cell}), photoelectric current (Iph_{cell}) of bifacial solar cell can be written as (3.45) and (3.46).

$$Io_{cell} = \frac{Isc_{cell}.(Rsh + Rs) - Voc}{Rsh.exp\left(\frac{Voc}{a.Vt}\right)} \quad (3.45)$$

$$Iph_{cell} = Isc_{cell}.\left(1 + \frac{Rs}{Rsh}\right) \quad (3.46)$$

In plotting the I-V curve of the bifacial module, voltage of all shaded and unshaded cells should be calculated to a particular current value. To find the voltage of a cell the following procedure can be followed.

For Individual Cells:

If $0 \leq I \leq Iph_{cell}$:

The voltage of the cell (V_{cell}) is found by solving the single diode equation:

$$0 = -I + Iph_{cell} - Io_{cell}.(exp(\frac{V_{cell}+I.Rs}{a.Vt}) - 1) - (\frac{V_{cell}+I.Rs}{Rsh}) \quad (3.47)$$

If $I > Iph_{cell}$

The voltage is determined by the linear equation:

$$V_{cell} = -(Rsh + Rs).I + Iph_{cell}.Rsh \quad (3.48)$$

For String of Cells:

To find the voltage of a particular string, photoelectric current of the string (Iph_{STRING}) should be found as follows. This is the minimum photocurrent from all cells in the string

$$Iph_{STRING} = \min\ (Iph_{cells}) \quad (3.49)$$

Voltage of the string (V_{STRING}) based on current (I):

If $0 \leq I \leq Iph_{STRING}$

$$V_{STRING} = \sum V_{cell} \quad (3.50)$$

If $\sum V_{cell} \geq Vd \ and \ I \geq Iph_{STRING}$ where Vd is diode forward voltage drop typically around -0.6V

$$V_{STRING} = \sum V_{cell} \quad (3.51)$$

If $\sum V_{cell} < Vd \ and \ I \geq Iph_{STRING}$

$$V_{STRING} = \text{Vd} \quad (3.52)$$

For the number of substrings in the module, voltage is calculated as above and voltage of the solar module at a particular current can be found by the summation of all voltages of the substrings.

The complete procedure for determining the I-V characteristic curve of a given bifacial module, along with shading information, is illustrated in the Figure 3.16.

.

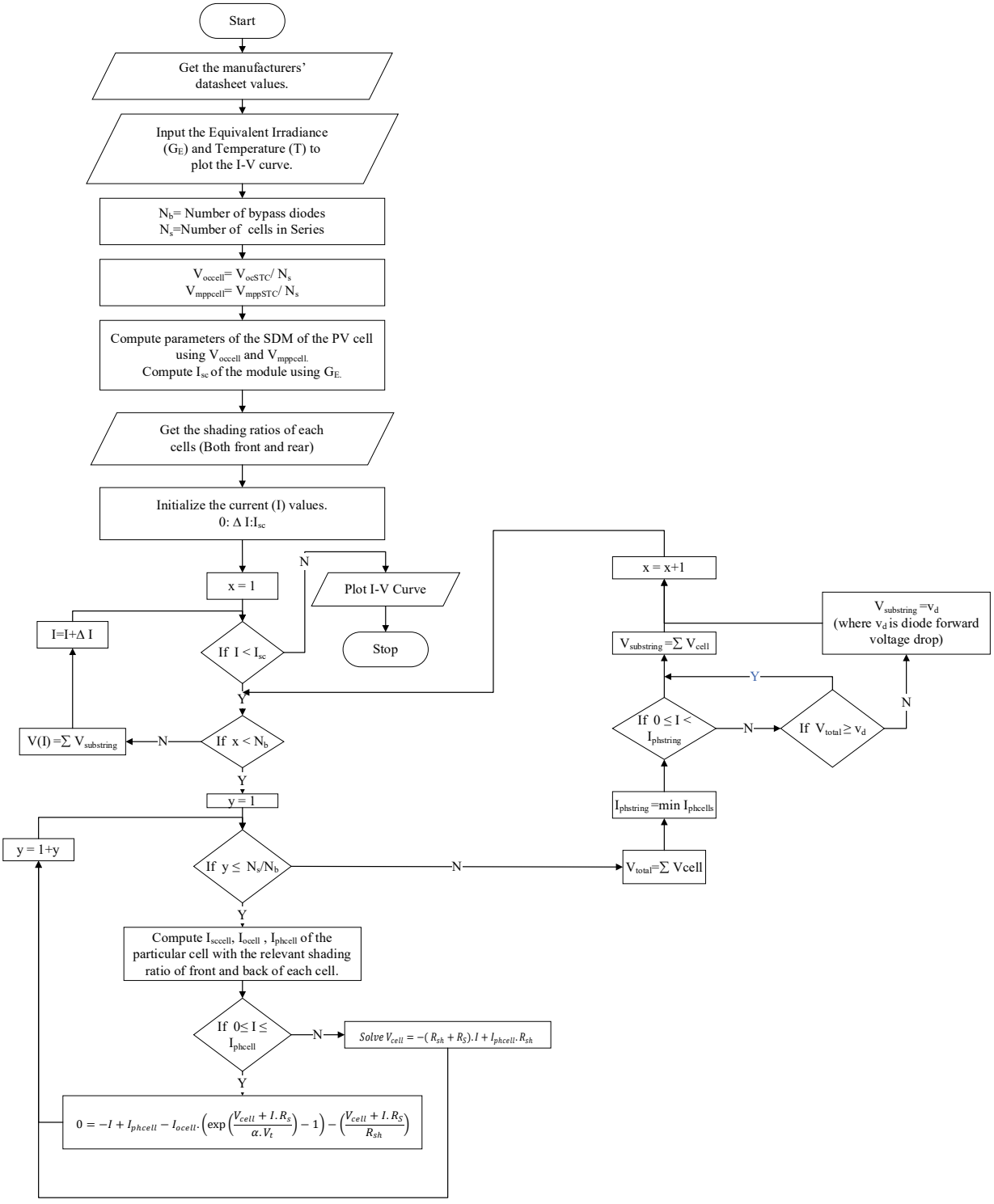

Figure 3.16 Procedure for determining the I-V characteristics

3.3.3 Validation of Bifacial PV Module Model with Manufacturer's Data

This section presents results of the validation of bifacial PV model with parameters estimated from the manufacturer-provided data. The SDM parameter estimation methodology applied to the mono-facial modules was applied to the bifacial modules. With the estimated model parameters, the key electrical characteristics, including P_{mpp}, V_{oc}, I_{sc}, I_{mpp}, and V_{mpp}, are re-evaluated at various bifacial gains and compared with the manufacturer specifications. The comparison results presented in Table 3.6 and Table 3.7 shows good agreement between computed and data sheet values for various bifacial gains. While a direct comparison of I-V curves was not feasible due to the lack of a controlled test setup, the differences between the estimated values and manufacturer data were minimal, with all errors consistently under 1%.

Table 3.6 Comparison of electric characteristics at different bifacial gains for Longi-545W module [80]

Bifacial Gain(%)		**5.0**	**10.0**	**15.0**	**20.0**	**25.0**
Pmax (W)	Data	572	600.00	627.00	654.00	681.00
	Estimated	572.39	600.67	627.84	655.01	682.19
	Error (%)	0.07	0.11	0.13	0.15	0.18
Voc (V)	Data	49.65	49.65	49.75	49.75	49.75
	Estimated	49.67	49.68	49.70	49.72	49.73
	Error (%)	0.04	0.07	0.10	0.07	0.04
Isc(A)	Data	14.61	15.31	16.00	16.70	17.39
	Estimated	14.61	15.32	16.01	16.70	17.39
	Error (%)	0.00	0.10	0.09	0.02	0.02
Impp (A)	Data	13.69	14.34	14.99	15.65	16.30
	Estimated	13.71	14.37	15.02	15.67	16.34
	Error (%)	0.15	0.21	0.20	0.13	0.25
Vmpp (V)	Data	41.80	41.80	41.90	41.90	41.90
	Estimated	41.75	41.80	41.80	41.80	41.75
	Error (%)	0.12	0.00	0.24	0.24	0.36

Table 3.7 Comparison of electric characteristics at different bifacial gains for LG-390N2T-A5 module[81]

Bifacial Gain(%)		**5**	**10**	**20**	**30**
Pmax (W)	Data	410	429.00	468.00	507.00
	Estimated	410.11	430.36	470.79	511.29
	Error (%)	0.03	0.32	0.60	0.85
Voc (V)	Data	49.20	49.20	49.30	49.30
	Estimated	49.26	49.31	49.41	49.51
	Error (%)	0.12	0.23	0.23	0.42
Isc(A)	Data	10.65	11.17	12.18	13.20
	Estimated	10.66	11.17	12.18	13.20
	Error (%)	0.07	0.04	0.00	0.04
Impp (A)	Data	9.90	10.36	11.28	12.22
	Estimated	9.93	10.37	11.29	12.35
	Error (%)	0.30	0.10	0.09	1.06
Vmpp (V)	Data	41.40	41.40	41.50	41.50
	Estimated	41.30	41.50	41.70	41.70
	Error (%)	0.24	0.24	0.48	0.48

3.3.4 Validation with Previously Published Experimental Results

In several research papers, I-V curves of bifacial PV modules have been presented without explicit references to manufacturer data. However, in the study in [82], the authors provided reference to the manufacturer data sheet and presented several I-V and P-V curves at various conditions [81]. Although the authors did not provide bifacial gain data for each case, they did include measured values for V_{oc} and I_{sc} for a particular condition. These values are used to reverse-calculate the temperature T and equivalent irradiance G_E , which represents the combined effect of irradiance received on both the front and rear surfaces, under various test conditions by solving (3.53) and (3.54).

$$I_{SCT}(G,T) = I_{sc_{STC}} \frac{G_E}{G_{STC}} \left[1 + \delta_{I_{SCT}}(T - T_{STC})\right] \tag{3.53}$$

$$V_{oc}(G,T) = V_{oc_{STC}}[1 + \delta_{VocG}(ln\,(G_E) - ln\,(G_{STC}))][1 + \delta_{VocT}(T - T_{STC})] \tag{3.54}$$

Three cases were taken to calculate values of G_E (total effective irradiance) and Temperatures as shown in Table 3.8.

Table 3.8 Back calculated G_E and Temperature for three cases found in [82]

Case	**I_{sc}(A)**	**V_{oc} (V)**	**Back calculated**	
			G_E Wm^{-2}	**Temperature (K)**
1	10.42	46.75	1020.76	317.22
2	10.63	48.59	1045.53	303.74
3	9.54	47.039	935.74	312.95

The reverse-calculated parameters were subsequently used to generate I-V curves for the bifacial module, which were directly compared to the experimentally measured curves as illustrated in Figure 3.17. The NRMSD values for these comparisons across three cases are presented in Table 3.9.

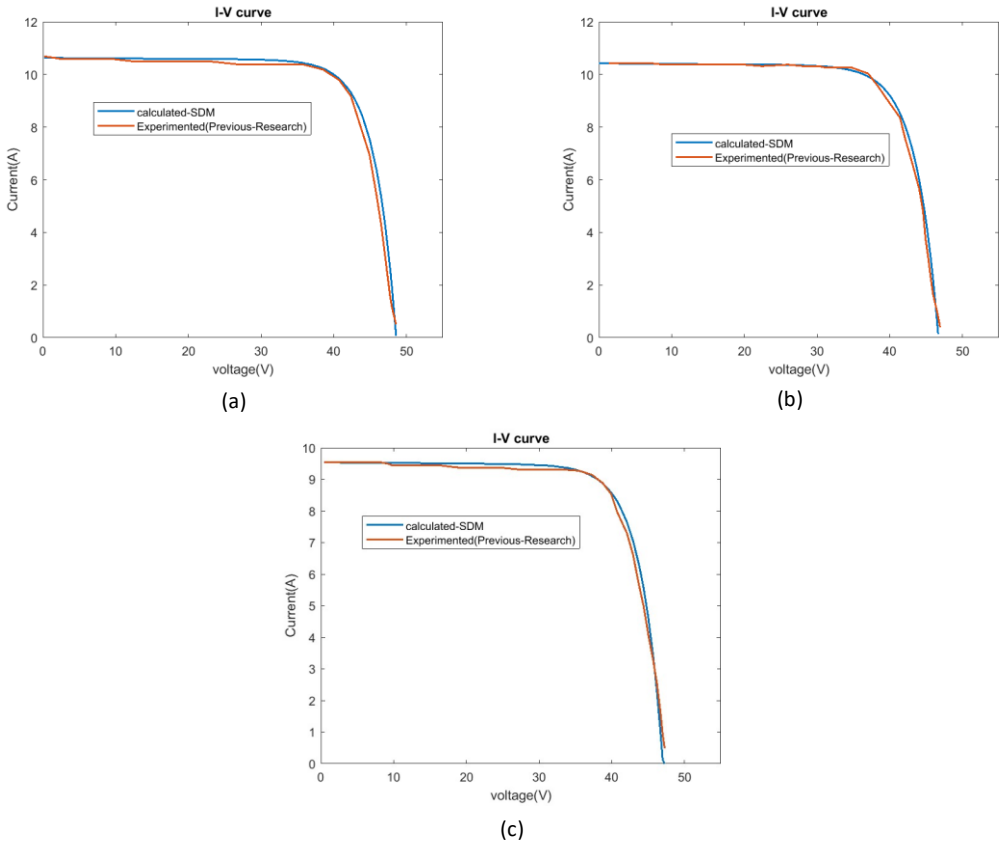

Figure 3.17 I-V curves for (a) Case 1 (b) Case 2 (c) Case3 in Table 3.8

Table 3.9 NRMSD values for three cases in Table 3.8

Case	1	2	3
NRMSD (%)	3.24	3.54	2.82

3.3.5 Validation of the Model for Partial Shading of Bifacial Modules

The study outlined in [83] offered valuable insights into the performance of bifacial PV modules. Researchers provided detailed information on factors such as rear-side shading, temperature fluctuations, and manufacturer data. Using this data, a model for partial shading of bifacial modules was validated. The study focused on bifacial PERC cells, operating under the assumption that their bifaciality falls within the range of 60% to 70%.

The experiments involved placing cardboard strips in various positions and orientations behind the bifacial module to simulate rear-side shading as shown in Figure 3.18.

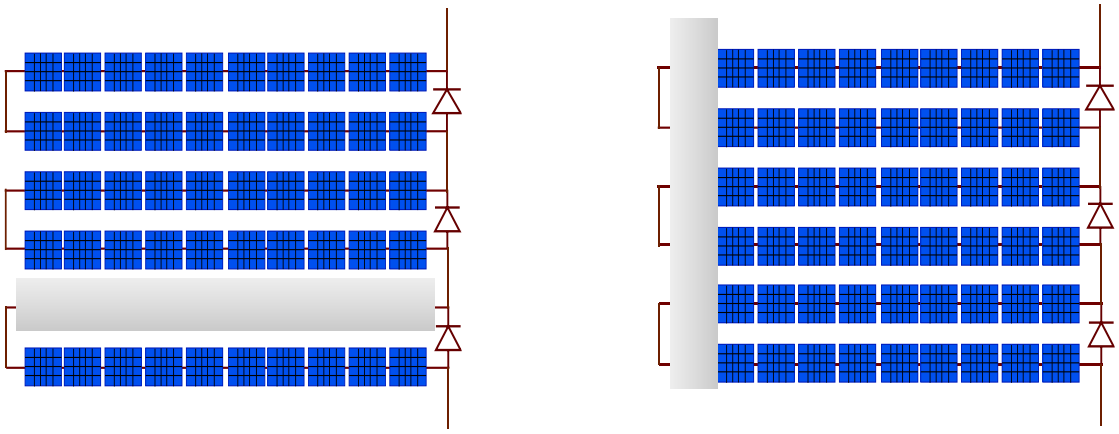

Figure 3.18 : Rear-surface shading on a bifacial PV module using cardboard strips [83]

First, using the manufacturer's data, the model parameters were estimated. Then the I-V curves under the shading conditions corresponding to experimental results given in [83] were generated using the model with estimated parameters. Figure 3.19 and Figure 3.20 show the comparison of I-V curves obtained with the proposed method with the experimental results found in [83]. NRMSD values of these two case are 3.1% and 3.3% respectively.

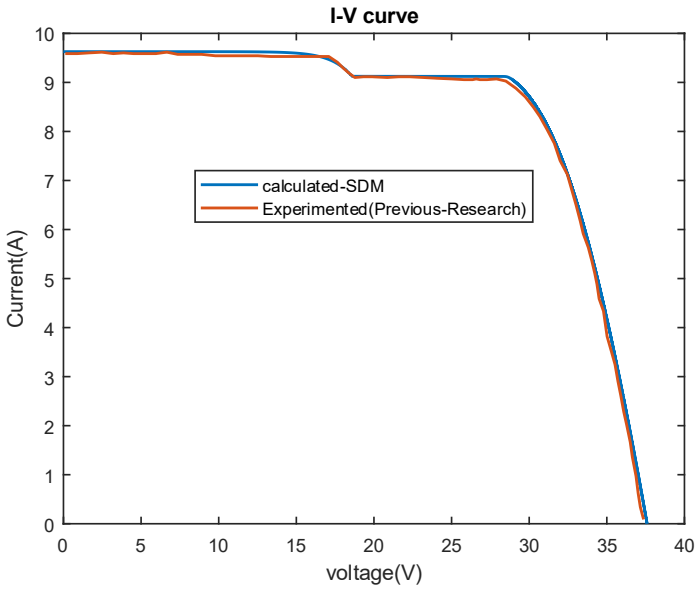

Figure 3.19 Comparison of I-V curves obtained using the proposed method with experimental results when an obstruction is placed along a single string as described in [83]

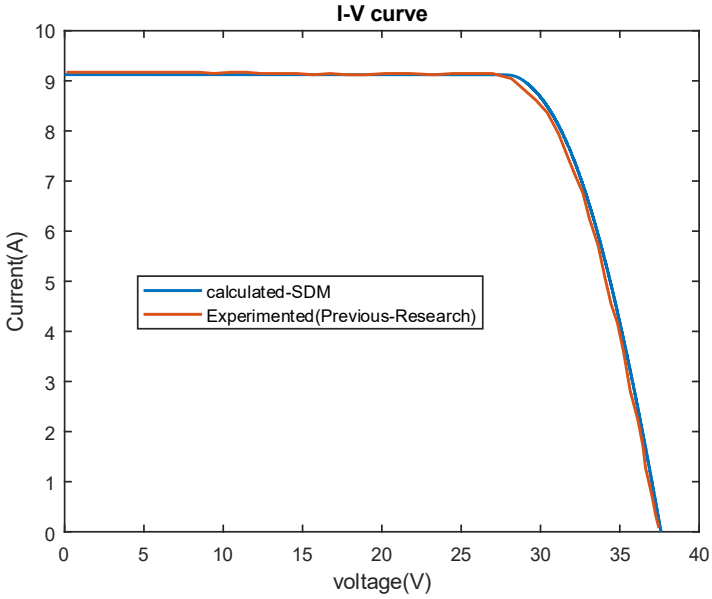

Figure 3.20 Comparison of I-V curves obtained using the proposed method with experimental results when an obstruction is placed across cell strings as described in [83]

3.4 Summary

This chapter presents a comprehensive analysis of the effectiveness of SDM for PV modules, structured into two distinct sections addressing monofacial and bifacial PV modules. Each section provides novel methodologies that provide robust solutions for parameter estimation and modeling of PV module performance, validated against manufacturer provided data and experimental data.

3.4.1 Monofacial PV Modules

A novel approach is proposed to estimate electrical parameters from manufacturer datasheets under STC. The methodology employs the Lambert-W function to solve a set of equations and extract the equivalent electrical circuit parameters based on manufacturer datasheet values under STC. A range of A_i values is tested, and the optimal A_i is identified using a multi-criteria objective function. Temperature and irradiance dependencies are derived using datasheet temperature coefficients and the irradiation coefficient of open-circuit voltage (from NOCT data). The proposed method is validated across five PV modules, demonstrating errors below 4% when compared to datasheet values. The method effectively predicts I-V characteristics and the temperature coefficient of maximum power, making it a reliable tool for simulation studies.

3.4.2 Bifacial PV Modules

The SDM proposed for monofacial modules is adapted to bifacial modules by integrating bifacial gain, bifaciality, and rear irradiance effects, aligning with IEC TS 60904-1-2 standards. The method is validated against manufacturer datasheets and experimental

results, achieving errors below 1% for key parameters (I_{sc}, V_{oc}, and P_{mpp}). A novel approach to model partial shading is proposed and validated using experimental data. This approach addresses gaps in bifacial modeling and supports enhanced energy capture and system optimization.

Together, these methodologies provide a robust framework for accurate simulation and design of PV systems, contributing significantly to both academic research and industry applications.

Chapter 4

Enhancements to DSOGI-PLL for Robust Grid Synchronization

This chapter proposes several modifications to the DSOGI-PLL to improve its phase and frequency tracking performance under transient conditions. The chapter presents an overview of the PLL algorithm, followed by a detailed discussion of the control structure of the SRF-PLL and its parameter tuning mechanisms. Subsequently, the DSOGI-PLL is introduced, along with its parameters. Then, the proposed modifications to the DSOGI-PLL are explained in detail. The chapter concludes with a basic validation of the PLL model, focusing on its dynamic performance using synthetic input signals under various transient scenarios.

4.1 Overview of the PLL Algorithm

The PLL is a nonlinear device (or mathematical process) that synchronizes the phase and frequency of an output signal to a reference signal. It operates based on the principle of feedback control, continuously adjusting the output phase to minimize the phase difference between the input and output signals. A typical PLL consists of three main components, which are the Phase Detector (PD), the Loop Filter (LF), and the Voltage Controlled Oscillator (VCO), as illustrated in Figure 4.1[42], [57] .

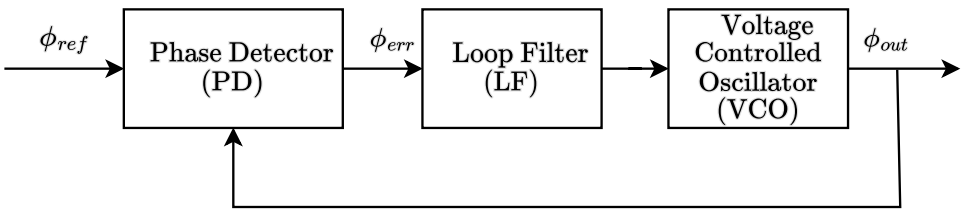

Figure 4.1Block diagram of PLL

- **Phase Detector (PD):** The PD compares the input signal ϕ_{ref} and the output signal $\phi_{out}$of the PLL. It generates a phase error signal ϕ_{err} proportional to the phase difference .
- **Loop Filter (LF):** The LF is responsible for filtering out high-frequency components (ac components) present in the phase error signalϕ_{err}. By doing so, it produces a corresponding dc control signal, which is then fed into the VCO. The LF may also incorporate a Proportional-Integral (PI) controller to reduce steady-state phase angle errors, ensuring precise phase tracking of the input voltage
- **Voltage Controlled Oscillator (VCO):** Adjusts the output frequency and phase based on the control signal from the loop filter

The main distinction among different types of PLLs lies in the implementation of the PD block. Variations in the PD design influence the overall system's performance and its ability to handle specific application requirements [57].

4.2 SRF-PLL

4.2.1 Overview of SRF-PLL

The SRF-PLL is a widely used control system designed to achieve phase and frequency synchronization of input signals, particularly in three-phase electrical systems. Figure 4.2 shows the basic structure of the SRF-PLL.

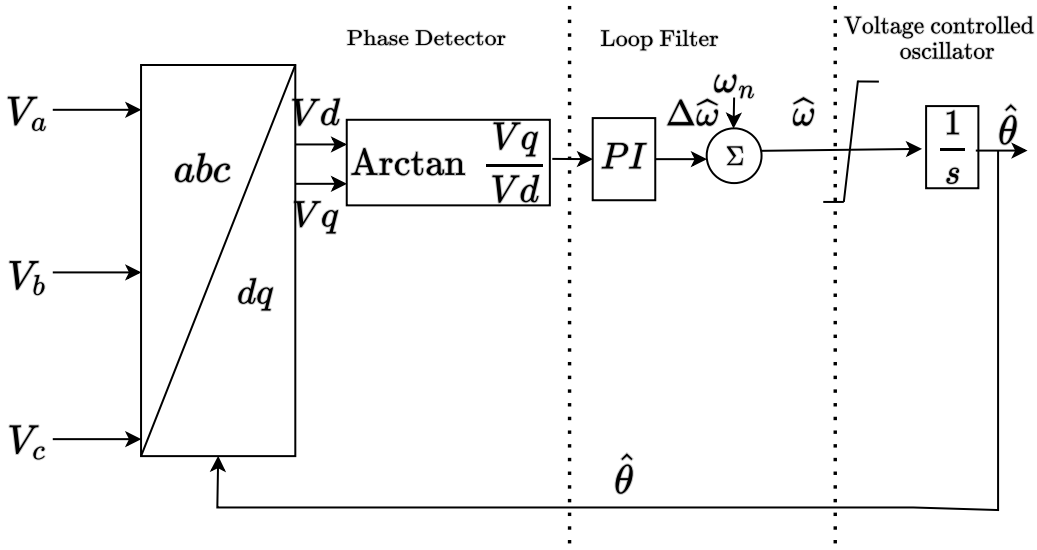

Figure 4.2 SRF-PLL

Here :

- $\hat{\theta}$ is the estimated phase angle.
- $\hat{\omega}$ is the estimated frequency.
- ω_n is the nominal frequency.

In this PLL, the transformation of the three-phase input voltages to the d-q synchronous reference frame is achieved through a combination of Clark and Park transformations.

Through the application of a feedback loop, the angular position of the d-q reference frame is regulated.

In the SRF-PLL, the proportional–integral (PI) controller plays a central role in regulating the estimated angular frequency and phase of the system. After the three-phase voltages are transformed into the synchronous d–q reference frame, the arctangent of vq/vd is used as the phase error signal. Under ideal synchronization conditions, this is driven to zero when the estimated phase angle $\hat{\theta}$ is aligned with the actual grid voltage vector.

The PI controller processes this error and generates a frequency correction term that adjusts the estimated frequency $\hat{\omega}$. The proportional term provides a fast dynamic response to phase and frequency deviations, while the integral term eliminates steady-state phase error by accumulating the error over time. The output of the PI controller is added to the nominal frequency $\omega_n$to form the estimated frequency $\hat{\omega}$, which is then integrated to obtain the estimated phase angle $\hat{\theta}$. Through this feedback mechanism, the PI controller forces the synchronous reference frame to lock onto the grid voltage, achieving stable phase and frequency synchronization.

Most of the SRF-PLLs used in control systems directly feed vq to the PI controller. However, this direct approach introduces nonlinearity to the PLL, potentially resulting in slower responses and system instability under specific conditions. Furthermore, the magnitude of the voltage contributes to the PLL bandwidth, leading to dynamic changes in bandwidth as the voltage magnitude varies. Taking arctangent of vq/vd can make the PLL linear and the PLL can have a constant BW irrespective of the magnitude of the voltage [84].

4.2.2 Small Signal Model of SRF-PLL

The three-phase input voltages V_{abc} of the PLL are assumed to be unbalanced and harmonically distorted, as expressed in (4.1).

$$
\begin{aligned}
Va(t) &= \sum_{1}^{\infty}[Vh^{+}\cos(h\omega t + \varphi h^{+}) + Vh^{-}\cos(h\omega t + \varphi h^{-})] \\
Vb(t) &= \sum_{1}^{\infty}[Vh^{+}\cos\left(h\omega t + \varphi h^{+} - \frac{2\pi}{3}\right) + Vh^{-}\cos\left(h\omega t + \varphi h^{-} + \frac{2\pi}{3}\right)] \\
Vc(t) &= \sum_{1}^{\infty}[Vh^{+}\cos\left(h\omega t + \varphi h^{+} + \frac{2\pi}{3}\right) + Vh^{-}\cos\left(h\omega t + \varphi h^{-} - \frac{2\pi}{3}\right)]
\end{aligned}
\tag{4.1}
$$

Where;

- h: Harmonic order (1 represents the fundamental frequency, while h>1 represents higher-order harmonics).
- ω: Angular frequency of the fundamental component.
- $Vh^{+}$and φh^{+}:Amplitude and phase angle of the positive-sequence component for the hth harmonic.
- $Vh^{-}$and φh^{-}: Amplitude and phase angle of the negative-sequence component for the hth harmonic.

The Park transformation can be seen as a composite transformation, where the Clarke transformation is followed by axes rotation as illustrated in Figure 4.3 [85].

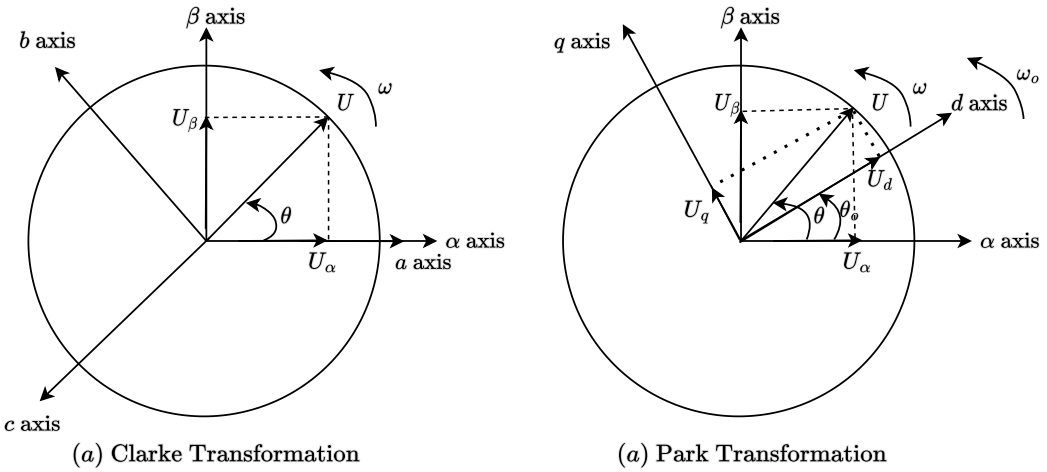

Figure 4.3 abc-αβ- dq transformation

Applying abc-αβ-dq Transformation to (4.1 will give *Vd, Vq* parameters as expressed in (4.2).

$$\begin{bmatrix} Vd \\ Vq \\ Vo \end{bmatrix} = \begin{bmatrix} cos\hat{\theta} & sin\hat{\theta} & 0 \\ -sin\hat{\theta} & cos\,\hat{\theta} & 0 \\ 0 & 0 & 1 \end{bmatrix} \frac{2}{3} \begin{bmatrix} 1 & -\frac{1}{2} & -\frac{1}{2} \\ 0 & \frac{\sqrt{3}}{2} & -\frac{\sqrt{3}}{2} \\ \frac{1}{\sqrt{2}} & \frac{1}{\sqrt{2}} & \frac{1}{\sqrt{2}} \end{bmatrix} \begin{bmatrix} Va \\ Vb \\ Vc \end{bmatrix} \text{ where } \hat{\theta}=\hat{\omega}t+\widehat{\varphi 1^+} \tag{4.2}$$

After simplifying the above equation, d-q components for positive and negative sequences can be derived as in (4.3):

$$\begin{bmatrix} Vd^+ \\ Vq^+ \end{bmatrix} = \begin{bmatrix} \sum_1^\infty [Vdh^+] \\ \sum_1^\infty [Vqh^+] \end{bmatrix} = \begin{bmatrix} \sum_1^\infty \left[Vh^+ \cos\left((h\omega - \hat{\omega})t + \varphi h^+ - \widehat{\varphi 1^+} \right) \right] \\ \sum_1^\infty \left[Vh^+ \sin\left((h\omega - \hat{\omega})t + \varphi h^+ - \widehat{\varphi 1^+} \right) \right] \end{bmatrix}; \tag{4.3}$$

$$\begin{bmatrix} Vd^- \\ Vq^- \end{bmatrix} = \begin{bmatrix} \sum_1^\infty [Vdh^-] \\ \sum_1^\infty [Vqh^-] \end{bmatrix} = \begin{bmatrix} \sum_1^\infty \left[Vh^- \cos\left((h\omega + \hat{\omega})t + \varphi h^- + \widehat{\varphi 1^+} \right) \right] \\ -\sum_1^\infty \left[Vh^- \sin\left((h\omega + \hat{\omega})t + \varphi h^- + \widehat{\varphi 1^+} \right) \right] \end{bmatrix}$$

Under a quasi-locked condition (i.e., ω = $\hat{\omega}$, and $\varphi 1^+ \approx \widehat{\varphi 1^+}$), the PLL achieves alignment such that $\theta = \hat{\theta}$ resulting in a zero-phase error. This indicates that U and U_d are in phase

and U_q become zero. As illustrated in Figure 4.3, when $U_q > 0$, U leads U_d, when $U_q < 0$, U lags U_d therefore, the phase error can be detected by using abc−αβ−dq transformation.

$$\begin{bmatrix} Vd \\ Vq \end{bmatrix} \approx \begin{bmatrix} \overline{Vd} \\ \overline{Vq} \end{bmatrix} + \begin{bmatrix} \widetilde{Vd} \\ \widetilde{Vq} \end{bmatrix} = \begin{bmatrix} Vh^{+}\cos\left(\varphi 1^{+} - \widehat{\varphi 1^{+}}\right) \\ Vh^{+}\sin\left(\varphi 1^{+} - \widehat{\varphi 1^{+}}\right) \end{bmatrix} + \begin{bmatrix} \sum_{2}^{\infty}[Vdh^{+}] \\ \sum_{2}^{\infty}[Vqh^{+}] \end{bmatrix} + \begin{bmatrix} \sum_{1}^{\infty}[Vdh^{-}] \\ \sum_{1}^{\infty}[Vqh^{-}] \end{bmatrix} ; \quad (4.4)$$

Where, $\overline{Vd}$ and $\overline{Vq}$ are dc terms and $\widetilde{Vd}$ and $\widetilde{Vq}$ are disturbance terms.

According to (4.3) and (4.4) fundamental negative-sequence component along with the harmonic components of the input voltage, appear as a disturbance input to the PLL linearized. Figure 4.4 shows the small signal model of the SRF-PLL. For the stability analysis of the PLL the disturbance terms can be neglected. This allows to take the error of the angle ($\varphi 1^{+} - \widehat{\varphi 1^{+}}$) by taking, $\tan^{-1}\frac{Vq}{Vd}$.

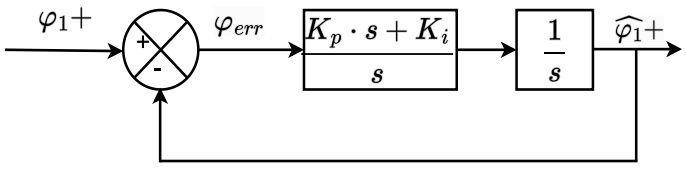

Figure 4.4 Small signal model of SRF- PLL

When designing the PLL, selecting appropriate proportional (K_p) and integral (K_i) gains is critical for ensuring stability and optimal performance. A stable system requires positive gain and phase margins, with a commonly recommended phase margin above 45°, as illustrated in Figure 4.5 [86].

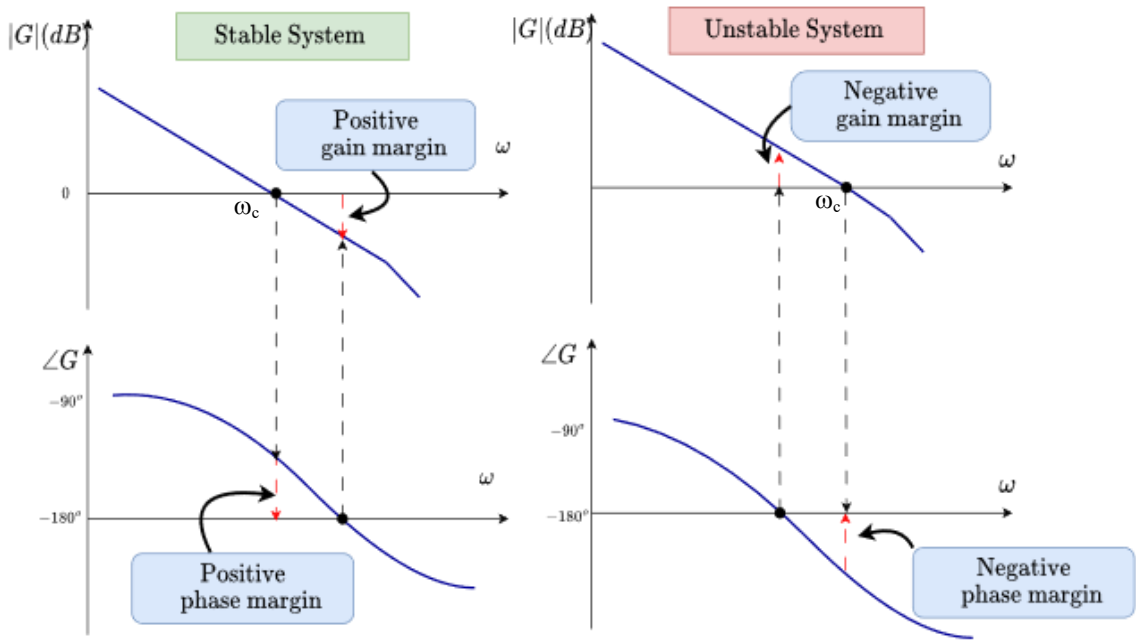

Figure 4.5 Stability criterions

Moreover, transient response of the system depends on the cross over frequency (ω_c) and achieving a faster transient response is often associated with a higher ω_c. Disturbance rejection capability is vital for a control system to attenuate external disturbances, ensuring stability and performance despite external influences. So, there is always trade off when choosing the ω_c. For SRF-PLL, ω_c is typically chosen as 0.2 times the nominal frequency (ω_n) , achieving approximately -20 dB attenuation at $2\omega_n$, which is crucial for managing the second-order harmonics present in the disturbance terms. Additionally, a damping ratio (ζ) closes to 0.707 is preferred for minimizing overshoot, reducing settling time, and mitigating oscillations. Achieving the right balance in these design parameters is crucial for ensuring stable and optimal performance of the PLL.

The open loop and closed loop transfer functions of the SRF-PLL are given in (4.5) and (4.6).

$$G_{olSRF} = \frac{K_p s + K_i}{s^2} \tag{4.5}$$

$$G_{clSRF} = \frac{K_p s + K_i}{s^2 + K_p s + K_i} \tag{4.6}$$

From (4.6) , the characteristic equation of the system can be obtain as $s^2 + K_p s + K_i$=0, which can be compared to the standard form of the second order equation $s^2 + 2\xi\omega_{nat} s + {\omega_{nat}}^2 = 0$, where ω_{nat} is the natural frequency of the system and ξ is the damping ratio of the system. In order to achieve the previously mentioned desirable crossover frequency and damping ratio values, the required K_p and K_i parameters can be calculated as follows:

- ω_c of the system should be selected less than 0.2 times the nominal frequency (ω_n) *s*uch that it will attenuate the second order disturnabnces by -20dB. For a 60 Hz system, where ω_n=377 rads^{-1}, ω_c can be selected as 75.39 rads^{-1}.

$$K_p = 2*\xi * \omega_{nat} \; ; \; K_i = {\omega_{nat}}^2 \tag{4.7}$$

At ω_c , the magnitude condition $|G_{olSRF}| = 1$ leads to :

$$\frac{\sqrt{\omega_c^2 . K_p^2 + K_i^2}}{\omega_c^2} = 1 \tag{4.8}$$

Substituting $\xi = 0.707$ and ω_c= 75.39 rads^{-1} on (4.7) and (4.8). K_p and K_i can be calculated and the phase margin also can be determined as follows.

$$K_p = \quad 68 \; ; \; K_i = 2330 \; ; \; PM = \tan^{-1}\frac{\omega c}{K_i/K_p} = 65^o \tag{4.9}$$

Figure 4.6 shows the Bode plot of SRF-PLL considering all these design criteria.

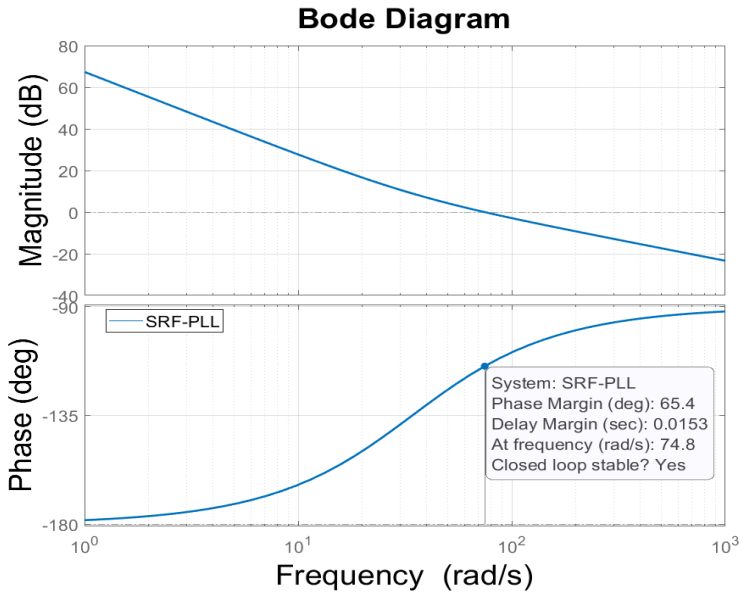

Figure 4.6 Bode plot of SRF-PLL

While the small-signal model of the SRF-PLL considers unbalanced and harmonically distorted input voltages, the stability analysis and controller design typically assume a quasi-locked condition where the input is balanced and predominantly sinusoidal. Under such assumptions, disturbance terms (e.g., harmonics and negative-sequence components) are neglected to simplify the analysis. However, in practical scenarios, the presence of unbalanced conditions, DC offsets, or harmonic distortions can introduce significant errors in the estimated phase and frequency, thereby degrading PLL performance. These limitations highlight the need for more robust PLL architectures capable of maintaining accuracy under non-ideal grid conditions.

4.3 Advancements on PLLs

To enhance the performance of the control system and address specific challenges, several advanced techniques can be employed. Many PLLs have been introduced in literature to overcome these challenges and out of them DSOGI-PLL takes a significant place due to its advantages over the other PLLS[19], [57]. The DSOGI-PLL is specifically designed to track the phase of the positive sequence voltage, offering noise immunity and enhanced harmonic rejection. These features make it particularly well-suited for operation under non-ideal grid conditions. The next section will discuss the DSOGI-PLL and perform its stability analysis.

4.3.1 DSOGI-PLL

4.3.1.1 Overview of DSOGI-PLL

The DSOGI-PLL is a sophisticated phase-locked loop with three main components:

1. **Second-Order Generalized Integrator (SOGI):** Two SOGI blocks are employed in the pre-filtering stage to process v_α and v_β signals.
2. **Positive Sequence Calculator (PSC):** Extracts the FFPS components.
3. **SRF-PLL:** A conventional PLL used to determine the grid frequency and phase.

Structures of the DSOGI-PLL and SOGI block are shown in Figure 4.7 and Figure 4.8 respectively. In the configuration shown in Figure 4.7, two SOGIs are utilized to filter v_α and v_β signals in the pre-filtering stage. Additionally, the SOGIs function as a Quadrature Signal Generator (QSG), producing quadrature filtered versions of v_α and v_β signals which are $qv`_\alpha$ and $qv`_\beta$ [87].

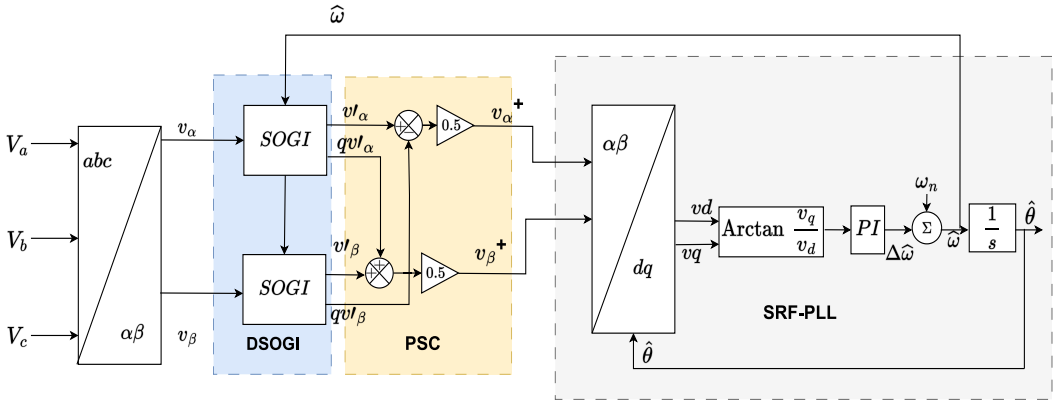

Figure 4.7 DSOGI-PLL

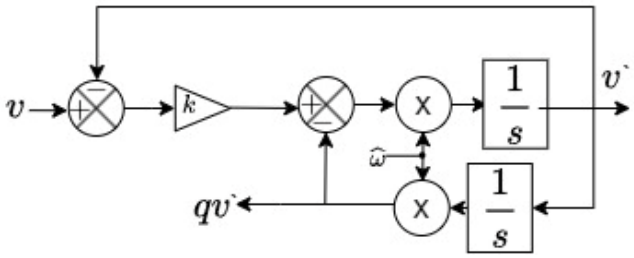

Figure 4.8 QSG-SOGI block

The signals from the QSG- SOGI blocks are processed through the PSC to reveal the FFPS components. Finally, these components are fed into the SRF-PLL to extract the grid frequency and phase. The detected grid frequency $\hat{\omega}$ can be fed back to the QSG-SOGI blocks to ensure the DSOGI-PLL remains frequency adaptive [57][87].

The QSG-SOGI block is crucial for harmonic rejection, noise filtering, and producing quadrature signals. Its transfer functions are given in (4.10):

$$G_d(s) = \frac{k.\omega_1.s}{s^2 + k.\omega_1.s + {\omega_1}^2} \tag{4.10}$$

$$G_q(s) = \frac{k.{\omega_1}^2}{s^2 + k.\omega_1.s + {\omega_1}^2}$$

Where:

- ω_1: Estimated frequency.
- k: Gain factor of the QSG-SOGI block

Both transfer functions share the same second-order denominator, which represents a resonant system tuned at the estimated angular frequency ω_1. The numerator of $G_d(s)$ contains the term s, which introduces a 90° phase lead around the resonant frequency. As a result, the output of $G_d(s)$ produces the in-phase (direct) component of the fundamental signal.

In contrast, the numerator of $G_q(s)$ does not contain the term s and therefore does not introduce the same phase shift. Due to the common denominator, the output of $G_q(s)$ lags the output of $G_d(s)$ by approximately 90° at ω_1. This phase relationship can be verified by evaluating the frequency response at $s = j\omega_1$, where the magnitudes of both transfer functions become equal while their phase difference approaches 90°.

Consequently, when both transfer functions are excited by the same input, the QSG-SOGI generates two signals with equal magnitude and a quadrature phase relationship. This orthogonal signal pair forms the basis for quadrature signal generation and is used for reference frame transformations and phase estimation.

According to [88], the optimal value of gain factor of the QSG-SOGI block of the DSOGI-PLL, k, is 1.414; this value results in favorable settling time, overshoot and harmonic rejection capabilities, and leads to a damping factor of 0.7 in SOGI blocks. Therefore, this value is used in the proposed DSOGI -PLL.

The DSOGI-PLL combines band-pass and low-pass filtering capabilities to extract the fundamental frequency. Filter bandwidth is exclusively determined by the gain value and independent of frequency estimation. At the center frequency as shown in Figure 4.9, the gain of both direct (G_d(s)) and quadrature (G_q(s)) is unitary, while the phase of G_q(s) is lagging 90°. Independent of the input signal frequency, the output *qv'* always lags 90° from *v'*. Therefore, when the frequency of the input signal deviates from the center frequency, the filter output signal differs only in magnitude.

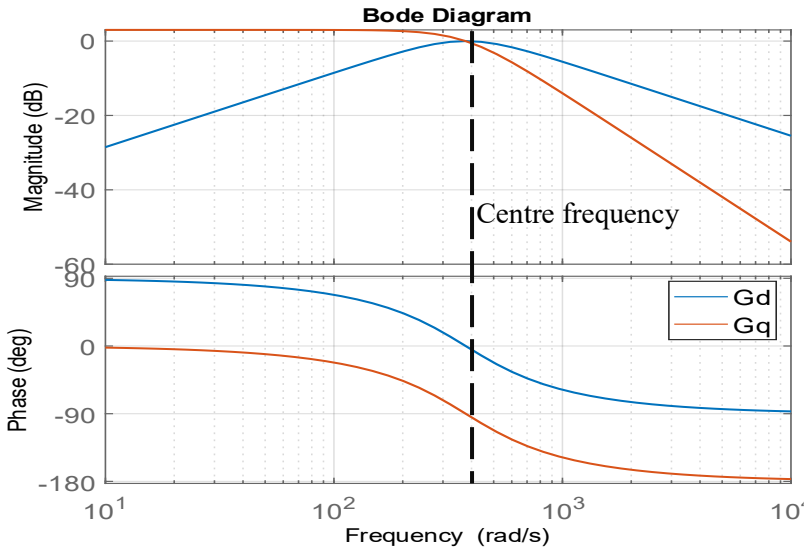

Figure 4.9 Bode plots of Gd and Gq

This section describes how the QSG-SOGI blocks, in conjunction with the Positive Sequence Calculator (PSC), extract the positive sequence components from the three-phase voltage signals. The following provides the mathematical process and justification for extracting the positive sequence. First consider the transformation of three-phase voltage (v_{abc}) into positive (v^{+}_{abc}) and negative (v^{-}_{abc}) sequences:

$$v_{abc}^{+} = [T_p]v_{abc} \;\; and \; v_{abc}^{-} = [T_n]v_{abc} \tag{4.11}$$

$where$:

$$[T_p] = \frac{1}{3}\begin{bmatrix} 1 & a & a^2 \\ a^2 & 1 & a \\ a & a^2 & 1 \end{bmatrix}, [T_n] = \frac{1}{3}\begin{bmatrix} 1 & a^2 & a \\ a & 1 & a^2 \\ a^2 & a & 1 \end{bmatrix}, a = e^{\frac{j2\pi}{3}}$$

For the αβ -frame, the positive sequence ($v_{\alpha\beta}^{+}$) is derived as:

$$v_{\alpha\beta}^{+} = [T_{\alpha\beta}]v_{abc}^{+} = [T_{\alpha\beta}][T_p]v_{abc} = [T_{\alpha\beta}][T_p]\left[T_{\alpha\beta}\right]^{T} v_{\alpha\beta} \tag{4.12}$$

$where$:

$$[T_{\alpha\beta}] = \frac{2}{3}\begin{bmatrix} 1 & -\frac{1}{2} & -\frac{1}{2} \\ 0 & \frac{\sqrt{3}}{2} & \frac{\sqrt{3}}{2} \end{bmatrix}$$

After simplifying $[T_{\alpha\beta}][T_p]\left[T_{\alpha\beta}\right]^{T}$ in (4.12), the positive sequence values as facilitated by the SOGI and PSC, are expressed as in (4.13):

$$v_{\alpha\beta}^{+} = \frac{1}{2}\begin{bmatrix} 1 & -q \\ q & 1 \end{bmatrix} v_{\alpha\beta} \;, q = e^{-\frac{j\pi}{2}} \tag{4.13}$$

4.3.1.2 Small signal model of DSOGI-PLL

Even though the DSOGI-PLL has a complex structure, it can be represented using the small signal model shown in Figure 4.10, as has been proposed in [57].

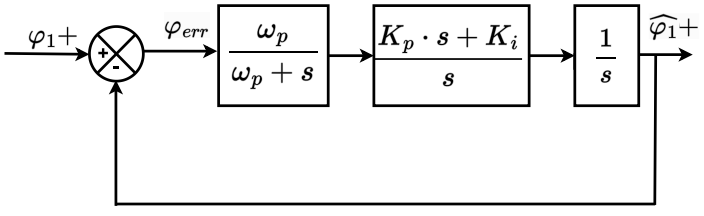

Figure 4.10 Small signal model of DSOGI-PLL

Here $\omega_p = \frac{k\widehat{\omega}}{2}$ and K_p , K_i are the paramters of the PI controller. Based on the model, the open loop and closed loop transfer functions of the DSOGI-PLL can be obtained as in (4.14) and (4.15) [57], [89].

$$G_{ol-DSOGI} = \frac{K_p s + K_i}{s^2} . \frac{\omega_p}{\omega_p + s} \tag{4.14}$$

$$G_{cl-DSOGI} = \frac{(K_p s + K_i).\omega_p}{s^3 + \omega_p s^2 + \omega_p K_p s + K_i \omega_p} \tag{4.15}$$

Characteristic equation of the DSOGI-PLL can be equated to the standard factorized form for an underdamped system as:

$$s^3 + \omega_p s^2 + \omega_p K_p s + K_i \omega_p = (s + A)(s^2 + 2\xi\omega_{nat} s + {\omega_{nat}}^2) \tag{4.16}$$

By equating the corresponding parameters:

$$\omega_p = (2\xi\omega_{nat} + A);\ ({\omega_{nat}}^2 + 2\xi\omega_{nat} A) = \omega_p K_p;\ A{\omega_{nat}}^2 = K_i \omega_p \tag{4.17}$$

Same design criteria as for the SRF-PLL should be considered here to design the DSOGI-PLL. Cut off frequency was selected same as the SRF-PLL which is ω_c =75.39 rads^{-1} for a 60 Hz System. According to the definition of the ωc and the PM, by substituting s = jωc into G_{olSRF}:

$$\left|G_{olSRF(j\omega c)}\right| = 1$$

To satisfy all the design criteria, $K_p = 70$; $K_i = 2416$ were selected. The resulting phase margin (PM) is calculated as:

$$\text{PM}=\tan^{-1}\frac{\omega c}{K_i/K_p} - \tan^{-1}\frac{\omega c}{\omega_p} = 49.8^o \quad (4.18)$$

Figure 4.11 shows the Bode plot of DSOGI-PLL considering all these design criteria.

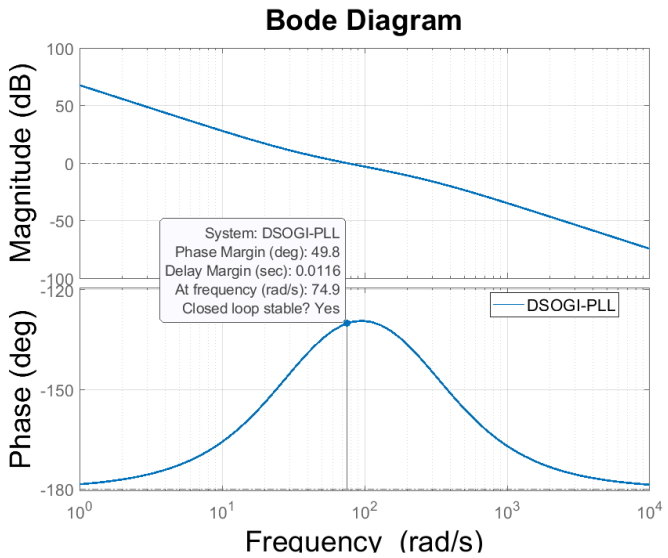

Figure 4.11 Bode plot of DSOGI-PLL with $K_p = 70$; $K_i = 2416$

4.3.2 Modifications Proposed to Improve DSOGI-PLL

To further improve the performance of DSOGI-PLL during the transient periods, it is modified by introducing a transient eliminator and an adaptive bandwidth mechanism. Transient eliminator is used to detect transient in the grid and to freeze the frequency for short period of time until the system becomes stable. This frequency is used in the controller of the DSOGI -PLL.

The adaptive bandwidth mechanism allows the PLL to dynamically adjust its response, achieving faster phase tracking, particularly during transients. This feature significantly

aids in the synchronization of the control system under rapidly changing grid conditions, improving overall system robustness and stability. By minimizing phase errors and expediting the synchronization process of PLLs, it is expected that the stability and resilience of power systems in the face of transient conditions arising from various disturbances can be significantly improved. Before delving into the proposed modifications

4.3.2.1 Transient Eliminator

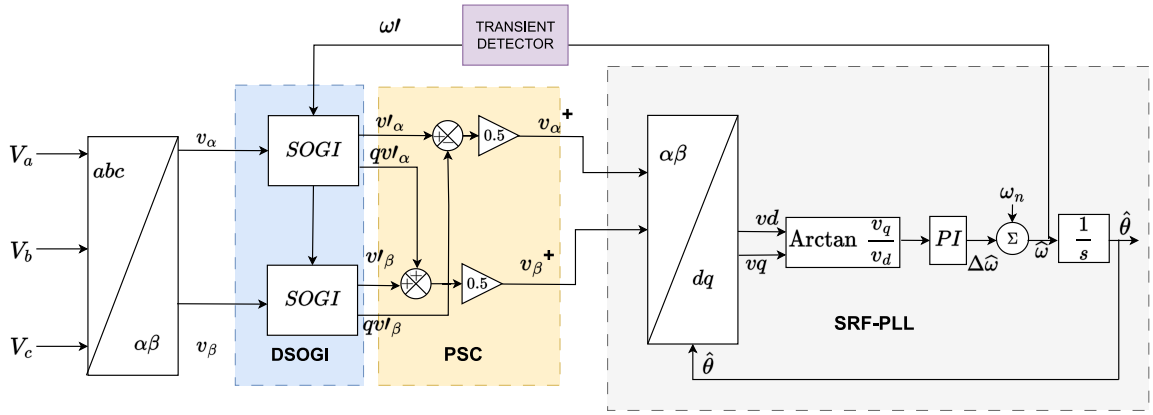

Figure 4.12 Modified DSOGI-PLL

The DSOGI-PLL relies on the frequency fed to its SOGI blocks for effective filtering. However, during transient events, fluctuations in the detected frequency can compromise its filtering capability. In response to this challenge, a transient eliminator which activates upon observing a sudden change in frequency is incorporated into the system. When a transient is identified by the transient eliminator, it temporary freezes the frequency at the value just before the inception of transient for a period of T_{fz}. This frozen frequency is then provided to the SOGI blocks. By doing so, the DSOGI-PLL mitigates the potential undesirable outcomes associated with transient events, ensuring a more stable and effective filtering process. This adaptive mechanism contributes to improve the robustness of the DSOGI-PLL, particularly in handling transient conditions, such as faults. Detection of the

transients can be achieved either by examining the voltage waveform or using the phase error which can be obtained from an intermediate stage of the DSOGI-PLL.

1. Voltage Waveform-Based Transient Detection

The voltage waveform-based method examines the three-phase instantaneous voltages (V_{abc}) to identify transient events. Each phase is monitored to determine if a deviation exceeds a predefined threshold (δ). If any phase voltage crosses this threshold, the transient is detected, and the system freezes the frequency for a predefined duration (T_x) to stabilize the operation. This algorithm is illustrated in Figure 4.13 . To further minimize oscillations in frequency and prevent sudden changes during or after a transient event, ROCOF is limited to 8 Hz/s. In practical implementations, systems connected to inverter-based resources (IBR) typically restrict the maximum allowable ROCOF to around 4 Hz/s [90], [91].

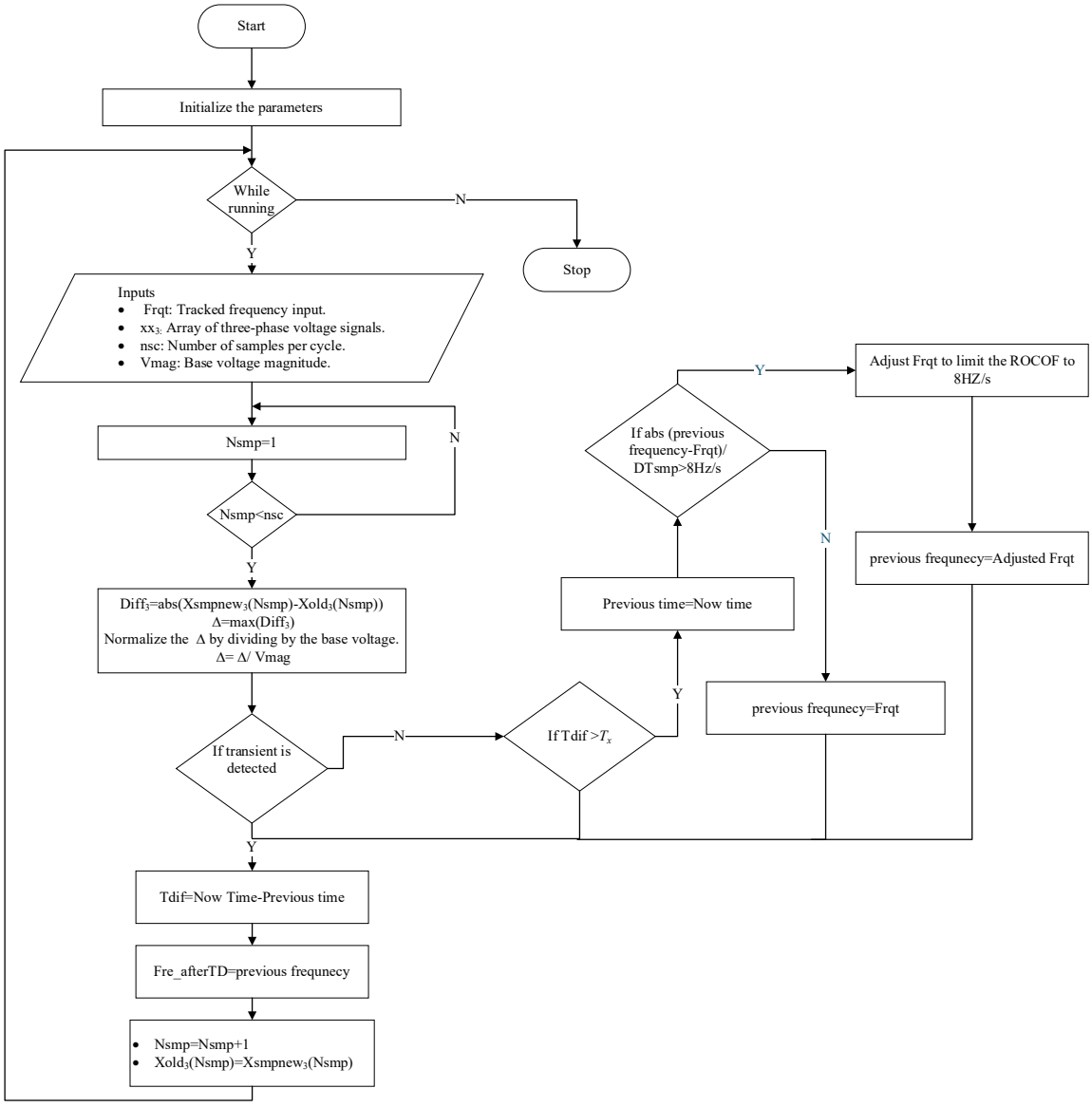

Figure 4.13 Transient detecting algorithm using voltage waveform

2. Phase Error-Based Transient Detection

Transient detection can also be achieved using the phase error obtained from any PLL as shown in Figure 4.1. The phase error, which represents the difference between the input and output phase of the PLL, can indicate transients if it exceeds a threshold. This method is tightly integrated with the PLL and offers a simpler implementation.

Both methods, voltage waveform-based and phase error-based, are implemented and used into the advanced PLL to enhance transient detection and system stability. The voltage waveform-based approach is preferred for frequency freezing, particularly in systems exposed to long-term harmonic distortion. Under such conditions, the phase error may fail to converge to zero. As a result, the transient eliminator may be triggered repeatedly, even in the absence of actual transients. This repeated activation can lead to system instability and false transient detections, undermining the reliability of the PLL.

Conversely, the phase error-based method is suitable for adaptive bandwidth enhancement, as the threshold used in this context can tolerate phase errors introduced by harmonics. However, for frequency freezing, precise transient detection is critical, making the voltage waveform-based method more reliable due to its resilience against harmonic interference.

4.3.2.2 Adaptive Bandwidth Mechanism

The Adaptive Bandwidth scheme is activated when the phase error greater than a threshold value, ε, is detected as illustrated in Figure 4.14. Upon detecting such deviations, the bandwidth is rapidly increased, allowing the PLL to respond swiftly to transient events and enhancing its capacity to track and synchronize with grid phase changes promptly. This dynamic adjustment supports system stability during crucial moments, such as fault conditions or sudden grid fluctuations. As conditions normalize, the bandwidth is gradually reduced, preventing overshooting, and minimizing the introduction of unnecessary phase errors during the transition back to steady-state operation. This is achieved by linearly changing the control gains to original values with time, offering an effective means of

enhancing PLL performance in dynamic power system environments by providing a balance between precision and adaptability.

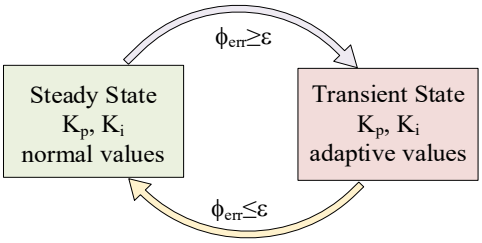

Figure 4.14 Adaptive bandwidth mechanism

When increasing the bandwidth, it is important to ensure that the system remains underdamped to avoid slow responses. According to previous research it is desirable to have 0.7 as the damping ratio of the system to have favorable operation [87]. Therefore, by considering the open loop transfer function described in (4.19), it is possible to derive the characteristic equation of the system as:

$$s^3 + \omega_p \cdot s^2 + K_p \cdot \omega_p \cdot s + K_i \cdot \omega_p = 0 \tag{4.19}$$

If the system considered as an underdamped system, equation in (4.19) can be factorized as shown in (4.20) and (4.21), where A is a constant and ω_{nat} is the natural frequency and ξ is the damping coefficient.

$$(s + A)(s^2 + 2\xi\omega_{nat}s + {\omega_{nat}}^2) = 0 \tag{4.20}$$

$$s^3 + (2\xi\omega_{nat} + A)s^2 + ({\omega_{nat}}^2 + 2\xi\omega_{nat}A)s + A{\omega_{nat}}^2 = 0 \tag{4.21}$$

Using these equations, appropriate $K_p$and K_i values can be determined by following the procedure illustrated in Figure 4.15.

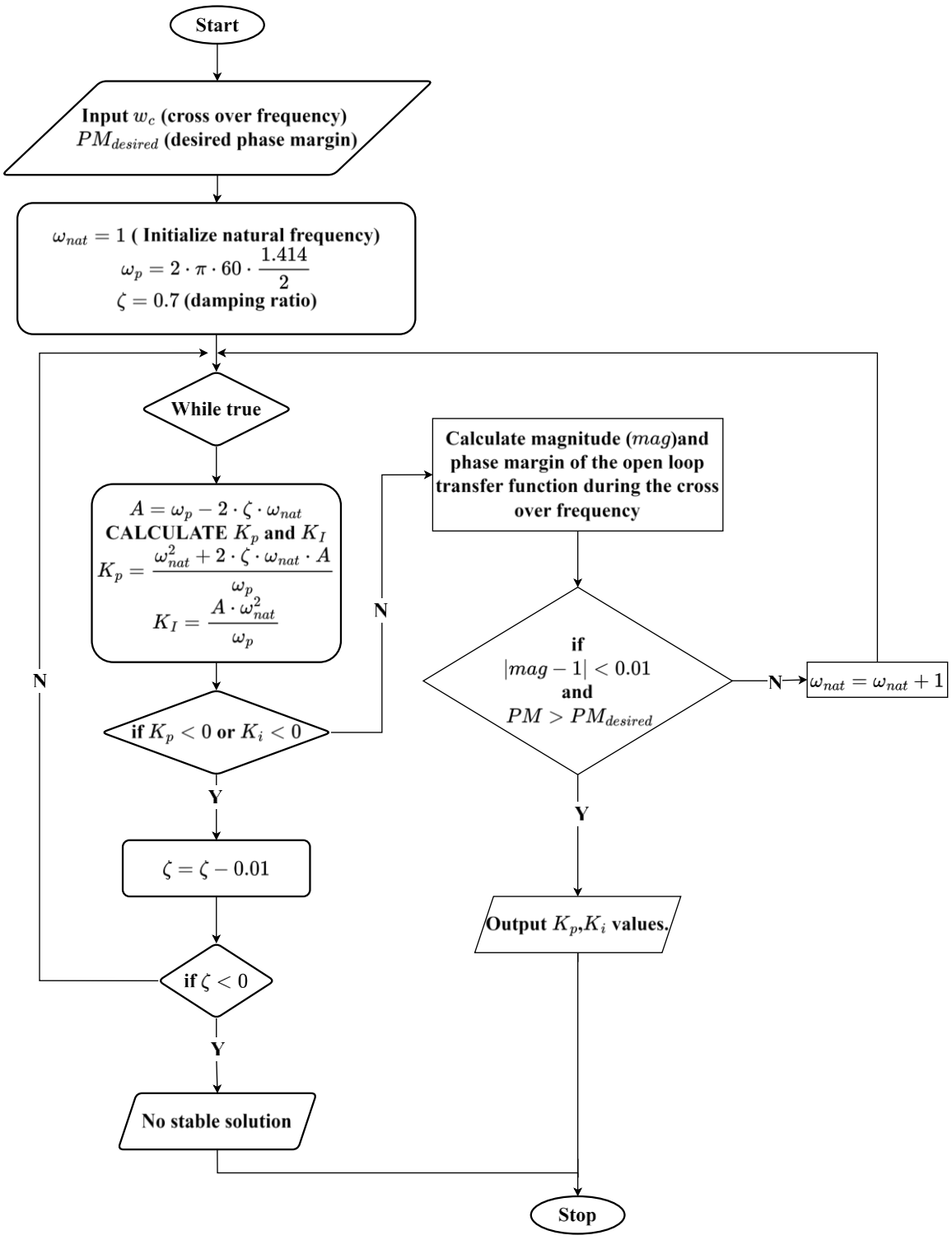

Figure 4.15 Adaptive bandwidth gain calculating mechanism.

Table 4.1 presents the identified parameters for different bandwidth (BW) enhancements. Increasing BW improves the system's responsiveness (ω_c) by enabling faster transient response. However, this improvement introduces trade-offs, particularly a reduction in phase margin (PM), which affects stability. Notably, as BW enhancement exceeds 5 times, the phase margin becomes critically low, jeopardizing system stability. A BW enhancement below 5 times strikes a balance between achieving a faster transient response and maintaining sufficient phase margin, ensuring both stability and improved dynamic performance.

Table 4.1 Parameters identified for different Bandwidths.

BW multiplier	**ω_c**	**K_p**	**K_i**	**ξ**	**PM**
2	150.78	135.19	1915.33	0.70	55.13
3	226.17	295.07	1511.48	0.56	48.50
3.5	263.87	368.07	1920.65	0.55	44.50
4	301.56	450.83	1078.73	0.53	40.59
5	376.95	639.59	3776.47	0.31	45.02
7	527.73	586.43	4144.80	0.33	26.03

4.4 Implementation of the proposed PLL model in PSCAD/ EMTDC simulation software

The proposed advanced PLL model is implemented within the PSCAD/EMTDC simulation environment. It builds upon the standard built-in PLL model provided by PSCAD/EMTDC by integrating additional advanced functionalities. As illustrated in Figure 4.16 , the user interface of this PLL model allows operation in two modes: the standard SRF - PLL mode and an enhanced mode with adaptive features. By default, the model functions as a conventional SRF-PLL unless the advanced features are explicitly enabled. One of the key configurations is automatic estimation of PI controller parameters to ensure stable system performance. Alternatively, users may manually input their preferred PI gains to suit specific design requirements.

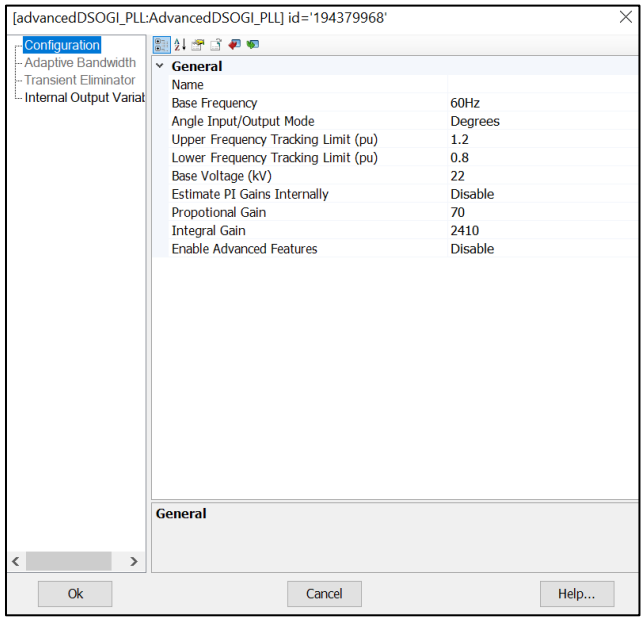

Figure 4.16 User interface of the advanced PLL

Figure 4.17 represents the configuration interfaces for the advanced features. These include:

- Adaptive Bandwidth: Users can select from predefined BW enhancements (i.e., 2-times, 3-times, or 4-times) and specify the desired phase margin.
- Transient Eliminator: Users can define the duration for which the PLL output frequency is frozen during detected transients, as well as set the sampling rate in terms of samples per cycle.

These configurable features provide flexibility to identify optimal parameter settings for improved robustness and dynamic performance of the PLL under varying grid conditions

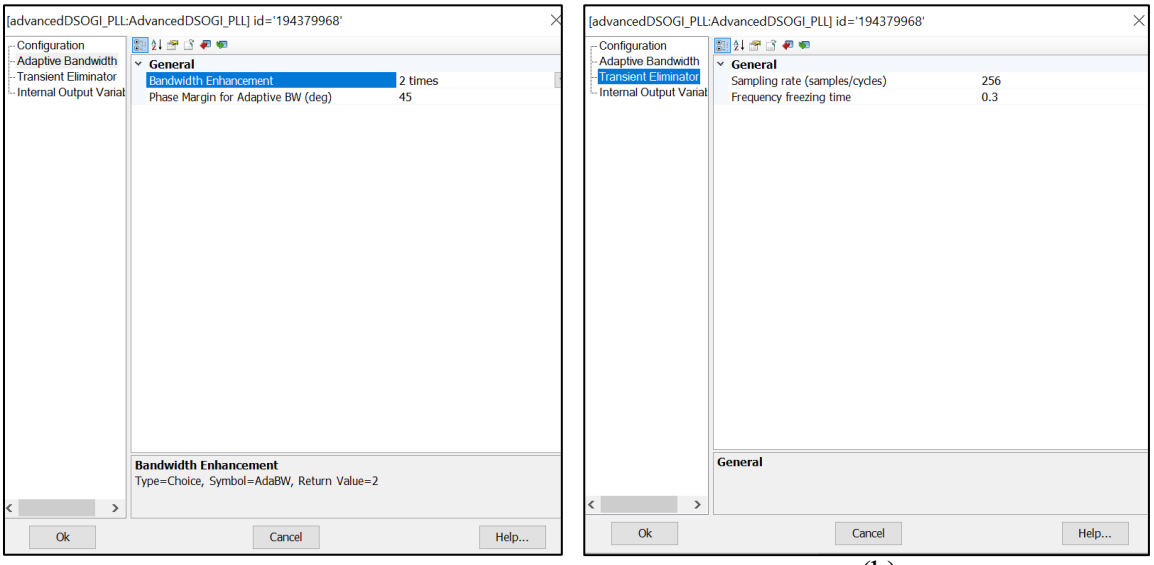

Figure 4.17 Advanced feature tabs: (a) Adaptive Bandwidth (b) Transient Eliminator

4.5 Testing Using Synthetic Signals

Power systems often experience transients, such as faults, which induce magnitudes changes, phase jumps, and frequency deviations in the voltage waveforms. However, the

extents of these changes are system dependent and cannot be precisely controlled. Therefore, the use of synthetic signals with controlled variations in magnitude, phase, and frequency mimicking these scenarios is the first approach used for testing the proposed advanced PLL.

A synthetic waveform generator was implemented using PSCAD/EMTDC master library components to allow for individual control of voltage magnitude, phase, and frequency for each phase. Additionally, the generator can introduce harmonics into the three-phase waveforms.

4.5.1 Comparison of Conventional SRF PLL and DSOGI-PLL

This section evaluates the performance of the SRF-PLL and the DSOGI-PLL under dynamic and transient conditions. The analysis considers both balanced and unbalanced scenarios, along with various transient events, to highlight differences in robustness and tracking accuracy.

4.5.1.1 Performance Under Balanced Conditions.

Figure 4.18 illustrates the behaviour of SRF-PLL and the DSOGI-PLL under balanced transient conditions.

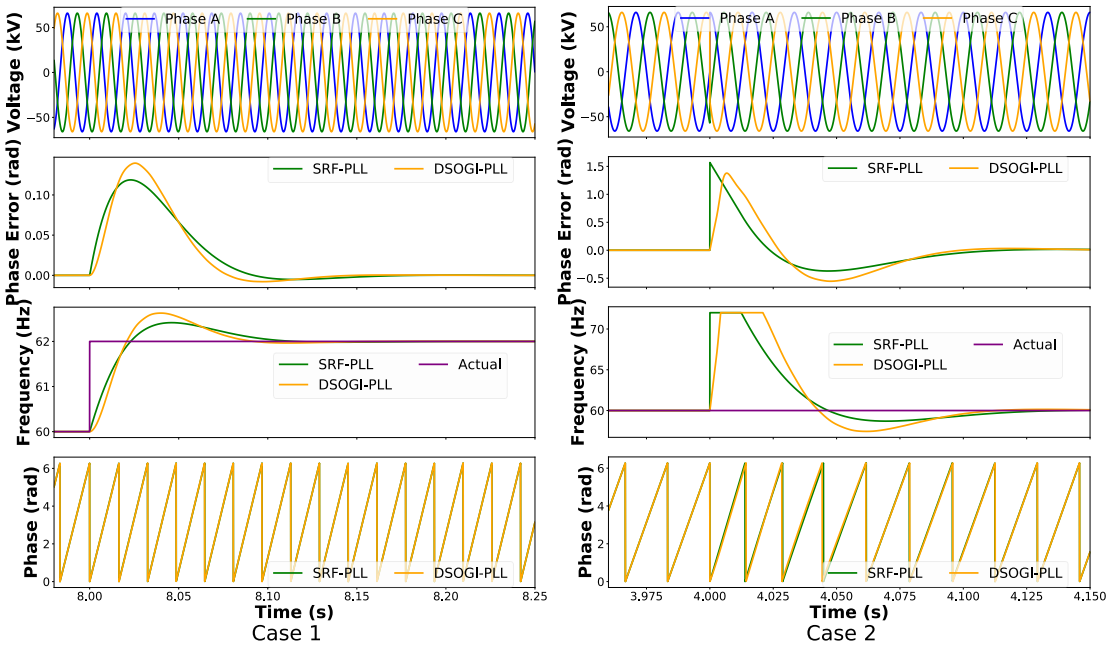

Figure 4.18 Performance of SRF-PLL and DSOGI-PLL under balanced conditions

The transient response of the PLLs is tested under two scenarios: a frequency step-change (Case 1) and a 90-degree phase jump (Case 2). In these cases, both SRF-PLL and DSOGI-PLL exhibit comparable phase and frequency tracking characteristics, maintaining stable performance. Under ideal conditions, with no harmonics or unbalanced elements in the system, both SRF-PLL and DSOGI-PLL perform similarly. Their outputs are comparable, demonstrating effective phase and frequency tracking with no significant differences. The bandwidth and proportional-integral (K_p, K_i) values for both PLLs are calculated as per Section 4.2.2 and 4.3.1.2, ensuring a fair comparison.

4.5.1.2 Performance Under Harmonics and Unbalanced Conditions

When subjected to unbalanced and harmonic-rich environments, the DSOGI-PLL outperforms the SRF-PLL in robustness and stability. Figure 4.19 illustrates their behavior under four specific test cases:

- **Case 1:** Magnitude of Phase C is reduced to 0.5 pu at 1.0 seconds.
- **Case 2:** Harmonics are injected into the system at 1.0 seconds.
- **Case 3:** A 90-degree phase jump is introduced to Phase C, to the harmonic-injected system.
- **Case 4:** A frequency ramp of 4 Hz/s is applied at 8.0 seconds to the harmonic-injected system.

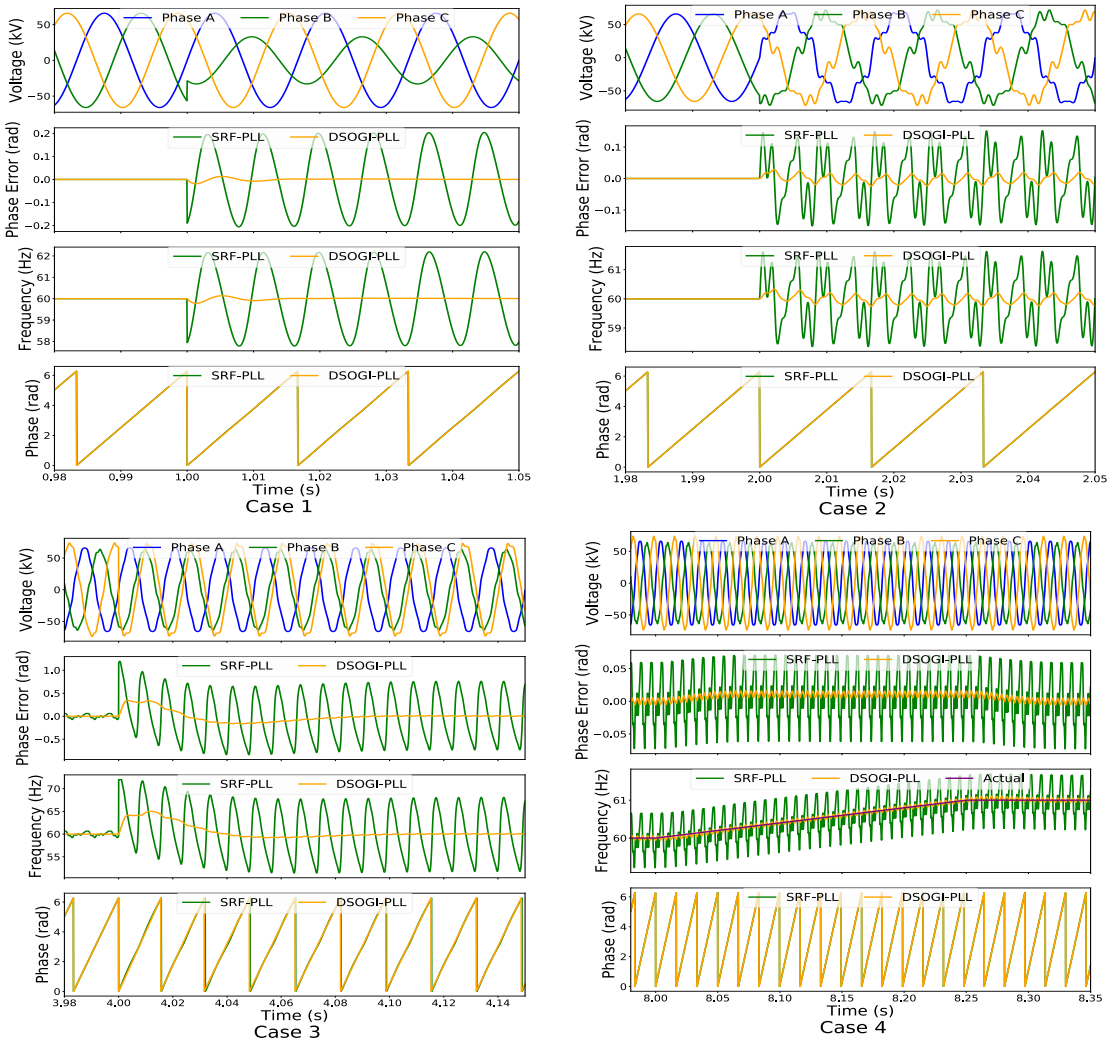

Figure 4.19 Comparison of SRF -PLL with conventional DSOGI-PLL for Cases 1 to 4

In Case 1 and Case 3, where transients such as magnitude reduction and a 90-degree phase jump are introduced, the SRF-PLL exhibits oscillatory frequency and noticeable phase error, while the DSOGI-PLL shows a slight overshoot in both phase error and frequency immediately after the disturbance but settles quickly to steady-state. In Cases 2 and 4, where harmonics are injected along with additional transients, the SRF-PLL displays significant noise in its frequency output and high phase error throughout, whereas the

DSOGI-PLL maintains smooth frequency tracking and lower phase error, with only very low-magnitude oscillations compared to the SRF-PLL. In all these scenarios, the DSOGI-PLL demonstrates consistent tracking performance, effectively handling transient events without significant degradation in output quality.

4.5.2 Comparison of Conventional DSOGI-PLL and Proposed Adaptive DSOGI-PLL

This section presents a detailed evaluation of the conventional DSOGI-PLL and the proposed adaptive DSOGI-PLL under various dynamic and transient scenarios. The proposed modifications, which include the use of an adaptive bandwidth mechanism and a transient eliminator, are assessed for their ability to enhance system robustness and accuracy. The scenarios include harmonic injections, three-phase and unbalanced phase jumps, voltage magnitude changes, and frequency ramps. In this work, the bandwidth is increased by 5 times during a transient compared to normal operation, with ε set at 0.08 rad, and T_x is defined as 0.3s.

4.5.2.1 Performance Under Harmonic Injection

Figure 4.20 illustrates the response of the DSOGI-PLL systems to a harmonic injection at 2.0 seconds, where 3rd, 5th, and 7th harmonics create a total harmonic distortion (THD) of 30%. The high harmonic content causes the phase error to exceed the threshold, activating the adaptive bandwidth mechanism and transient eliminator in the proposed DSOGI-PLL. Once the phase error falls below the threshold, the adaptive bandwidth returns to its normal bandwidth. During the active period of adaptive bandwidth, the frequency exhibits high-magnitude oscillations; however, as the system transitions back to normal bandwidth, both

configurations—with and without adaptive bandwidth—show similar oscillation magnitudes. Although the frequency oscillations increase when harmonics are introduced, this effect can be effectively mitigated by using the transient eliminator, which freezes the frequency

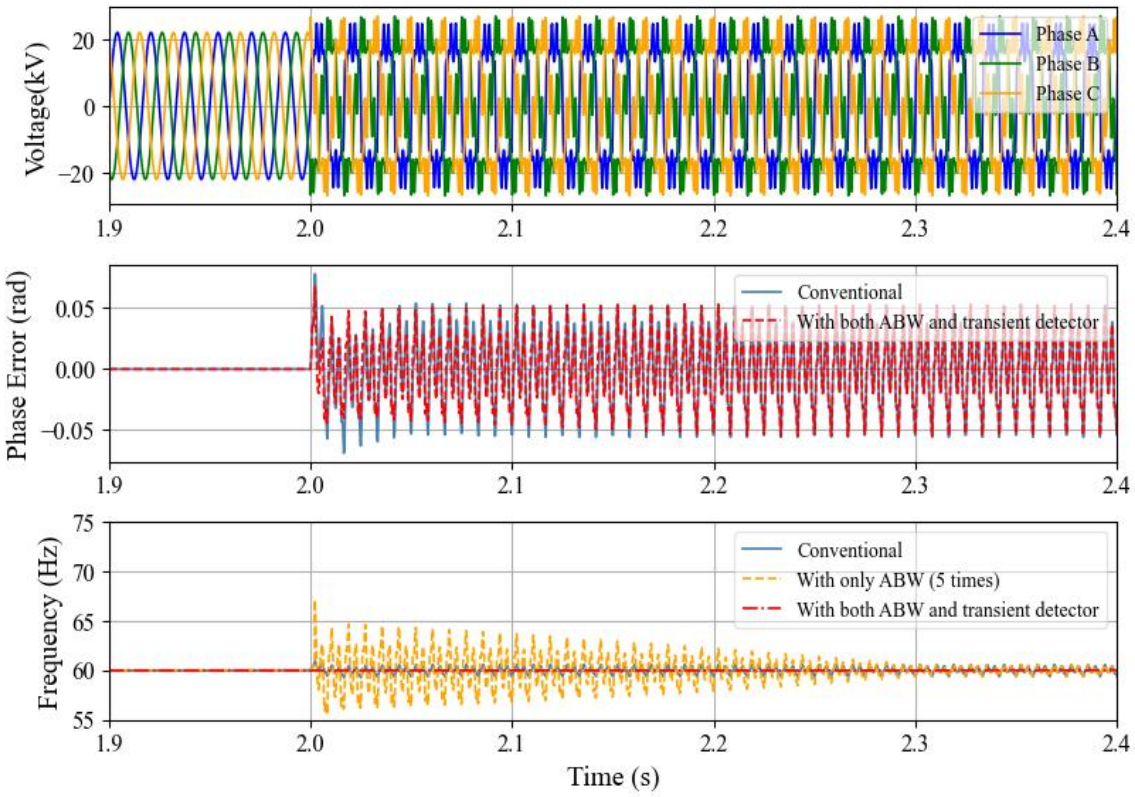

Figure 4.20 Comparison of proposed DSOGI-PLL with conventional DSOGI-PLL applying harmonic at 2.0s

Quantitative performance during harmonic injection is summarized in Table 4.2. This reveals that the proposed DSOGI-PLL achieves lower RMSE values for both phase error (0.027 rad) and frequency (0.001 Hz) compared to the conventional DSOGI-PLL (0.032 rad and 0.350 Hz, respectively). These results underscore the proposed PLL's effectiveness in mitigating oscillations and maintaining stability under high harmonic distortions.

Table 4.2 RMSE values for harmonic injection from 2.05s – 2.15s

	Normal DSOGI-PLL	Proposed DSOGI-PLL
Phase Error (rad)	0.032	0.027
Frequency (Hz)	0.350	0.001

4.5.2.2 Response to Frequency Ramp

Typically, the power system with a high penetration of renewable energy resources usually experiences a higher ROCOF, which typically doesn't exceed 4Hz/s [90], [91]. To demonstrate worst-case scenarios, a frequency ramp of 7Hz/s was used to show that the system can correctly detect the frequency with the proposed modifications. Figure 4.21 illustrates the behavior of the conventional DSOGI-PLL and the proposed DSOGI-PLL under a frequency ramp starting at 2.0 seconds. This scenario demonstrates the proposed adaptive DSOGI-PLL's ability to accurately track frequency without activating the transient eliminator. The results show that both conventional and proposed adaptive DSOGI-PLLs respond very similarly, and the proposed enhancements do not compromise the system's steady state performance.

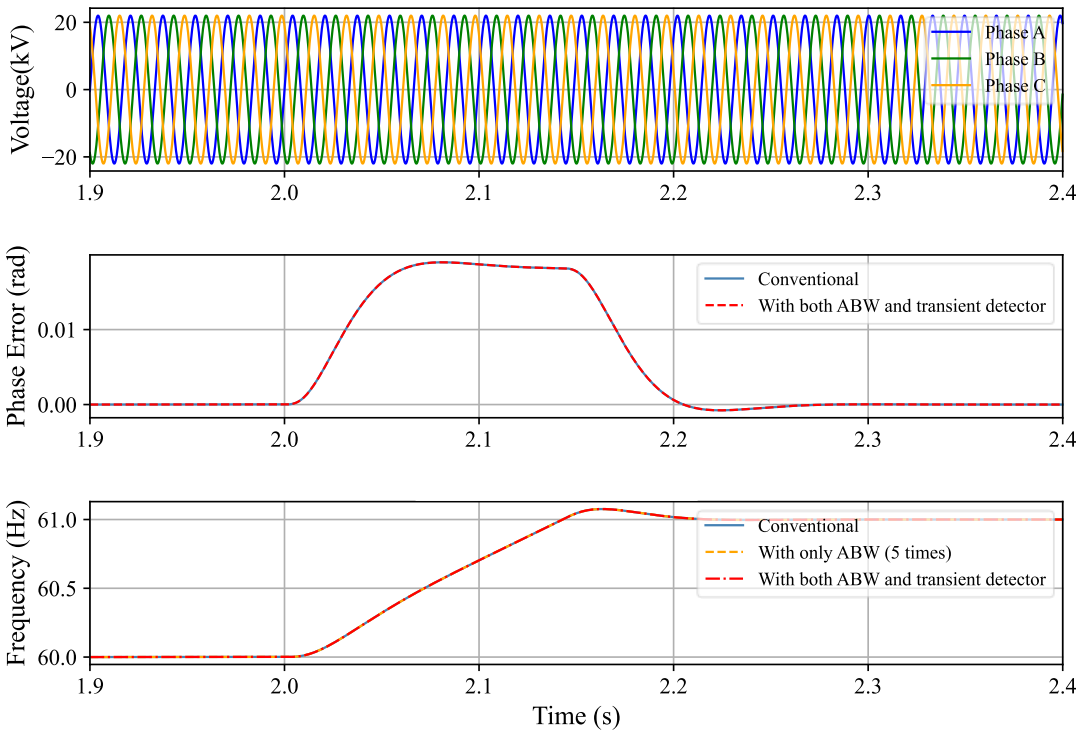

Figure 4.21 Comparison of proposed DSOGI-PLL with conventional DSOGI-PLL under a frequency ramp starting at 2.0s

4.5.2.3 Performance Under Voltage Magnitude Changes

Figure 4.22 highlights the response to a voltage magnitude change from 22 kV to 66 kV at 3.0 seconds. This transient activates both the adaptive bandwidth mechanism and the transient eliminator, allowing for fast phase tracking and reduced phase error overshoot. The proposed DSOGI-PLL achieves a settling time of 0.015 seconds and an overshoot of 0.08 rad, significantly outperforming the conventional system, which has a settling time of 0.04 seconds and an overshoot of 0.15 rad. These results emphasize the improved dynamic response of the proposed PLL.

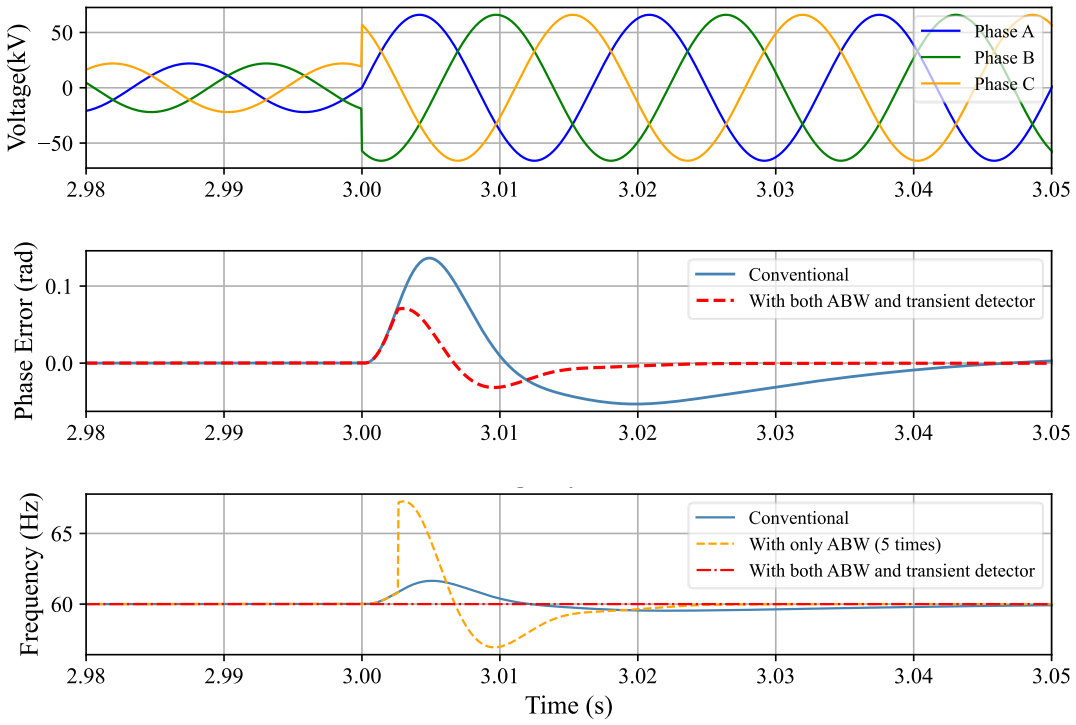

Figure 4.22 Comparison of proposed DSOGI-PLL with conventional DSOGI-PLL applying a voltage magnitude change at 3.0s

4.5.2.4 Phase Jump Scenarios

Figure 4.23 and Figure 4.24 compare the performance of the proposed method with the conventional method under specific conditions. Figure 4.23 illustrates an unbalanced phase jump of 90° in phase A, while Figure 4.24 demonstrates a balanced phase jump. In both cases, the phase jump occurs at 2.0 seconds and returns to the normal position around 2.2 seconds.

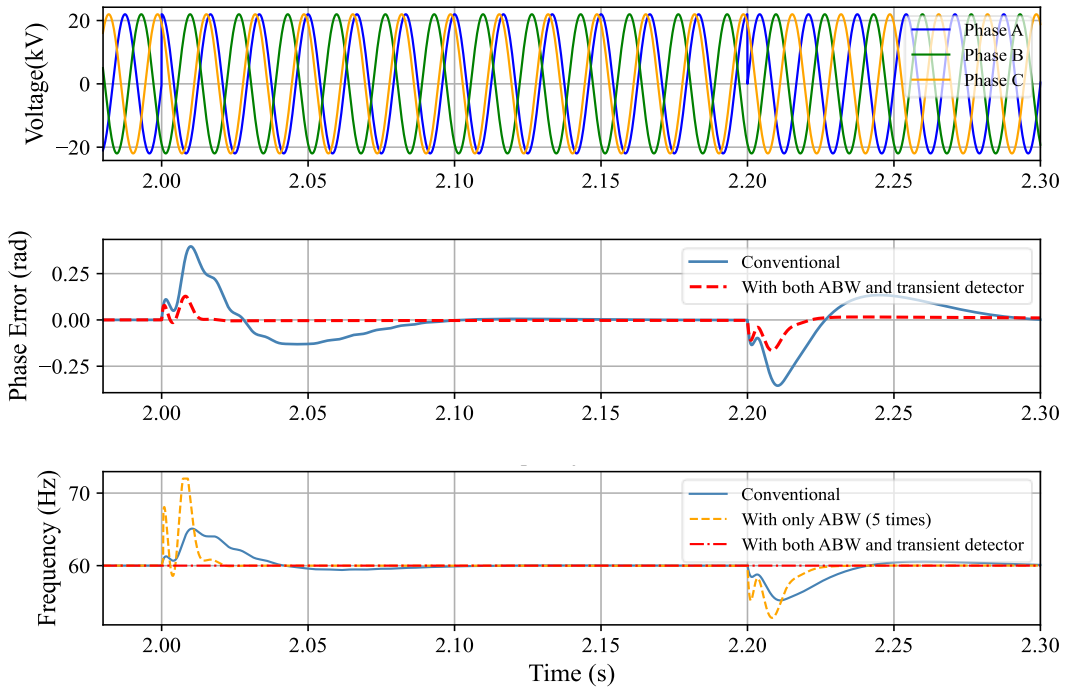

Figure 4.23 Comparison of proposed DSOGI-PLL with conventional DSOGI-PLL applying an unbalanced phase jump change at 2.0s

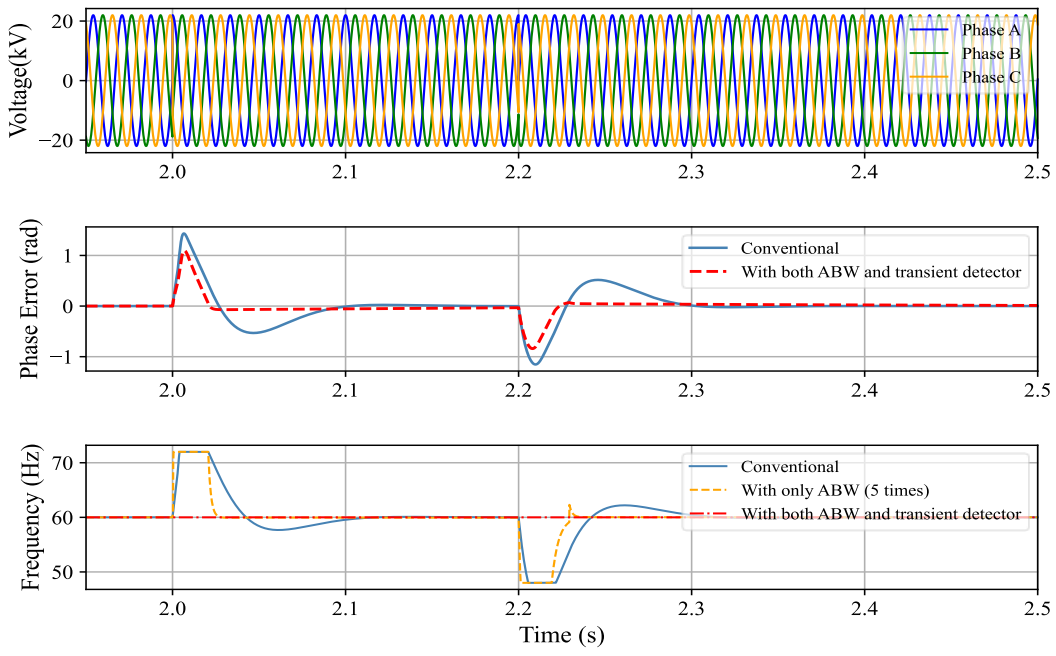

Figure 4.24 Comparison of proposed DSOGI-PLL with conventional DSOGI-PLL applying a balanced phase jump at 2.0s

These transients activate both the adaptive bandwidth and transient eliminator in the proposed DSOGI-PLL. Table 4.3 provides a quantitative comparison of the settling time and overshoot for balanced and unbalanced phase jumps.

Table 4.3 Comparison of the Proposed DSOGI-PLL for Different Phase Jumps

	Normal DSOGI-PLL		**Proposed DSOGI-PLL**	
	Settling time (s)	Overshoot (rad)	Settling time (s)	Overshoot (rad)
Phase jump (unbalanced)	0.1	0.3	0.02	0.1
Phase jump(balanced)	0.1	1.2	0.02	1

The proposed adaptive DSOGI-PLL significantly reduces the settling time and overshoot, demonstrating enhanced robustness and stability during phase jump scenarios. While the use of adaptive bandwidth can introduce frequency oscillations, these are effectively mitigated by the transient eliminator. The transient eliminator enhances the overall precision and stability of the PLL by addressing potential adverse effects caused by increased bandwidth during transients.

Overall, the proposed adaptive DSOGI-PLL demonstrates robustness and accuracy under diverse transient conditions compared to the conventional DSOGI-PLL, particularly in phase detection and synchronization. The integration of the adaptive bandwidth mechanism and the transient eliminator allow the system to effectively handle challenging scenarios such as harmonic injections, phase jumps, and voltage magnitude changes. These modifications significantly enhance the PLL's performance by reducing settling times,

minimizing overshoots, and maintaining system stability even under dynamic operating condition.

4.6 Summary

This chapter introduces enhancements to the DSOGI-PLL for robust grid synchronization under dynamic conditions. It begins with an overview of the PLL and SRF-PLL, outlining their structures, limitations, and tuning methods. The DSOGI-PLL is presented as an advanced solution, featuring SOGI blocks and Positive Sequence Calculators for improved harmonic rejection and frequency adaptability.

Key enhancements include:

- **Transient Eliminator**: Freezes frequency during transients to stabilize filtering and avoid frequency fluctuations.
- **Adaptive Bandwidth**: Dynamically adjusts bandwidth for faster phase tracking during disturbances and restores it to normal during steady state, ensuring stability and precision.

The chapter also presents synthetic waveform comparisons under various transient scenarios such as phase jumps, harmonic injections, and frequency ramps. These simulations demonstrate the performance of the proposed DSOGI-PLL compared to conventional designs, highlighting improvements in accuracy, dynamic response, and overall robustness.

Chapter 5

Performance Assessment of Improved Inverter Control Strategies

5.1 Introduction

This chapter details the testing of the proposed modifications to the DSOGI-PLL using three distinct approaches that include two test systems simulated in PSCAD/EMTDC. These tests evaluate the performance improvements in terms of the tracking accuracy and the quality of dynamic responses. The chapter explores the incorporation of power reserve control into a solar PV power plant and analyzes of its impact on the primary frequency response of the system. The chapter also includes a comprehensive discussion on the solar PV systems utilized in the study.

5.2 Solar Plant Connected to a Grid

This test demonstrates application of PLLs to implement a solar plant converter. The solar PV plant is connected to a voltage source behind an impedance, which is a simplified representation of a grid. The solar PV inverter uses decoupled control system, which relies on the PLL performance. This system facilitates evaluating the PLL performance under actual renewable energy integration conditions, considering intermittent solar power generation and grid interactions.

Figure 5.1 illustrates the test system designed for analyzing a solar inverter under grid-connected conditions. A single inverter rated at 0.25 MW is modeled in PSCAD/EMTDC, with its power output scaled using a dedicated PSCAD/EMTDC scaling component to meet the desired requirements. A 5 μs simulation time step was used considering the PWM carrier frequencies of the converters. The voltage source, representing the grid, is configured to allow dynamic adjustments to magnitude, phase, and voltage, enabling the simulation of various grid conditions. Temporary faults are applied to one of the transmission lines to analyze the inverter's response to disturbances, including stability and recovery. This scalable system effectively replicates real-world scenarios and evaluates inverter performance under diverse operational conditions.

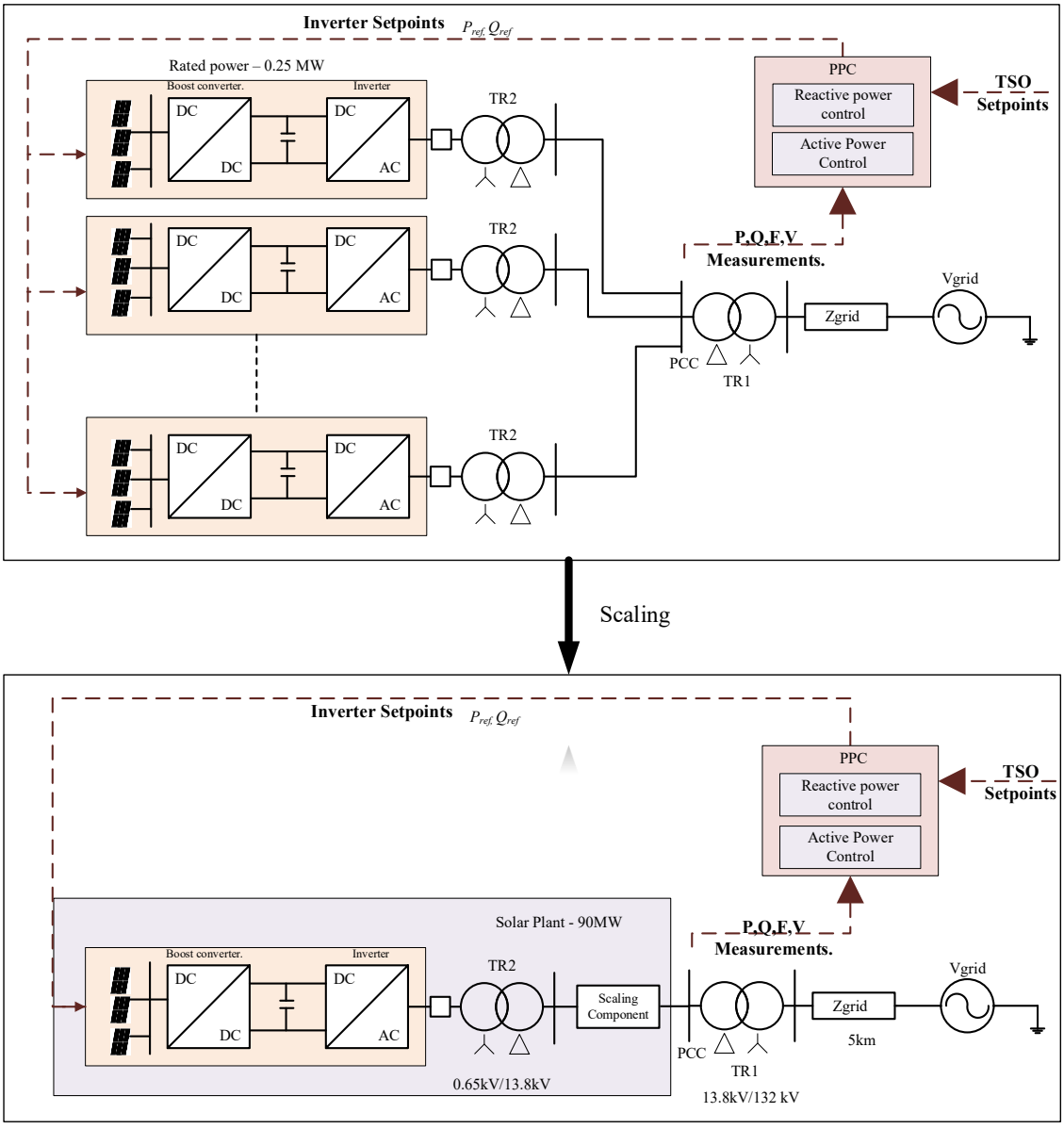

Figure 5.1 PV power plant scaled using the scaling component

5.2.1 Boost Converter Parameter and Control Design

Given the varying terminal voltage of a PV panel due to environmental changes such as temperature or solar intensity, a boost converter is implemented to maintain a desired DC voltage. Figure 5.2 Boost Converter shows the schematic of the boost converter.

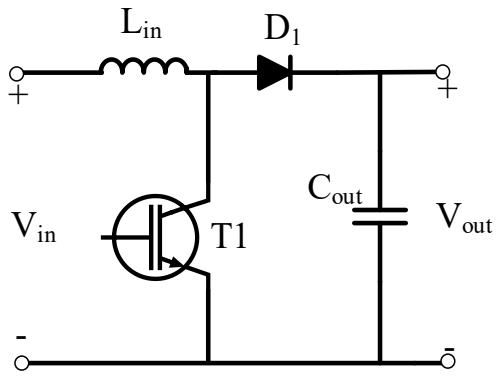

Figure 5.2 Boost Converter

When designing a boost converter, it is crucial to ensure that the components are chosen to optimize performance and efficiency. The general rules for designing the input inductance and output capacitance are as follows:

- In continuous mode operation, the ripple of the inductor current is generally maintained within 20% to 30% of its rated current. This practice helps in controlling the current magnitude and reducing switching losses.

Rated current of the input inductance of a PV plant of 0.25 MW:

$$\mathrm{I_{L_{rated}}} = \frac{\mathrm{P_{rated}}}{\mathrm{V_{in_{rated}}}} = \frac{0.25\mathrm{MW}}{0.839\mathrm{kV}} = 0.308\mathrm{kA} \tag{5.1}$$

Moreover, the ripple of the inductor current (ΔI_L) can be calculated using (5.2). Where k is the ripple factor (0.2 to 0.3), f_{sw} is switching frequency and D is the duty cycle.

$$\Delta I_L = \frac{V_{in} D}{f_{Sw} L_{in}} = \frac{V_{out} D(1-D)}{f_{Sw} L_{in}} \leq k\, I_{L_{rated}} \tag{5.2}$$

$$L_{in} \geq \frac{V_{out}(1-D)D}{f_{Sw} k\, I_{L_{rated}}} \tag{5.3}$$

The relationship between the input voltage, output voltage, and duty cycle in a boost converter is given by (5.4):

$$V_{out} = \frac{V_{in}}{1-D} \tag{5.4}$$

From this equation, the expressions for the maximum and minimum duty cycle can be derived so that the range of duty cycle can be determined as in (5.5).

$$D_{max} = 1 - \frac{V_{in_{min}}}{V_{out}} \;, D_{min} = 1 - \frac{V_{in_{max}}}{V_{out}} \tag{5.5}$$

As seen from (5.2) the right-side expression has a largest value when D = 0.5. Therefore,

$$\text{if } D_{min} < 0.5 < D_{max} \quad : \; L_{in} \geq \frac{V_{out}}{4 f_{Sw} k\, I_{L_{rated}}} \tag{5.6}$$

$$\text{if } D_{min} < D_{max} < 0.5 \quad : \; L_{in} \geq \frac{V_{out}(1-D_{max})\; D_{max}}{f_{Sw} k\, I_{L_{rated}}}$$

$$\text{if } 0.5 < D_{min} < D_{max} \quad : \; L_{in} \geq \frac{V_{out}(1-D_{min})\; D_{min}}{f_{Sw} k\, I_{L_{rated}}}$$

To determine minimum and maximum V_{in}, a variation of temperature as ±20ºC and irradiation level of ±300 Wm^{-2} can be considered.

Table 5.1 Summary of L_{in} calculation

Parameter	**Value/Range**	
PV System Parameters at STC (Rated parameters)		
Prated	0.25MW	
Irated	0.308kA	
Vrated	0.839kV	
	At T=45^{o}C and G=700 Wm^{-2}	***At T=5^{o}C and G=1300 Wm^{-2}***
Voltage range at Pmax	0.806kVx 0.8=0.6448	0.891 kV/0.8→1.113
Current range at Pmax	0.218kA	0.384 kA
Maximum power range	0.176MW	0.341MW
Boost Converter Design		
Switching frequency	3kHz	
Duty cycle range	Dmin=0.0725, Dmax=0.462, Drated=0.3	
Minimum Required Input Inductance (L_{in})	2.4mH	
Selected L_{in}	2.5mH	

In renewable energy applications like PV systems, a properly sized output capacitor (DC-bus capacitor) is essential for maintaining a stable DC voltage, smoothing out voltage fluctuations, and providing energy during transient conditions. The design of the output capacitor must consider the hold-up time, which is the period the capacitor can supply energy to the load when input power is temporarily unavailable. This is crucial in renewable energy systems with intermittent power supply.

The required capacitance for the hold-up time can be calculated based on the energy needed during this period. The energy stored in a capacitor is given by:

$$\frac{1}{2}.C_{out}.V_{Out}^2 \geq \frac{P_{o_{rated}}}{\eta}.T_h \tag{5.7}$$

where C_{out} the total dc-link capacitance, and T_h is the hold-up time. Th is typically selected to be around one fundamental period. So Cout can be selected as $C_{out} \geq 5875\ \mu F$

There are several methods to implement control algorithms for extracting maximum power from a solar panel using a boost converter. A single controller or a dual controller can be used to regulate the boost converter [92]. In this solar plant, a dual control loop is implemented as illustrated Figure 5.3. The PV array voltage reference is provided by the MPPT component available in PSCAD/EMTDC with perturb and observe algorithm to track the maximum power output. To maintain MPP at PV panel terminals to harness the maximum power from the PV panels.

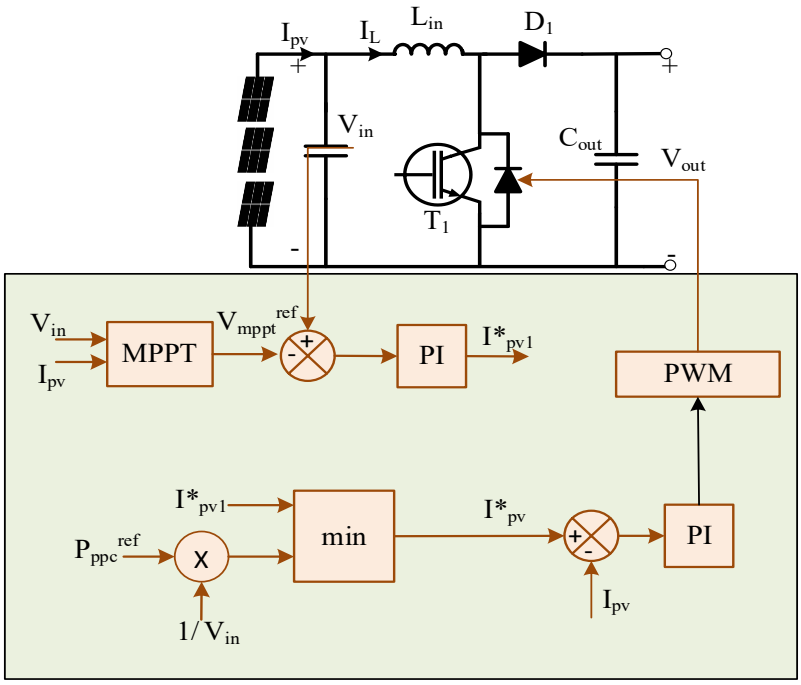

Figure 5.3 Dual controller for boost converter.

5.2.2 Power Plant Controller

When a PPC is integrated with a solar PV power plant, it typically provides a reference for the power output. The system operates based on the minimum of the PPC reference and the MPPT command. If power frequency control is incorporated into the power plant, the PPC reference adjusts according to the droop setting. Alternatively, frequency control can be added to the power order after the PPC.

However, frequency control in solar plants has limitations. If the available power is less than the PPC's requested power, the system cannot fully address the grid's power frequency issue. Conversely, if the available power exceeds the requested power, the system can supply the requested power. The control algorithm used to implement power frequency control through the PPC is illustrated in Figure 5.4.

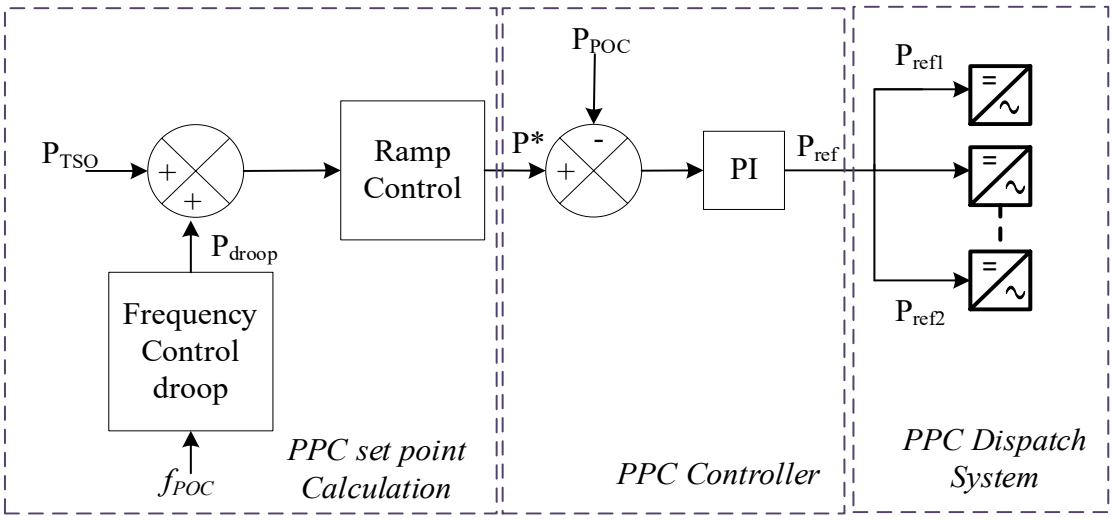

Figure 5.4 Active power reference calculation using PPC

Power frequency control is realized through a droop curve, as shown in Figure 5.5. The key parameters for frequency-droop operation are outlined in Table 5.2 [41].

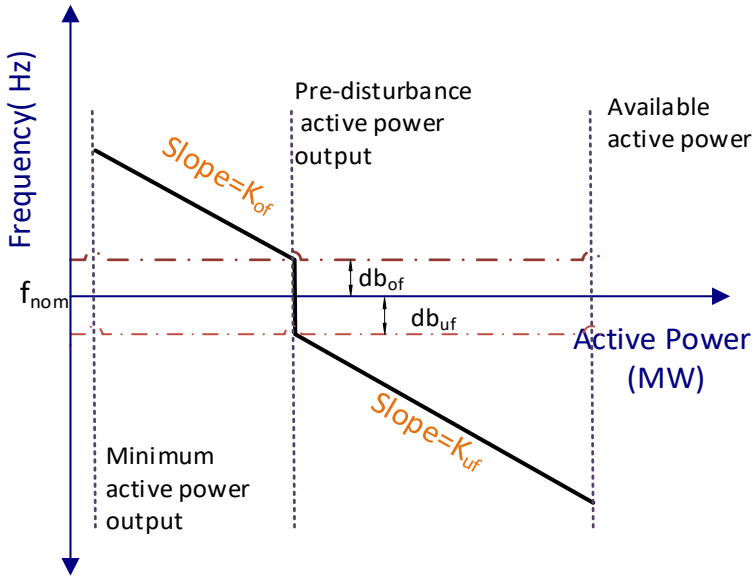

Figure 5.5 Primary Frequency Response (PFR) of an IBR

Table 5.2 Parameters of frequency-droop (frequency-power) operation [41]

Parameter	Default Setting
db_{OF}, db_{UF} (Hz)	0.06% of f_{rom} (0.036Hz (for 60Hz))
kOF,kUF	5%

The droop relationship is defined by the equation:

$$Droop\ (\%) = \ 100.\frac{\Delta F/F_{nom}}{\Delta P/P_{MAX}} \tag{5.8}$$

A typical droop setting of 5% implies that if the frequency error is 5% (e.g., 3 Hz for a 60 Hz system), the power plant attempts to utilize its full output to counteract the frequency deviation.

Incorporating power frequency control in inverters can lead to unintended outcomes if a false high-frequency signal is detected. In such cases, the controller may erroneously reduce active power injections, which could hinder the system's recovery during a fault. For effective grid support, active power should increase after a fault is cleared [14], [93].

Reactive power (Q_{ref}) can be provided as a set value Q_{set}, or Q can be calculated to maintain voltage at the PCC or a specific power factor. The user can select between these control modes, with the PPC assigning the Q_{ref} command to each inverter. The used controller to give the Q_{ref} is shown in Figure 5.6.

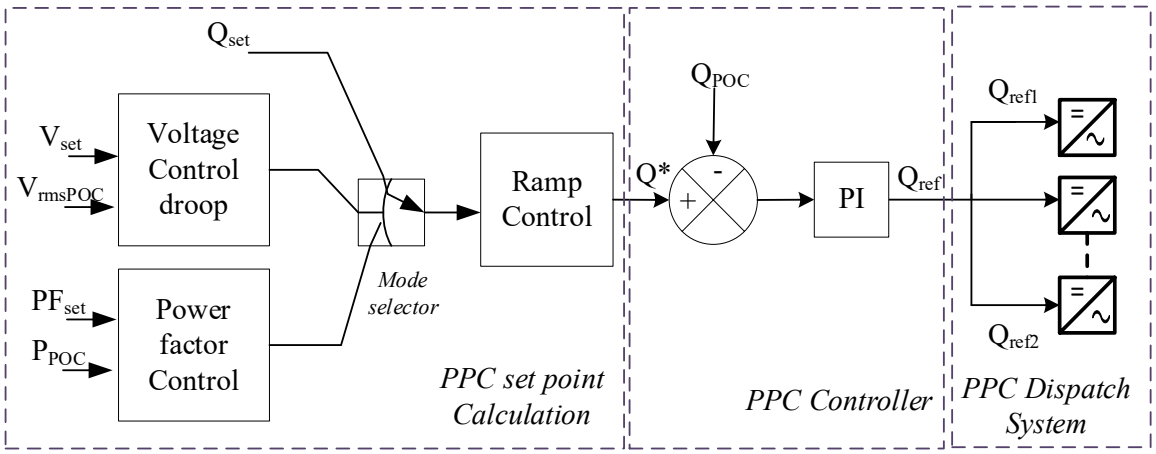

Figure 5.6 Reactive power reference calculation using PPC

5.2.3 Simulation Results

Using Transient eliminator to freeze the frequency with SRF -PLL.

The validation process involved comparing the performance of the transient eliminator with the SRF-PLL in a solar power plant. An A-B to Ground fault was applied at 3.0 seconds, and the system recovered by 3.2 seconds. The results, as shown in Figure 5.7, highlight the variation in power output with and without the use of the transient eliminator to freeze the frequency.

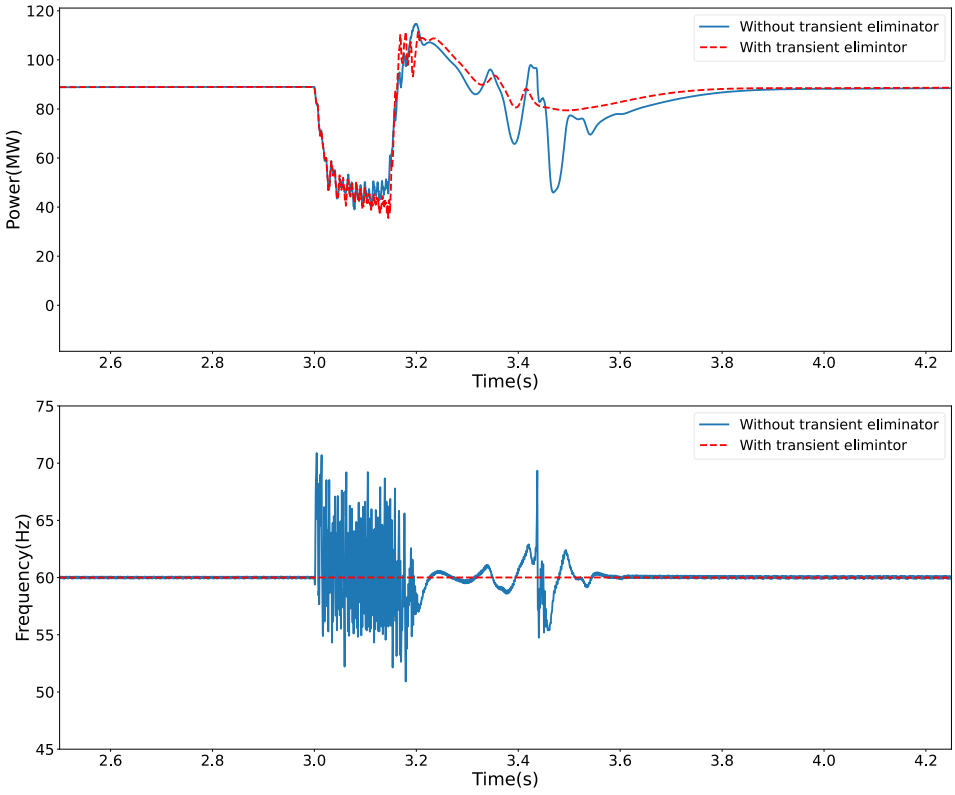

Figure 5.7 Impact of Frequency Freezing on Power Output Stability using SRF-PLL

The following observations were made:

- Without the transient eliminator, erroneous frequency detection caused a reduction in the power reference after fault clearance, leading to a decrease in power output.
- With the transient eliminator freezing the frequency during the fault (for 0.3 seconds), the power output improved, aiding recovery after the fault.

Using Transient eliminator freeze the frequency with DSOGI -PLL

The same validation process was conducted using DSOGI-PLL. In this case, fault impedance is reduced because the DSOGI-PLL does not exhibit as severe a response to erroneous frequency detection as the SRF-PLL.

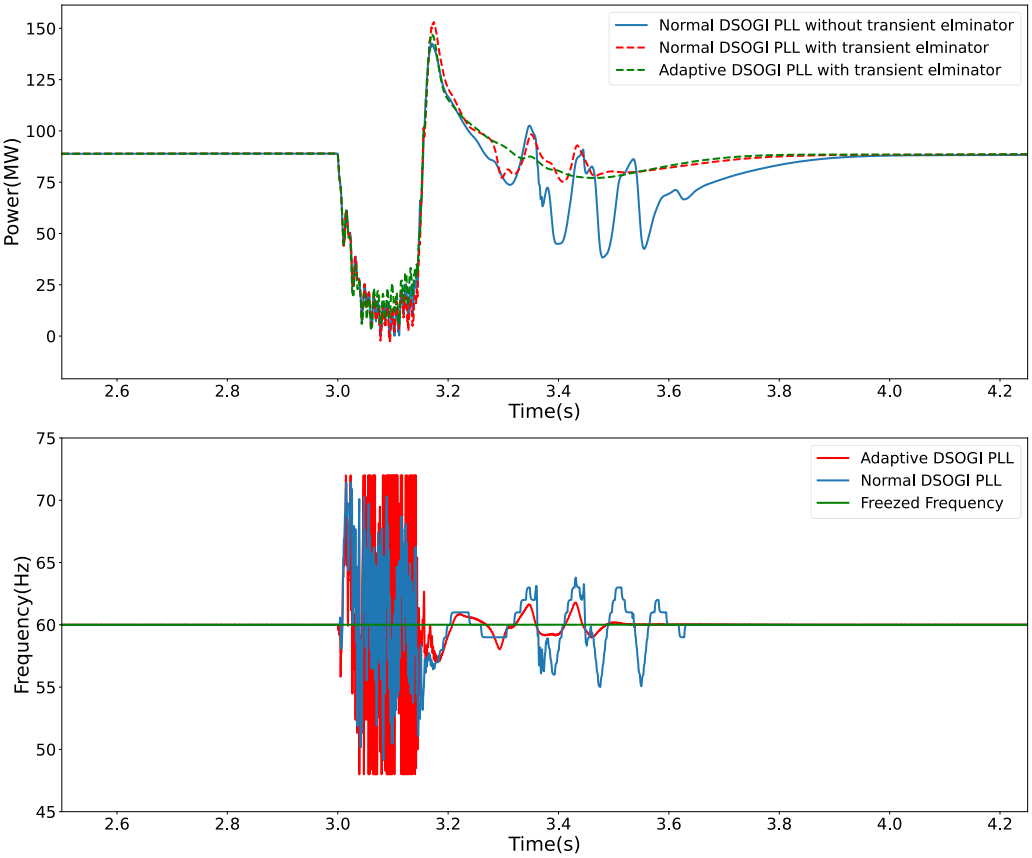

Figure 5.8 Impact of Frequency Freezing on Power Output Stability using DSOGI-PLL

In this study, the transient eliminator was applied to both the standard DSOGI-PLL and the adaptive DSOGI-PLL. It effectively prevented erroneous frequency detection, demonstrating that transient eliminator plays a crucial role in enhancing power frequency control. Furthermore, incorporating the adaptive bandwidth mechanism did not compromise performance and even showed slight improvements over the standard DSOGI-PLL.

The validation highlights the critical role of transient eliminators in freezing frequency during faults to maintain stable power output. Erroneous frequency detection can lead to reduced power output, negatively affecting system recovery. By employing a transient

eliminator, the system can sustain its power reference during and after faults, ensuring effective grid support and improving overall reliability.

5.3 Modified IEEE 9-Bus System with an Installed Solar Plant

The performance of the proposed DSOGI-PLL is now evaluated using a modified version of the IEEE 9-bus test system with an installed solar power plant for several scenarios. The schematic diagram of the simulation test system is shown in Figure 5.9. A 125MW rated solar power plant is connected to the bus 3 via a step-up transformer. The Short-Circuit Ratio (SCR) of the PV system used is close to 1.8. The synchronous generators G1 and G2 are modeled as a hydro-power plant with a capacity of 100MVA and 200 MVA. Thus, this system includes dynamics of the synchronous generators, in comparison to the system equivalent considered in Section 5.2. The system was simulated in PSCAD/EMTDC with 5 μs simulation time step.

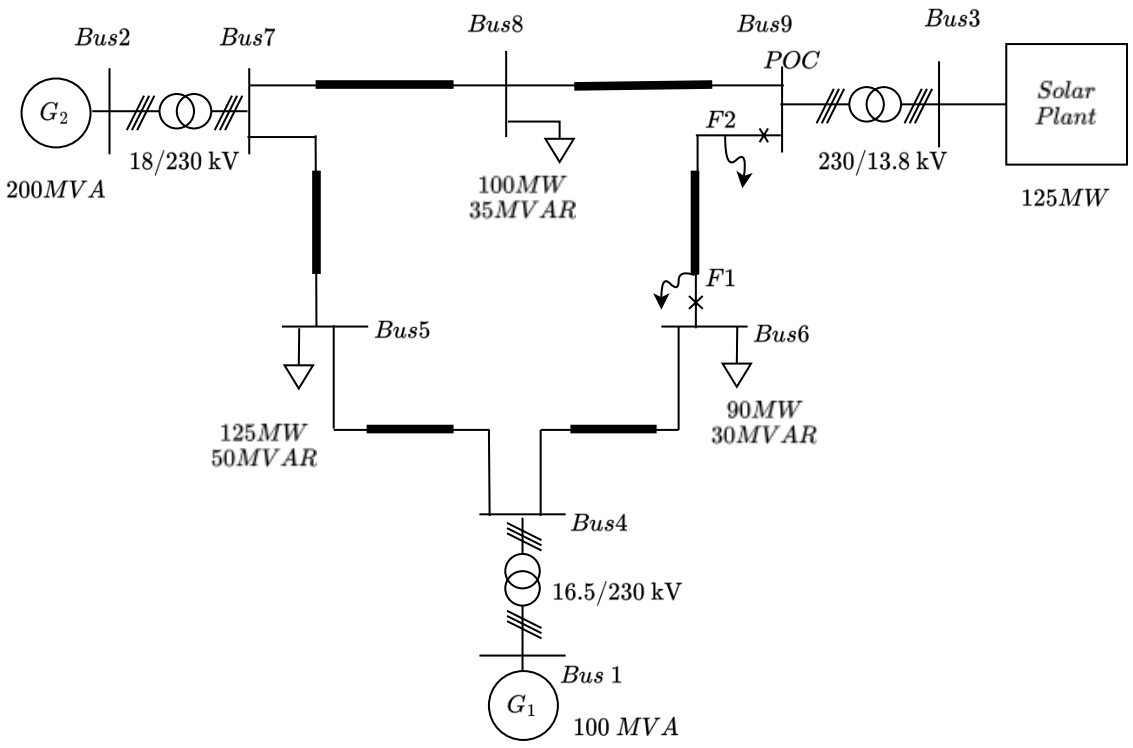

Figure 5.9: Modified IEEE 9-bus system with an installed solar plant.

5.3.1 Grid-Side Converter

Figure 5.10 shows the decoupled control of the grid side converter. Here the converter is maintaining the Vdc at a constant value and maintain the reactive power according to the PPC control command.

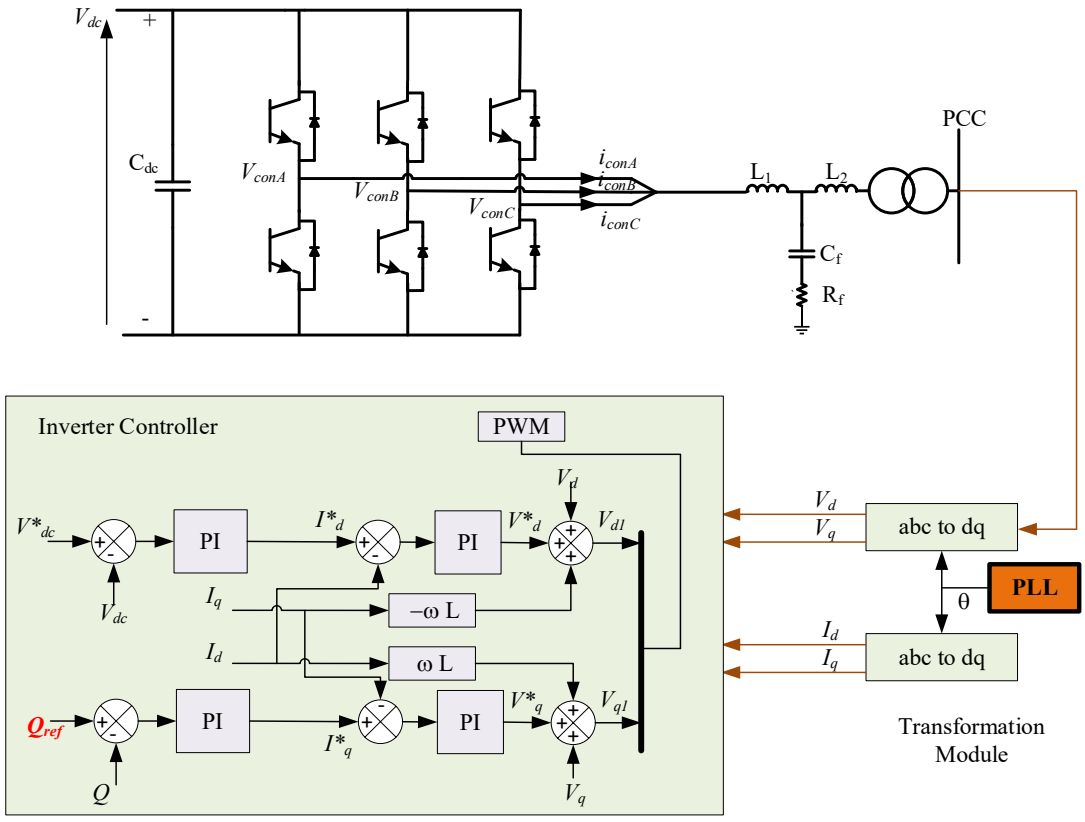

Figure 5.10 Decoupled control of grid side converter

The harmonic currents injected by a grid-connected inverter can be classified into three categories: low frequency harmonics, switching frequency harmonics, and high frequency harmonics. Each category of harmonic currents must be sufficiently and appropriately attenuated to ensure optimal performance and minimize potential issues [94], [95]. An LCL filter is typically used at the inverter output due to its several advantages. It can operate effectively at low switching frequencies, offers benefits in filter dimensions compared to conventional "L" and "LC" filters, and has a lower voltage drop while providing better damping than traditional "L" and "LC" filters [96]. The system and LCL filter parameters are shown in Table 5.3.

Table 5.3 System and LCL Filter Design Parameters

System Parameters.	LCL Filter parameters.
V_{dc} = 1.2 kV	L_1 = 0.4mH
V_{ac} = 0.65kV	L_2 = 0.4mH
Prated = 0.25MW	C_f = 39.23 μF
Irated = 0.22kA	R_f = 10.68 Ω
f_{sw} = 3kHz (switching frequency)	

5.3.2 Simulation Results

The impact of an unbalanced fault on the modified IEEE 9-bus system with a solar plant connection is illustrated in Figure 5.11. An A-C-G fault is applied at 3.5 seconds and cleared at 3.66 seconds at location 'F1', near Bus 6, as shown in Figure 5.9. During this disturbance, the Adaptive DSOGI-PLL with three times bandwidth enhancements demonstrates improved performance compared to the conventional DSOGI-PLL. Specifically, it exhibits reduced overshoot in both phase error and power response, and the system's power output settles more quickly with the adaptive PLL. While the voltage response remains nearly identical for both configurations, notable differences are observed in the frequency output. The conventional DSOGI-PLL and the raw frequency output of the adaptive DSOGI-PLL show oscillations during the fault period. In contrast, the frozen frequency output of the adaptive DSOGI-PLL remains constant throughout the

disturbance, effectively preventing erroneous frequency measurements and enhancing system stability.

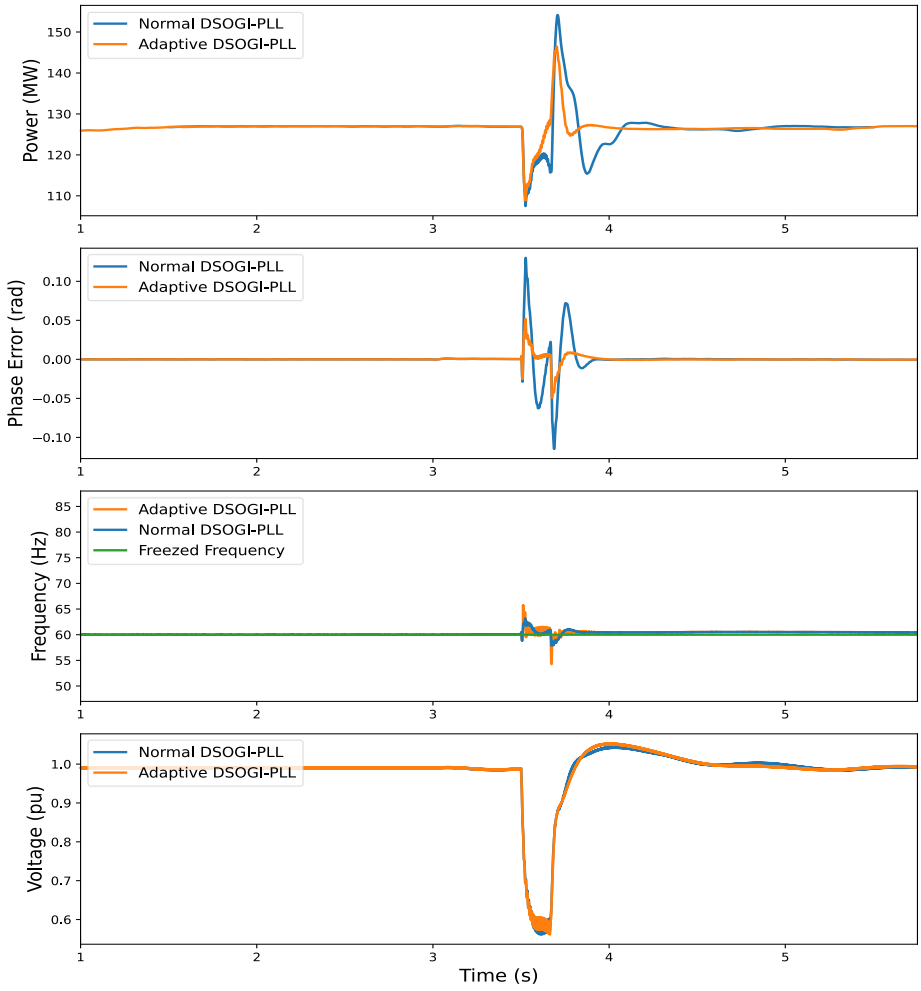

Figure 5.11 Comparison of PV plant control performance with proposed DSOGI PLL and the conventional under an unbalanced fault

The impact of a balanced fault on the modified IEEE9 solar plant-connected system is presented in Figure 5.12 A three-phase-to-ground fault is applied at fault location 'F2', as shown in Figure 5.9 , at 1.5 seconds. To clear the fault, both breakers on the affected transmission line are opened at 1.66 seconds.

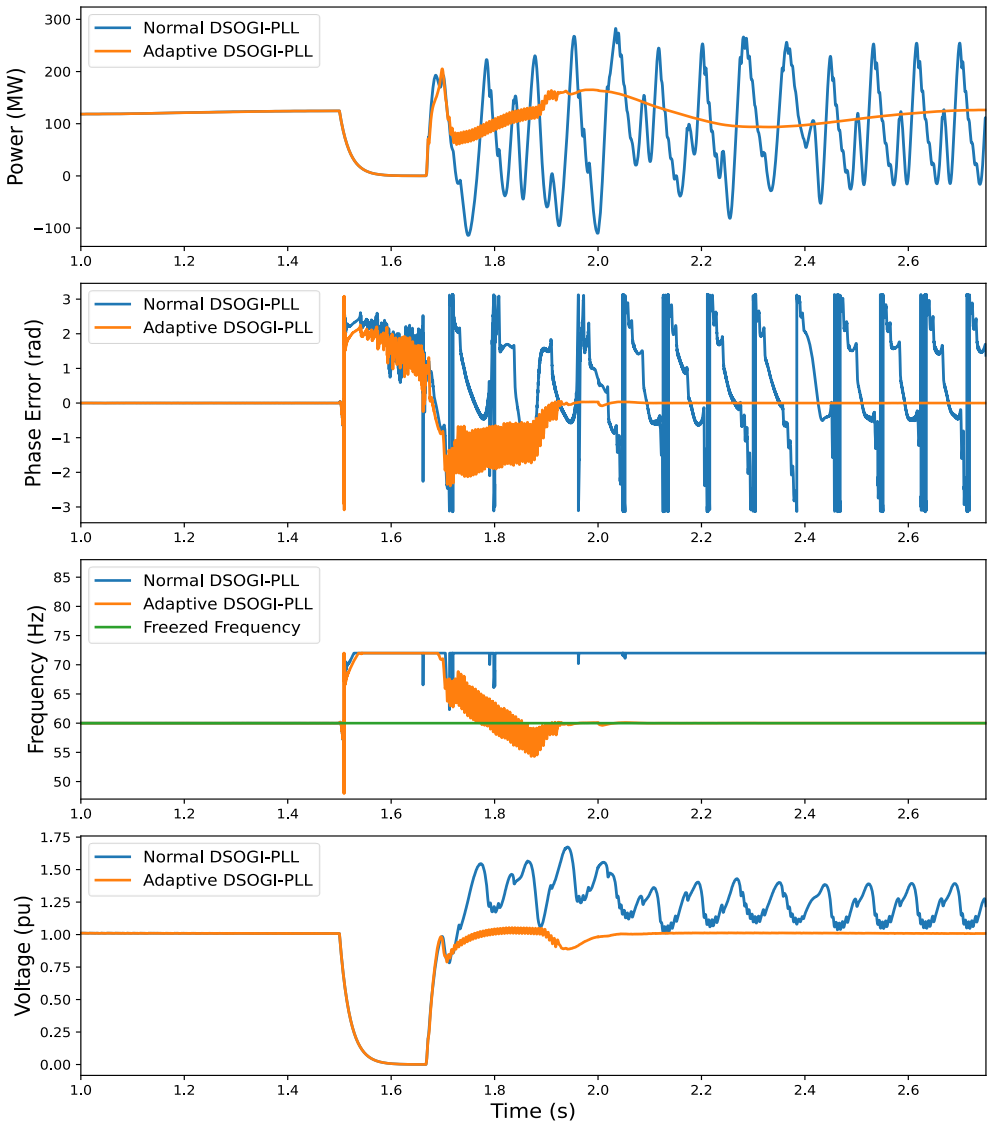

Figure 5.12 Comparison of PV plant control performance with proposed DSOGI PLL and the conventional under a balanced fault condition

In the case where the standard DSOGI-PLL is employed, the system experiences instability after removing Line 9-6 to clear a fault. This instability is not confined to a single parameter but is clearly reflected across all major system responses. Active power, phase error and voltage exhibit significant oscillations, and while the frequency deviates drastically, eventually reaching the upper limit of 1.2 pu (72 Hz) set within the DSOGI-PLL. This

instability is due to transient variations and delayed tracking of the phase angle at the point of interconnection, which adversely affects the control system that uses the phase angel for dq transformation. Contrastingly, with the adaptive DSOGI-PLL with bandwidth enhancement of three times , the phase angle is promptly tracked after the fault is cleared. Despite some initial overshoots in power, the system stabilizes approximately within 0.5s after clearing the fault. The system stability under the normal DSOGI PLL is observed to be maintained down to a minimum SCR of 2.3 for the event. Beyond this threshold, a decrease in SCR results in system instability. But with the use of the proposed PLL the SCR can be reduced even further, down to 1.0. This outcome highlights the effectiveness of the proposed modifications in ensuring swift and accurate phase detection, ultimately contributing to the stability and resilience of the system, specially in post-fault scenarios. Furthermore, this modified PLL is tested under different fault scenarios including balanced and unbalanced faults and it is well performing compared to the standard DSOGI-PLL

5.4 Power Reserve control

After validating the performance of the modified DSOGI-PLL, a power reserve controller was incorporated into the solar plant. The master-slave approach, known for its simplicity, was used to manage the power reserve. Figure 5.13 shows the modified system.

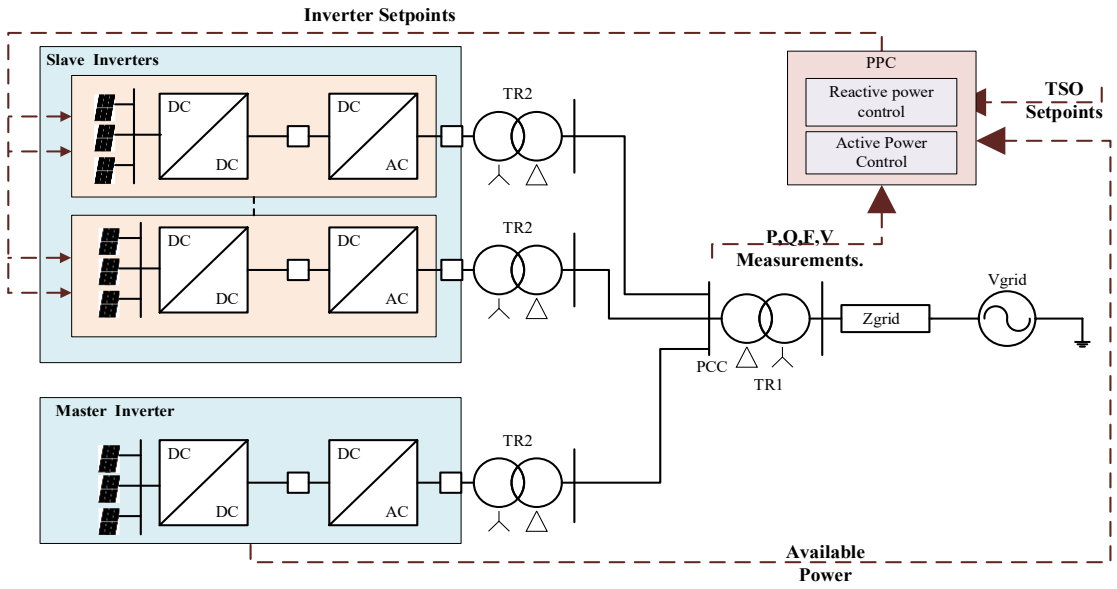

Figure 5.13 Solar plant connected system with power reserve control.

In the master-slave approach, a selected inverter or set of inverters functions as the master, tracking the MPPT to determine the optimal power output based on solar irradiance. This MPPT value is then communicated to the PPC, which manages power reserves and performs frequency control. The PPC adjusts the MPPT output based on system requirements, reserving a fraction of the power as needed. For instance, if 90% of the MPPT value is required, the PPC scales the power output to 0.9 of the MPPT. It then calculates the minimum between the TSO setpoint and the reserved MPPT value. This minimum value serves as the reference for power-frequency control, enabling the solar plant to regulate active power output effectively in response to grid frequency deviations. Once the PPC establishes the active power order, it distributes the command to all slave inverters, ensuring synchronized and coordinated power output across the plant. Figure 5.14 shows this control system.

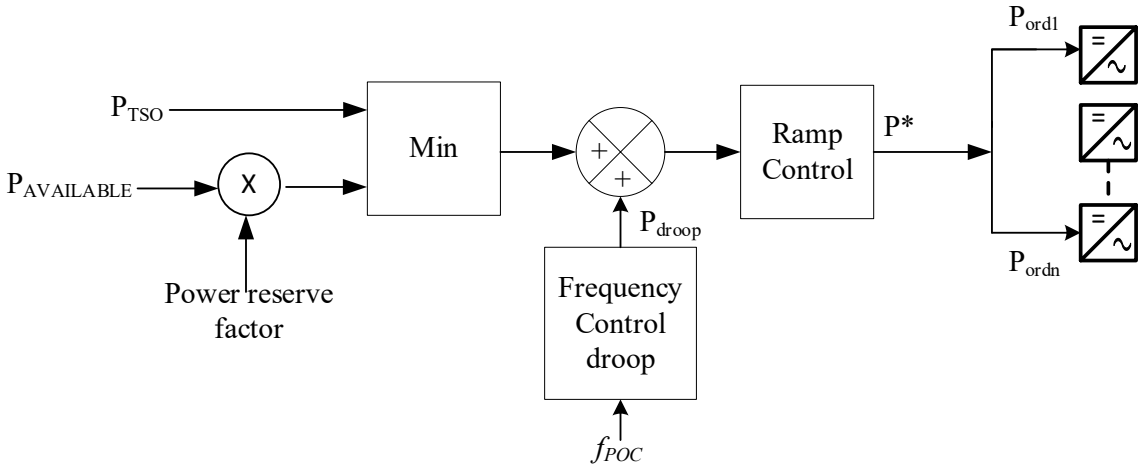

Figure 5.14 Power reference calculation using PPC incorporating power reserve.

Power-frequency control is most effective when adjustments are made directly to the available power output of the solar plant rather than modifying thet TSO command (P_{TSO}). Due to the intermittent nature of solar power, relying solely on TSO commands can be impractical. Maintaining awareness of the available power at all times allows the system to allocate reserves consistently, irrespective of solar variability. This approach ensures that the inverter actively supports the system's primary frequency response, enhancing grid stability and reliability even under fluctuating power conditions. By aligning available power with grid requirements, this method provides a robust mechanism to mitigate the challenges posed by solar intermittency.

5.4.1 Simulation Results

The modified IEEE-9 bus system, integrated with a solar plant equipped with power reserve control, is utilized to evaluate the proposed power reserve control mechanism. A

load of 30 MW is added to the system at 6 seconds from Bus 8 as illustrated in Figure 5.15.

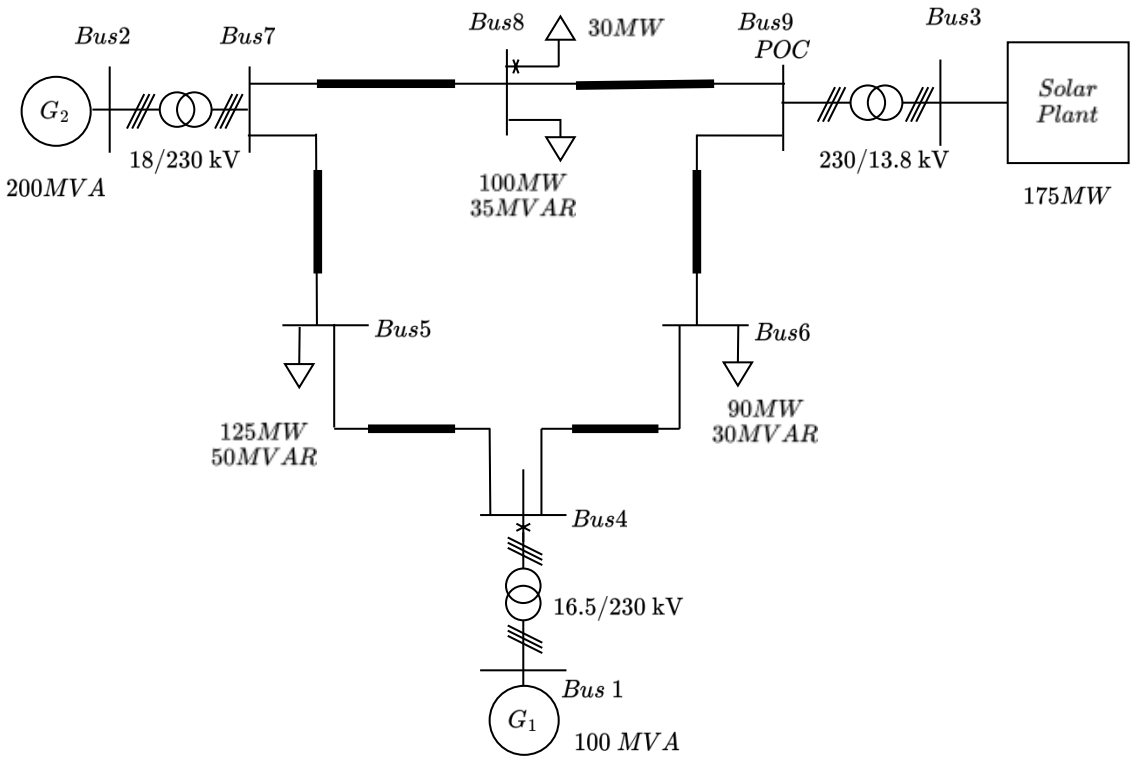

Figure 5.15 modified IEEE-9 bus system with power reserve in solar plant

Two different droop settings—1% and 5%—with a power reserve of 0.1 of the available power are analyzed. The frequency responses of these settings are compared against a scenario without any power reserve, as illustrated in Figure 5.16. Both droop settings provided effective primary frequency responses, stabilizing the grid during frequency deviations. However, the 1% droop setting demonstrated a slight improvement over the 5% droop due to its higher power output rate, enabling a faster response to frequency changes. Since only the primary frequency response is considered, the system settles at a lower

frequency without returning to nominal. This results in a slightly reduced steady-state power output, as dictated by the droop characteristic at the new frequency.

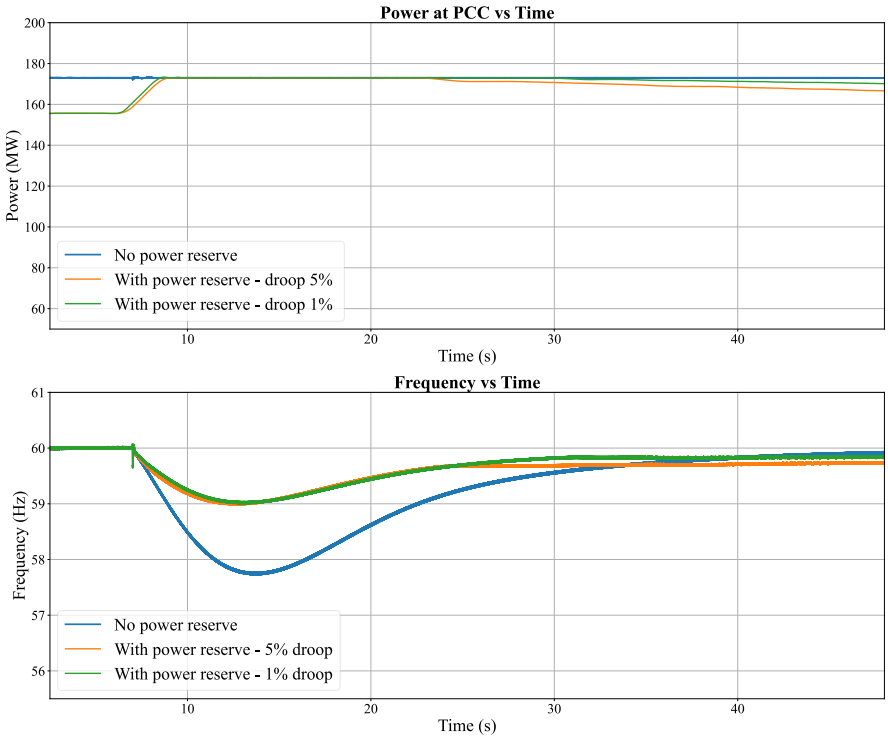

Figure 5.16 Primary frequency response with and without power reserve

The results demonstrate that incorporating power reserve, allowing the frequency droop curve to operate on both sides, significantly enhances the primary frequency response of the overall system.

Further, this power reserve control was used to study the impact of changes in irradiation levels on system performance. When irradiation decreases, the available power from the PV plant also drops. In such cases, if the plant maintains a reserve, the primary frequency response improves. Specifically, when power drops due to reduced irradiation, the frequency also declines, and the plant operates at full capacity to support frequency

recovery. Once the frequency stabilizes, the plant restores the reserve from the available power, as illustrated in the Figure 5.17.

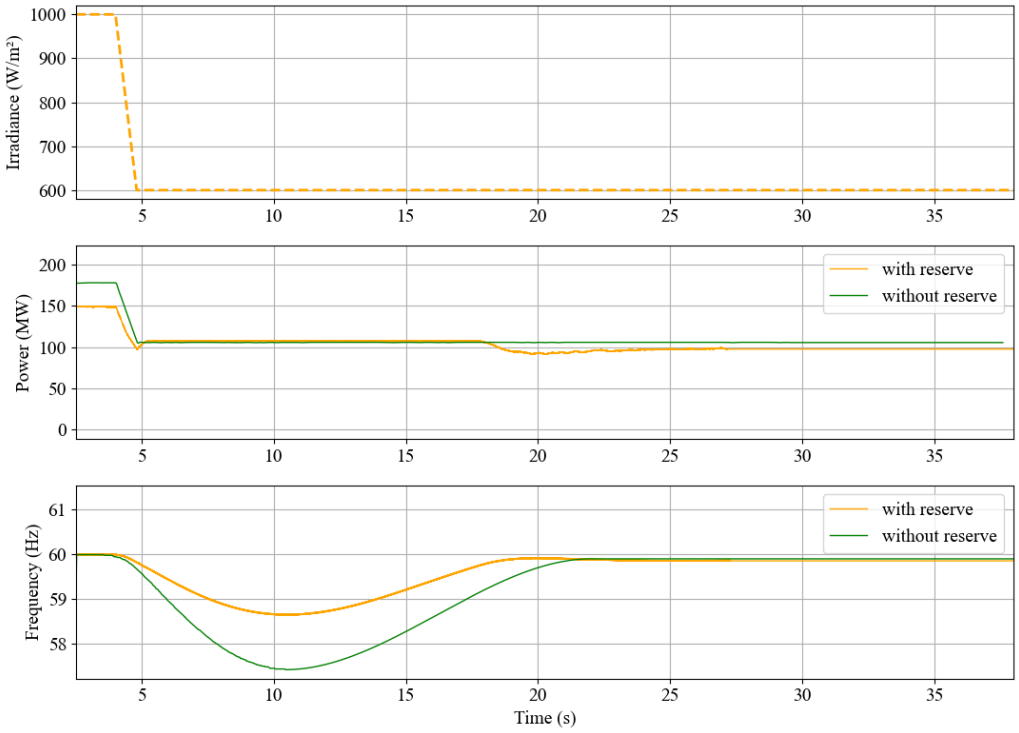

Figure 5.17 Primary frequency response with and without power reserve under an irradiation change

To accurately capture real world scenarios such as variations in irradiation and temperature, it is essential to implement detailed solar PV module models as discussed in Chapter 3 rather than relying on a simple DC source to mimic PV functionality.

5.5 Summary

This chapter evaluated the proposed DSOGI- PLL modifications under various test scenarios, demonstrating improvements in accuracy, dynamic response, and robustness. It examined the integration of PLLs into grid-connected solar PV systems, confirming their role in stabilizing power output under dynamic conditions. Furthermore, the

implementation of a Power Reserve Controller using the Master-Slave approach optimized frequency regulation and enhanced primary frequency response, addressing challenges caused by disturbances. Overall, the proposed enhancements significantly improved system stability and reliability.

Chapter 6

Conclusions and Future Work

6.1 Summary and Conclusions

This thesis addresses key challenges in integrating PV systems into modern power grids, with a dual focus on enhancing PV module modeling and improving grid stability during transient events.

In Chapter 3, a robust methodology was introduced for extracting parameters of the SDM for monofacial PV modules using only the electrical data typically available in manufacturer datasheets. This approach eliminates the need for extensive experimental data or complex optimization techniques. The accuracy of the method was confirmed by comparing simulated I-V curves with those extracted from datasheets using a curve extraction tool. The model also accounts for variations in temperature and irradiance, demonstrating its robustness and reliability. The same methodology was extended to bifacial PV modules by incorporating bifacial gain and partial shading effects. Validation was performed through comparisons with manufacturer data and experimental results from published literature, confirming the method's accuracy and applicability for bifacial PV modeling

Chapters 4 and 5 focused on enhancing the performance of the DSOGI-PLL used in grid-connected converter systems. Key modifications included the integration of a transient eliminator and an adaptive bandwidth scheme to the DSOGI-PLL. The transient eliminator

effectively identifies and responds to grid disturbances by freezing the PLL frequency temporary for a predetermine time, thereby reducing overshoot during phase jumps and fault conditions. The adaptive bandwidth mechanism dynamically increases the cutoff frequency of the DSOGI-PLL during disturbances, enabling faster synchronization with the grid voltage and thereby enhancing overall system stability. Simulation results validate the effectiveness of these enhancements, showing improvements in synchronization accuracy, reduced phase error, and better adaptability during transient events. Furthermore, a power reserve controller was implemented using the master-slave approach for enhancing frequency regulation and primary frequency response. The simulation results confirmed that this power reserve controller can support power frequency response during disturbances.

In conclusion, the methodologies developed in this thesis contribute to more accurate PV module modeling and more resilient grid synchronization strategies, supporting the reliable integration of renewable energy sources into modern power systems.

6.2 Contributions

Advancements in PV Module Modeling

- Validated a robust parameter extraction method for monofacial and bifacial PV modules using limited manufacturer data.
- Included partial shading effects in the modeling of bifacial PV modules to improve prediction accuracy in real-world conditions
- Validated the bifacial model using experimental data from published data, establishing their reliability for diverse environmental conditions.

Enhancement of Grid Stability

- Proposed and validated a modified DSOGI-PLL incorporating adaptive bandwidth and transient detection algorithms to improve performance under dynamic conditions.
- Conducted extensive simulations using diverse test cases, including a test waveform generator, a solar plant connected to a grid modeled as a voltage source behind an impedance, and an IEEE 9-bus system, to assess the robustness of the proposed methodologies.
- These test results showed that when using the conventional DSOGI-PLL, the modified IEEE-9 bus system could maintain synchronism during severe faults for PV plants with SCR values approaching 2.0. However, with the proposed modifications, the system could accommodate PV plants with SCR value approaching 1.0, demonstrating improved robustness under weak grid conditions.
- Demonstrated how primary frequency response can be enhanced using power reserve control for solar inverters, contributing to improved grid stability.

These contributions have led to the following publications;:

- **G. Ranasinghe** and A. Rajapakse, "Enhanced Single Diode Model for Bifacial PV Module Incorporating Partial Shading," *2023 International Conference on Sustainable Technology and Engineering (i-COSTE)*, Nadi, Fiji, 2023, pp. 1-6
- Rajapakse, **G. Ranasinghe**, R. Jayasinghe, L. Kotalawala and D. Muthumini, "Robust Method for Estimating Single-Diode Model Parameters of a PV Module

from the Manufacturer's Datasheet Information," *2023 International Conference on Sustainable Technology and Engineering (i-COSTE)*, Nadi, Fiji, 2023, pp. 1-6

- **G. Ranasinghe**, A. D. Rajapakse and L. Kotalawala, "Advanced DSOGI PLL with Adaptive Bandwidth for Improved Transient Performance of Grid Connected Inverter Control Systems," *2024 IEEE Power & Energy Society General Meeting (PESGM)*, Seattle, WA, USA, 2024, pp. 1-5.

6.3 Future Work

- Validate the bifacial PV module model using experimental data from laboratory setups to ensure its practical applicability and accuracy under real-world conditions.
- Integrate the proposed PLL modifications into larger systems with higher levels of renewable energy generation to evaluate their scalability and performance.
- The reliability of the proposed master–slave approach for power reserve control has limitations, as the failure of a single master could lead to system-wide issues. This approach was implemented primarily to demonstrate how maintaining a reserve improves primary frequency response. For a more robust solution, future work can explore distributed and fault-tolerant control strategies.

References

[1] A. I. Osman *et al.*, "Cost, environmental impact, and resilience of renewable energy under a changing climate: a review," *Environ Chem Lett*, vol. 21, no. 2, 2023, doi: 10.1007/s10311-022-01532-8.

[2] F. Johnsson, J. Kjärstad, and J. Rootzén, "The threat to climate change mitigation posed by the abundance of fossil fuels," *Climate Policy*, vol. 19, no. 2, 2019, doi: 10.1080/14693062.2018.1483885.

[3] H. M. Ridha, H. Hizam, S. Mirjalili, M. L. Othman, M. E. Ya'acob, and L. Abualigah, "A Novel Theoretical and Practical Methodology for Extracting the Parameters of the Single and Double Diode Photovoltaic Models," *IEEE Access*, vol. 10, 2022, doi: 10.1109/ACCESS.2022.3142779.

[4] J. Z. Zhou, H. Ding, S. Fan, Y. Zhang, and A. M. Gole, "Impact of short-circuit ratio and phase-locked-loop parameters on the small-signal behavior? of a VSC-HVDC converter," *IEEE Transactions on Power Delivery*, vol. 29, no. 5, pp. 2287–2296, Oct. 2014, doi: 10.1109/TPWRD.2014.2330518.

[5] "NERC | Report Title | Report Date I Reliability Guideline," 2018.

[6] V. Prakash, R. Bhakar, H. P. Tiwari, H. W. Pain, Y. Bian, and F. Li, "Primary frequency response in future low carbon scenario: Opportunities & challenges," in *2016 International Conference on Recent Advances and Innovations in Engineering, ICRAIE 2016*, 2016. doi: 10.1109/ICRAIE.2016.7939502.

[7] Y. Liu, S. You, J. Tan, Y. Zhang, and Y. Liu, "Frequency Response Assessment and Enhancement of the U.S. Power Grids Toward Extra-High Photovoltaic Generation Penetrations-An Industry Perspective," *IEEE Transactions on Power Systems*, vol. 33, no. 3, 2018, doi: 10.1109/TPWRS.2018.2799744.

[8] D. B. Rathnayake *et al.*, "Grid Forming Inverter Modeling, Control, and Applications," *IEEE Access*, vol. 9, 2021, doi: 10.1109/ACCESS.2021.3104617.

[9] D. Yousri, H. Rezk, and A. Fathy, "Identifying the parameters of different configurations of photovoltaic models based on recent artificial ecosystem-based optimization approach," *Int J Energy Res*, vol. 44, no. 14, 2020, doi: 10.1002/er.5747.

[10] M. Zagrouba, A. Sellami, M. Bouaïcha, and M. Ksouri, "Identification of PV solar cells and modules parameters using the genetic algorithms: Application to maximum power extraction," *Solar Energy*, vol. 84, no. 5, 2010, doi: 10.1016/j.solener.2010.02.012.

[11] A. Askarzadeh and A. Rezazadeh, "Extraction of maximum power point in solar cells using bird mating optimizer-based parameters identification approach," *Solar Energy*, vol. 90, 2013, doi: 10.1016/j.solener.2013.01.010.

[12] R. Kopecek and J. Libal, "Bifacial photovoltaics 2021: Status, opportunities and challenges," 2021. doi: 10.3390/en14082076.

[13] "NERC | Report Title | Report Date I 1,200 MW Fault Induced Solar Photovoltaic Resource Interruption Disturbance Report," 2017.

[14] NERC, “Reliability Guideline: BPS-Connected Inverter-Based Resource Performance,” 2018.

[15] “RELIABILITY | RESILIENCE | SECURITY NERC | Report Title | Report Date I 2022 Odessa Disturbance.”

[16] Q. Hu, L. Fu, F. Ma, and F. Ji, “Large Signal Synchronizing Instability of PLL-Based VSC Connected to Weak AC Grid,” *IEEE Transactions on Power Systems*, vol. 34, no. 4, 2019, doi: 10.1109/TPWRS.2019.2892224.

[17] D. Zhu, S. Zhou, X. Zou, and Y. Kang, “Improved Design of PLL Controller for LCL-Type Grid-Connected Converter in Weak Grid,” *IEEE Trans Power Electron*, vol. 35, no. 5, 2020, doi: 10.1109/TPEL.2019.2943634.

[18] F. D. Freijedo *et al.*, “Grid-synchronization methods for power converters,” in *IECON Proceedings (Industrial Electronics Conference)*, 2009. doi: 10.1109/IECON.2009.5414976.

[19] S. Golestan, J. M. Guerrero, and J. C. Vasquez, “Three-Phase PLLs: A Review of Recent Advances,” 2017. doi: 10.1109/TPEL.2016.2565642.

[20] J. Lopez-Garcia, A. Casado, and T. Sample, “Electrical performance of bifacial silicon PV modules under different indoor mounting configurations affecting the rear reflected irradiance,” *Solar Energy*, vol. 177, 2019, doi: 10.1016/j.solener.2018.11.051.

[21] A. Yahya-Khotbehsara and A. Shahhoseini, “A fast modeling of the double-diode model for PV modules using combined analytical and numerical approach,” *Solar Energy*, vol. 162, 2018, doi: 10.1016/j.solener.2018.01.047.

[22] S. R. Fahim, H. M. Hasanien, R. A. Turky, S. H. E. A. Aleem, and M. Ćalasan, “A Comprehensive Review of Photovoltaic Modules Models and Algorithms Used in Parameter Extraction,” 2022. doi: 10.3390/en15238941.

[23] T. Ahmad, S. Sobhan, and Md. F. Nayan, “Comparative Analysis between Single Diode and Double Diode Model of PV Cell: Concentrate Different Parameters Effect on Its Efficiency,” *Journal of Power and Energy Engineering*, vol. 04, no. 03, 2016, doi: 10.4236/jpee.2016.43004.

[24] C. Bhowmik, S. Bhowmik, and A. Ray, “Green Energy Sources Selection for Sustainable Planning: A Case Study,” *IEEE Trans Eng Manag*, vol. 69, no. 4, 2022, doi: 10.1109/TEM.2020.2983095.

[25] T. S. Liang, M. Pravettoni, J. P. Singh, and Y. S. Khoo, “Meeting the requirements of IEC TS 60904-1-2 for single light source bifacial photovoltaic characterisation: Evaluation of different back panel materials,” *Engineering Research Express*, vol. 2, no. 1, 2020, doi: 10.1088/2631-8695/ab7ee5.

[26] B. G. Bhang, W. Lee, G. G. Kim, J. H. Choi, S. Y. Park, and H. K. Ahn, “Power Performance of Bifacial c-Si PV Modules with Different Shading Ratios,” *IEEE J Photovolt*, vol. 9, no. 5, 2019, doi: 10.1109/JPHOTOV.2019.2928461.

[27] J. Johnson, D. Yoon, and Y. Baghzouz, “Modeling and analysis of a bifacial grid-connected photovoltaic system,” in *IEEE Power and Energy Society General Meeting*, 2012. doi: 10.1109/PESGM.2012.6345266.

[28] D. Hong, J. Ma, K. L. Man, H. Wen, and P. Wong, “Prediction of I-V characteristics for Bifacial PV Modules via an alpha-beta single double-diode model,” in *2022*

IEEE Energy Conversion Congress and Exposition, ECCE 2022, 2022. doi: 10.1109/ECCE50734.2022.9948042.

[29] A. K. Abdulrazzaq, G. Bognár, and B. Plesz, "Evaluation of different methods for solar cells/modules parameters extraction," *Solar Energy*, vol. 196, 2020, doi: 10.1016/j.solener.2019.12.010.

[30] H. M. Waly, H. Z. Azazi, D. S. M. Osheba, and A. E. El-Sabbe, "Parameters extraction of photovoltaic sources based on experimental data," *IET Renewable Power Generation*, vol. 13, no. 9, 2019, doi: 10.1049/iet-rpg.2018.5418.

[31] L. E. Peñaranda Chenche, O. S. Hernandez Mendoza, and E. P. Bandarra Filho, "Comparison of four methods for parameter estimation of mono- and multi-junction photovoltaic devices using experimental data," 2018. doi: 10.1016/j.rser.2017.06.089.

[32] R. TAMRAKAR and A. GUPTA, "A Review extraction of solar cell modelling parameters," *IJIREEICE*, 2015, doi: 10.17148/ijireeice.2015.3111.

[33] J. Cubas, S. Pindado, and C. De Manuel, "Explicit expressions for solar panel equivalent circuit parameters based on analytical formulation and the lambert W-function," *Energies (Basel)*, vol. 7, no. 7, 2014, doi: 10.3390/en7074098.

[34] A. Jain and A. Kapoor, "Exact analytical solutions of the parameters of real solar cells using Lambert W-function," *Solar Energy Materials and Solar Cells*, vol. 81, no. 2, 2004, doi: 10.1016/j.solmat.2003.11.018.

[35] J. Prasanth Ram, D. S. Pillai, D. Mathew, J. Ha, and Y. J. Kim, "A simple, reliable and adaptive approach to estimate photovoltaic parameters using spotted hyena

optimization: A framework intelligent to predict photovoltaic parameters for any meteorological change," *Solar Energy*, vol. 236, 2022, doi: 10.1016/j.solener.2022.03.019.

[36] D. Sera, R. Teodorescu, and P. Rodriguez, "PV panel model based on datasheet values," in *IEEE International Symposium on Industrial Electronics*, 2007. doi: 10.1109/ISIE.2007.4374981.

[37] P. Changmai, S. Deka, S. Kumar, T. S. Babu, B. Aljafari, and B. Nastasi, "A Critical Review on the Estimation Techniques of the Solar PV Cell's Unknown Parameters," 2022. doi: 10.3390/en15197212.

[38] E. A. Silva, F. Bradaschia, M. C. Cavalcanti, and A. J. Nascimento, "Parameter estimation method to improve the accuracy of photovoltaic electrical model," *IEEE J Photovolt*, vol. 6, no. 1, 2016, doi: 10.1109/JPHOTOV.2015.2483369.

[39] U. Akram, M. Nadarajah, R. Shah, and F. Milano, "A review on rapid responsive energy storage technologies for frequency regulation in modern power systems," 2020. doi: 10.1016/j.rser.2019.109626.

[40] M. Farrokhabadi *et al.*, "Microgrid Stability Definitions, Analysis, and Examples IEEE PES Task Force on Microgrid Stability Definitions, Analysis, and Modeling," *IEEE TRANSACTIONS ON POWER SYSTEMS*, vol. 35, no. 1, 2020.

[41] I. S. Association, *IEEE 1547-2018. Standard for Interconnection and Interoperability of Distributed Energy Resources with Associated Electric Power Systems Interfaces*, no. February. 2018.

[42] S. Xue, B. Kasztenny, I. Voloh, and D. Oyenuga, “Power System Frequency Measurement for Frequency Relaying,” *Western Protective Relay Conference, At Spokane, WA*, no. October 2007, 2007.

[43] L. Asnin, V. Backmutsky, M. Gankin, J. Blashka, and M. Sedlachek, “DSP methods for dynamic estimation of frequency and magnitude parameters in power system transients,” in *2001 IEEE Porto Power Tech Proceedings*, 2001. doi: 10.1109/PTC.2001.964871.

[44] T. S. Sidhu, “Accurate measurement of power system frequency using a digital signal processing technique,” *IEEE Trans Instrum Meas*, vol. 48, no. 1, 1999, doi: 10.1109/19.755064.

[45] M. Akke, “Frequency estimation by demodulation of TWo complex signals,” *IEEE Power Engineering Review*, vol. 17, no. 1, 1997, doi: 10.1109/MPER.1997.560678.

[46] P. Denys, C. Counan, L. Hossenlopp, and C. Holweck, “Measurement of Voltage Phase for The French Future Defence Plan Against Losses of Synchronism,” *IEEE Transactions on Power Delivery*, vol. 7, no. 1, 1992, doi: 10.1109/61.108890.

[47] M. S. Priyadarshini, M. Bajaj, L. Prokop, and M. Berhanu, “Perception of power quality disturbances using Fourier, Short-Time Fourier, continuous and discrete wavelet transforms,” *Sci Rep*, vol. 14, no. 1, 2024, doi: 10.1038/s41598-024-53792-9.

[48] W. T. Kuang and A. S. Morris, “Using short-time Fourier transform and wavelet packet filter banks for improved frequency measurement in a Doppler robot tracking

system," *IEEE Trans Instrum Meas*, vol. 51, no. 3, 2002, doi: 10.1109/TIM.2002.1017713.

[49] T. Lin, M. Tsuji, and E. Yamada, "A wavelet approach to real time estimation of power system frequency," in *Proceedings of the SICE Annual Conference*, 2001. doi: 10.1109/sice.2001.977806.

[50] T. Lobos and J. Rezmer, "Real-time determination of power system frequency," *IEEE Trans Instrum Meas*, vol. 46, no. 4, 1997, doi: 10.1109/19.650792.

[51] P. Kdash and S. Kpanda, "Fast estimation of voltage and current phasors in power networks using an adaptive neural network," *IEEE Transactions on Power Systems*, vol. 12, no. 4, 1997, doi: 10.1109/59.627847.

[52] L. L. Lai, C. T. Tse, W. L. Chan, and A. T. P. So, "Real-time frequency and harmonic evaluation using artificial neural networks," 1999. doi: 10.1109/61.736681.

[53] Z. Salcic, Z. Li, U. D. Annakkage, and N. Pahalawaththa, "A comparison of frequency measurement methods for underfrequency load shedding," *Electric Power Systems Research*, vol. 45, no. 3, 1998, doi: 10.1016/s0378-7796(98)00024-8.

[54] J. Wu, J. Long, and J. Wang, "High-accuracy, wide-range frequency estimation methods for power system signals under nonsinusoidal conditions," *IEEE Transactions on Power Delivery*, vol. 20, no. 1, 2005, doi: 10.1109/TPWRD.2004.837826.

[55] W. Zahoor and S. H. Zaidi, “Synchronization and dq current control of grid-connected voltage source inverter,” in *17th IEEE International Multi Topic Conference: Collaborative and Sustainable Development of Technologies, IEEE INMIC 2014 - Proceedings*, 2014. doi: 10.1109/INMIC.2014.7097384.

[56] M. Surprenant, I. Hiskens, and G. Venkataramanan, “Phase locked loop control of inverters in a microgrid,” in *IEEE Energy Conversion Congress and Exposition: Energy Conversion Innovation for a Clean Energy Future, ECCE 2011, Proceedings*, 2011. doi: 10.1109/ECCE.2011.6063833.

[57] S. Golestan, M. Monfared, and F. D. Freijedo, “Design-oriented study of advanced synchronous reference frame phase-locked loops,” *IEEE Trans Power Electron*, vol. 28, no. 2, 2013, doi: 10.1109/TPEL.2012.2204276.

[58] F. SEVİLMİŞ and H. KARACA, “Performance analysis of SRF-PLL and DDSRF-PLL algorithms for grid interactive inverters,” *International Advanced Researches and Engineering Journal*, vol. 3, no. 2, 2019, doi: 10.35860/iarej.412250.

[59] E. Bullich-Massagué, R. Ferrer-San-josé, M. Aragüés-Peñalba, L. Serrano-Salamanca, C. Pacheco-Navas, and O. Gomis-Bellmunt, “Power plant control in large-scale photovoltaic plants: Design, implementation and validation in a 9.4 MW photovoltaic plant,” *IET Renewable Power Generation*, vol. 10, no. 1, 2016, doi: 10.1049/iet-rpg.2015.0113.

[60] M. J. B. B. Davi, M. Oleskovicz, and F. V. Lopes, “Study on IEEE 2800-2022 standard benefits for transmission line protection in the presence of inverter-based

resources," *Electric Power Systems Research*, vol. 220, 2023, doi: 10.1016/j.epsr.2023.109304.

[61] R. Teodorescu, M. Liserre, and P. Rodríguez, *Grid Converters for Photovoltaic and Wind Power Systems*. 2010. doi: 10.1002/9780470667057.

[62] D. Kolantla, S. Mikkili, S. R. Pendem, and A. A. Desai, "Critical review on various inverter topologies for pv system architectures," *IET Renewable Power Generation*, vol. 14, no. 17, 2020, doi: 10.1049/iet-rpg.2020.0317.

[63] F. Liu, Z. Fan, Q. Liu, and R. Zou, "Equivalent Input Disturbance-Based Control Design for Three Phase Dual-Stage Grid-Tied Photovoltaic System Considering Dead Time Effect," *Front Energy Res*, vol. 9, 2021, doi: 10.3389/fenrg.2021.775437.

[64] A. Narang, G. G. Farivar, H. D. Tafti, and J. Pou, "Power Reserve Control Methods for Grid-Connected Photovoltaic Power Plants: A Review," in *2022 IEEE 7th Southern Power Electronics Conference, SPEC 2022*, 2022. doi: 10.1109/SPEC55080.2022.10058393.

[65] M. Morjaria, D. Anichkov, V. Chadliev, and S. Soni, "A grid-friendly plant: The role of utility-scale photovoltaic plants in grid stability and reliability," *IEEE Power and Energy Magazine*, vol. 12, no. 3, 2014, doi: 10.1109/MPE.2014.2302221.

[66] A. Sangwongwanich, Y. Yang, F. Blaabjerg, and D. Sera, "Delta Power Control Strategy for Multistring Grid-Connected PV Inverters," *IEEE Trans Ind Appl*, vol. 53, no. 4, 2017, doi: 10.1109/TIA.2017.2681044.

[67] C. Yongning, L. Yan, L. Zhen, C. Ziyu, and L. Hongzhi, "Study on Grid-connected Renewable Energy Grid Code Compliance," in *iSPEC 2019 - 2019 IEEE Sustainable Power and Energy Conference: Grid Modernization for Energy Revolution, Proceedings*, 2019. doi: 10.1109/iSPEC48194.2019.8974936.

[68] Y. Yang, P. Enjeti, F. Blaabjerg, and H. Wang, "Wide-scale adoption of photovoltaic energy: Grid code modifications are explored in the distribution grid," *IEEE Industry Applications Magazine*, vol. 21, no. 5, 2015, doi: 10.1109/MIAS.2014.2345837.

[69] W. Shockley, "The Theory of p-n Junctions in Semiconductors and p-n Junction Transistors," *Bell System Technical Journal*, vol. 28, no. 3, 1949, doi: 10.1002/j.1538-7305.1949.tb03645.x.

[70] X. Feng, X. Qing, C. Y. Chung, H. Qiao, X. Wang, and X. Zhao, "A simple parameter estimation approach to modeling of photovoltaic modules based on datasheet values," *Journal of Solar Energy Engineering, Transactions of the ASME*, vol. 138, no. 5, 2016, doi: 10.1115/1.4034357.

[71] "High module conversion efficiency Suntech current sorting process Excellent weak light performance Lower operating temperature Extended wind and snow load tests Withstanding harsh environment Features Industry-leading Warranty Certifications and Standards," 2022. [Online]. Available: www.suntech-power.com

[72] C. Solar Inc, "Canadian_Solar-Datasheet-SuperPower_CS6K-MS_v5.551_EN." [Online]. Available: www.canadiansolar.com,

[73] “BSM525-550M10-72HPH ”, Accessed: Oct. 13, 2023. [Online]. Available: www.bluesunpv.com

[74] “JAM78S30-GR”, Accessed: Oct. 13, 2023. [Online]. Available: www.Jasolar.com

[75] “MBB HC Technology PID Resistance P-Type Tiger Pro 54HC Positive power tolerance of 0~+3% Key Features Multi Busbar Technology.” [Online]. Available: www.jinkosolar.com

[76] International Electrotechnical Commission, “IEC TS 60904-1-2,” 2019.

[77] R. Guerrero-Lemus, R. Vega, T. Kim, A. Kimm, and L. E. Shephard, “Bifacial solar photovoltaics - A technology review,” 2016. doi: 10.1016/j.rser.2016.03.041.

[78] Y. Zhang, Q. Gao, Y. Yu, and Z. Liu, “Comparison of Double-Side and Equivalent Single-Side Illumination Methods for Measuring the I-V Characteristics of Bifacial Photovoltaic Devices,” *IEEE J Photovolt*, vol. 8, no. 2, 2018, doi: 10.1109/JPHOTOV.2017.2778226.

[79] J. Lopez-Garcia, D. Pavanello, and T. Sample, “Analysis of temperature coefficients of bifacial crystalline silicon pv modules,” *IEEE J Photovolt*, vol. 8, no. 4, 2018, doi: 10.1109/JPHOTOV.2018.2834625.

[80] “Datasheet of Bifacial ModuleLONGI-545W ,” https://static.longi.com/L_Gi_LE_T_TMD_059_108_LR_5_72_HBD_530_550_M_35_30_and_15_V14_4c79e9b9a7.pdf.

[81] “"Datasheet of Bifacial Module LG 390N2T-A5.,” https://www.lg.com/global/business/download/resources/.

[82] A. Dobrzycki, D. Kurz, and E. Maćkowiak, “Influence of selected working conditions on electricity generation in bifacial photovoltaic modules in polish climatic conditions,” *Energies (Basel)*, vol. 14, no. 16, 2021, doi: 10.3390/en14164964.

[83] C. Hansen, D. Riley, C. Deline, F. Toor, and J. Stein, “A Detailed Performance Model for Bifacial PV Modules,” *Sand2017-11013C a*, 2017.

[84] J. Steinkohl, X. Wang, P. Davari, and F. Blaabjerg, “Analysis of linear phase-locked loops in grid-connected power converters,” in *2019 21st European Conference on Power Electronics and Applications, EPE 2019 ECCE Europe*, 2019. doi: 10.23919/EPE.2019.8915504.

[85] C. J. O’Rourke, M. M. Qasim, M. R. Overlin, and J. L. Kirtley, “A Geometric Interpretation of Reference Frames and Transformations: Dq0, Clarke, and Park,” *IEEE Transactions on Energy Conversion*, vol. 34, no. 4, 2019, doi: 10.1109/TEC.2019.2941175.

[86] F. M. Gardner, “Phaselock techniques,” *IEEE Trans Syst Man Cybern*, vol. SMC-14, no. 1, 2012, doi: 10.1109/tsmc.1984.6313286.

[87] F. Sevilmiş and H. Karaca, “Performance enhancement of DSOGI-PLL with a simple approach in grid-connected applications,” *Energy Reports*, vol. 8, 2022, doi: 10.1016/j.egyr.2021.11.186.

[88] R. Izah, S. Subiyanto, and D. Prastiyanto, “Improvement of DSOGI PLL Synchronization Algorithm with Filter on Three-Phase Grid-connected Photovoltaic

System," *Jurnal Elektronika dan Telekomunikasi*, vol. 18, no. 1, 2018, doi: 10.14203/jet.v18.35-45.

[89] S. Ke and Y. Li, "Analysis and modelling of a phase-locked loop based on a novel cascade structure of SOGI," *IET Power Electronics*, vol. 16, no. 15, 2023, doi: 10.1049/pel2.12581.

[90] entsoe, "Rate of Change of Frequency (RoCoF) withstand capability.ENTSO-E guidance document for national implementation for network codes on grid connection," Belgium, 2018.

[91] IEEE power and energy society, "IEEE Std 2800TM-2022 Standard for Interconnection and Interoperability of Inverter-Based Resources (IBRs) Interconnecting with Associated Transmission Electric Power Systems," IEEE power and energy society, 2022," 2022.

[92] F. Jibji-Bukar and O. Anaya-Lara, "Frequency support from photovoltaic power plants using offline maximum power point tracking and variable droop control," *IET Renewable Power Generation*, vol. 13, no. 13, 2019, doi: 10.1049/iet-rpg.2019.0211.

[93] S. You, "Solar PV Frequency Control in the U.S. EI and ERCOT Interconnections-Case Studies and Recommendations."

[94] K. H. Ahmed, S. J. Finney, and B. W. Williams, "Passive Filter Design for Three-Phase Inverter Interfacing in Distributed Generation," in *2007 Compatibility in Power Electronics*, IEEE, May 2007, pp. 1–9. doi: 10.1109/CPE.2007.4296511.

[95] Y. Kim, H. Cha, B. M. Song, and K. Y. Lee, “Design and control of a grid-connected three-phase 3-level NPC inverter for Building Integrated Photovoltaic systems,” in *2012 IEEE PES Innovative Smart Grid Technologies, ISGT 2012*, 2012. doi: 10.1109/ISGT.2012.6175663.

[96] M. Dursun and M. K. Dosoglu, “LCL Filter Design for Grid Connected Three-Phase Inverter,” in *ISMSIT 2018 - 2nd International Symposium on Multidisciplinary Studies and Innovative Technologies, Proceedings*, 2018. doi: 10.1109/ISMSIT.2018.8567054.

Appendix. A

Table A.1: Parameters of PPC

Parameter	Value
Upper limit on active power reference (Pmax,1)	1
Lower limit on active power reference (Pmin,1)	0
Upper limit on V/Q control (Qmax)	0.477
Lower limit on V/Q control (Qmin)	-0.477
Reactive power compensation gain (Kc)	0.04
Active power PI controller proportional gain	1.0
Active power PI controller integral gain	1
Reactive power PI controller proportional gain	1
Reactive power PI controller integral time constant	0.1

Table A.2: Parameters of Inverter and Boost Converter controller.

Parameter	Value
Converter controller	
V_{dc} PI controller proportional gain	1.0
V_{dc} PI controller integral time constant	1
Reactive power PI controller proportional gain	1
Reactive power PI controller integral time constant	0.1
Boost Converter	
Outer loop proportional gain	0.1
Outer loop integral time constant	0.03

Inner loop proportional gain	1
Inner loop integral time constant	0.05

Standard IEEE 9-Bus System

Table A.3: Terminal conditions of IEEE 9-bus system

Bus	Voltage (kV)	Phase angle (deg)	Active power (pu)	Reactive Power (pu)
1	17.16	0.0	0.7163	0.2791
2	18.45	9.3507	1.63	0.049
3	14.145	5.142	0.85	-0.1145

Table A.4: Transmission line characteristics of IEEE 9-bus system

From bus	To bus	R (pu/m)	X (pu/m)	B (pu/m)
4	5	0.01	0.068	0.0176
4	6	0.017	0.092	0.158
5	7	0.032	0.161	0.306
6	9	0.039	0.1738	0.358
7	8	0.0085	0.0576	0.149
8	9	0.0119	0.1008	0.209

Table A.5: Load characteristics of IEEE 9-bus system

Bus	P (pu)	Q (pu)
5	1.25	0.5
6	0.9	0.3
8	1.0	0.35

Table A.6: Hydro governor parameters

Parameter	Value	Parameter	Value
Dead band value	0.00033 pu	Permanent droop (Rp)	0.2 pu
Maximum gate position (Gmax)	1.0 pu	Minimum gate position (Gmin)	0.0 pu
Maximum gate opening rate (MXGT OR)	1 pu/s	Maximum gate closing rate (MXGT CR)	1 pu/s
Pilot servo motor time constant (TA)	0.05 pu	Gate servo time constant (TC)	0.2 pu
Gate servomotor time constant (TD)	0.2	Derivative gain (KD)	0 pu

Table A.7: Hydro turbine parameters

Parameter	Value	Parameter	Value
Head at rated conditions	1.0 pu	Output power at rated conditions	1.0 pu
Gate position at rated conditions	1.0 pu	Rated no-load gate	0.05 pu
Water starting time (TW)	2.0 s	Penstock head loss coefficient (fp)	0.02 pu
Turbine damping constant (D)	0 pu		